COBALT SILICIDE FORMATION THROUGH A DIFFUSION BARRIER

BY

HAMEDA ALI ABRASS

Submitted in partial fulfilment of the requirements for the degree of

DOCTOR OF PHILOSOPHY (PhD) IN PHYSICS

In the Faculty of Natural and Agricultural Sciences

University of Pretoria

July 2015

Supervisor/ Promoter: Prof. C.C. Theron

SUMMARY

Cobalt silicide formation through a diffusion barrier

by

Hameda Ali Abrass

Submitted in partial fulfillment of the requirements for the degree of doctor of philosophy in Physics (PhD) in the Faculty of Natural and Agricultural Sciences, University of Pretoria.

Supervisor/ Promoter: Prof. C.C. Theron

Silicon (Si) has various applications in different technological fields as a structural material or a semiconductor. Cobalt disilicide is an attractive silicide for contact with Si because it has favourable properties such as low resistivity. Recently, a great deal of interest has been shown in thin film silicides, produced by the reaction of alloys of cobalt with a silicon substrate. In these systems the actual concentration of Co is diluted and the reaction pathway is changed from that of pure Co and Si reaction.

Another way of influencing the reaction pathway is by use of a diffusion barrier. This study investigates solid-state reactions between Co thin films (126 nm) and single-crystalline Si substrate. Specifically, it examines the formation of cobalt silicides through diffusion barrier interlayers composed of iron-zirconium (FeZr).

Samples with the standard thickness of Co thin films and various thicknesses of the same composition diffusion barrier ($Fe_{90}Zr_{10}$) were prepared through utilisation of the molecular beam epitaxial (MBE) deposition technique on Si substrates. These samples were annealed at temperatures of 400 and 450 °C for durations of 3 and 24 hours under high vacuum conditions. The results of the solid-state reactions are analysed by Rutherford backscattering spectrometry (RBS) before and after annealing, X-ray diffraction (XRD) using CoK_{α} radiation, and scanning electron microscope (SEM) and some structures were

characterized by Auger electron spectroscopy (AES) depth profiling. The formation of the various cobalt silicides found at diffusion barrier interlayers is then interpreted in terms of the reduced flux of reactant atoms at the reaction interface, which is due to the different thicknesses of the diffusion barriers.

The RBS results indicate that the unannealed spectra fit well with those annealed at 350 °C, thus showing that no reactions took place. The XRD results reveal that, at temperatures of 400 and 450 °C, Co reacted with the Si substrate and formed a mixed layer of cobalt silicides, namely, CoSi and $CoSi_2$. The SEM images revealed that the unannealed Co thin films had a granular surface with an average granule diameter of 20 nm. After annealing, the average granule diameter was observed to be larger than the unannealed value. However, after some annealing periods the granule diameters were observed to generally become larger and this substantiates cobalt silicide formation compared to the unannealed images. In some images the crystals bore visible black spots due to the presence of carbon in the interface, which is confirmed by the AES results. A cross-sectional SEM image of the Si<100>|FeZr(53 nm)|Co(126 nm) sample, prepared by liquid nitrogen (LN_2) fracture and annealed at 450 °C for 24 h, reveals three different observable layers. These results were in good agreement with the information gained from the AES analysis.

Concentration-controlled phase selection in solid-state reaction has been proposed as a model to interpret first-phase formation occurring at solid interfaces. This is done in the context of the effective heat of formation (EHF) model. The EHF model predicts, as the initial phase, the formation of Co_2Si at the Co/Si interface if there is no barrier layer. In the case of this study, the presence of FeZr as barrier layer caused CoSi to be formed as the initial phase, thus bypassing Co_2Si formation. The EHF model shows that the diffusion barrier can reduce the effective concentration of the Co atoms to a value where the effective heat of formation of CoSi is more negative than that of Co_2Si. Thus, first-phase formation of CoSi is thermodynamically favoured. The results obtained in this study fit well the model if the initial phase Co_2Si has been bypassed.

UNIVERSITEIT VAN PRETORIA
UNIVERSITY OF PRETORIA
YUNIBESITHI YA PRETORIA

DECLARATION

I, Hameda Ali Abrass, declare that this thesis, which I hereby submit for the degree of PhD in Physics at the University of Pretoria, is my own work and has not previously been submitted by me for a degree at this or any other tertiary institution.

Signature: ……

Date: ……

ACKNOWLEDGEMENTS

I would like to express my appreciation to my supervisor, Prof. C. C. Theron, not only for his continued patience and support during the course of this study, but also for being an excellent instructor and mentor. I would also like to express my gratitude to Dr Nick van der Berg and Mr A. J Botha for their guidance in and assistance with the microscopy aspect of this research, as well as Ms Wiebke Grote for her assistance with the XRD analyses. I would further like to thank the University of Pretoria and the Department of Physics for the support during this study. I also wish to acknowledge and thank the students and staff of the Department of Physics, and my friends, both near and far, for their support. In particular, I would like to recognise the unwavering support, patience and love of my husband, whose encouragement through the highs and lows of this study I greatly appreciate.

Finally, I would like to acknowledge and thank my daughters for their patience and love.

TABLE OF CONTENTS

SUMMARY.....ii
DECLARATION.....iv
ACKNOWLEDGEMENTS.....v

CHAPTER 1: INTRODUCTION.....1
1.1 Introduction.....1
1.2 Cobalt silicides.....2
1.3 Objectives and scope of research.....6
1.4 Thesis outline.....7

CHAPTER 2: THEORETICAL BACKGROUND AND LITERATURE REVIEW.....12
2.1 Introduction.....12
2.2 Diffusion.....12
2.2.1 Solid-state diffusion.....15
2.2.2 Diffusion mechanisms in solids.....15
2.2.3 Lattice diffusion.....16
2.2.3.1 Vacancy mechanism.....16
2.2.3.2 Interstitial mechanism.....17
2.2.3.3 Interstitialcy mechanism.....17
2.2.4 The diffusion coefficient.....18
2.3 Heats of reaction.....19
2.4 Effective heat of formation model.....22
2.5 Cobalt silicides formation.....25
2.5.1 Cobalt silicides formation on a Co-Si system.....25
2.5.2 Cobalt silicides formation through diffusion barrier.....26

CHAPTER 3: EXPERIMENTAL TECHNIQUES.....36
3.1 Introduction.....36
3.2 Barrier layer fabrication.....36
3.2.1 CrZr by arc-melting.....36
3.2.1.1 The Compact Arc-Melter (MAM-1).....36
3.2.1.2 The Ebeam evaporation technique.....38
3.2.1.3 E-beam evaporation setup.....39
3.2.2 FeZr by solid-state diffusion.....40
3.2.2.1 Sputter deposition.....40
3.2.3 FeZr by co-evaporation.....45
3.2.3.1 Molecular beam epitaxy (MBE).....45
3.2.3.2 Deposition setup.....47
3.2.3.3 Preparation and analysis of the Co/FeZr/Si system.....48
3.3 Annealing of samples.....49
3.4 Rutherford backscattering spectrometry.....51

3.4.1 Kinematic factor 54
3.4.2 Depth scaling of thin film systems 56
3.4.3 Energy loss 58
3.4.4 Scattering cross-section 60
3.5 Scanning electron microscope (SEM) 61
3.5.1 SEM Experimental Setup 63
3.5.2 Fracture cross-section 64
3.6 X-ray diffraction (XRD) 65
3.6.1 XRD Experimental Setup 68
3.7 Auger electron spectroscopy (AES) 69
3.7.1 Quantitative analysis 71

CHAPTER 4: RESULTS AND ANALYSIS 79
4.1 Introduction 79
4.2 Si/CrZr/Si system by arc melting 79
4.3 Si/FeZr/Co system by solid-state diffusion 79
4.4 Si/FeZr/Co system by MBE 80
4.4.1 Introduction 80
4.4.2 Unannealed sample 82
4.4.2.1 RBS results 82
4.4.2.2 SEM results 83
4.5 Annealed Si<100>/FeZr(33 nm)/Co(126 nm) sample 85
4.5.1 RBS results 85
4.5.2 XRD results 90
4.5.3 SEM results 91
4.6 Annealed Si<100>/FeZr(43nm)/Co(126 nm) Sample 92
4.6.1 RBS results 92
4.6.2 XRD results 94
4.6.3 SEM results 96
4.7 Annealed Si<100>/FeZr(48 nm)/Co(126 nm) sample 97
4.7.1 RBS results 97
4.7.2 XRD results 98
4.7.3 SEM results 98
4.8 Annealed Si<100>/FeZr(53 nm)/Co(126 nm) sample 99
4.8.1 RBS results 99
4.8.2 XRD results 100
4.8.3 SEM results 101
4.9 Annealed Si<100>/FeZr(63 nm/Co(126 nm) sample 102
4.9.1 RBS and AES results 102
4.9.2 XRD results 107
4.9.3 SEM results 108
4.9.4 A cross-sectional SEM 109
4.10 Annealed Si<100>/FeZr(83 nm)/Co(126 nm) Sample 110
4.10.1 RBS results 110
4.10.2 XRD results 111

4.10.3 SEM results 112
4.11 Annealed Si<100>/FeZr(100 nm)/Co(126 nm) sample 113
4.11.1 RBS results 113
4.11.2 XRD results 114
4.11.3 SEM results 114

CHAPTER 5: CONCLUSIONS AND FUTURE WORK 117
5.1 Summary and Conclusions 117
5.2 Future work 122

LIST OF TABLES

Table 1.1: The formation sequence, crystal structure, and formation temperature of cobalt silicides..... 3

Table 2.1: Heats of formation of some Co-Si compounds expressed in different ways.. 21

Table 2.2: Review of studies concerned with cobalt silicides formation on a Co-Si system. 25

Table 2.3: Review of studies on cobalt silicide formation through diffusion barrier layers. 26

Table 3.1: The temperature vapour pressures of Cr and Zr. 40

Table 3.2: The FeZr/Si samples preparation. 45

Table 4.1: Results of the RBS simulations of the annealed sample. 105

Table 5.1: Cobalt silicide formation through FeZr diffusion barrier layers. 120

LIST OF FIGURES

Figure 1.1: The crystal structure of the different cobalt silicides 3

Figure 1.2: Illustration showing the same ΔC with different Δx values. 5

Figure 2.1: Schematic diagram of the formation of metal silicide M_iSi_j formed from the diffusion of silicon or metal atoms. 13

Figure 2.2: Schematic representation of a grain boundary 14

Figure 2.3: Vacancy diffusion mechanism. 16

Figure 2.4: Interstitial diffusion mechanism. 17

Figure 2.5: Interstitialcy diffusion mechanism. 17

Figure 2.6: EHF diagram for the Co-Si binary system 24

Figure 3.1: Images of the Compact Arc-Melter (Edmund Bühler GmbH MAM-1). 37

Figure 3.2: Interior view of the Compact Arc-Melter containing a prepared sample 38

Figure 3.3: A simple diagram of electron beam evaporation 39

Figure 3.4: (a) The sputtering chamber with the lid open showing the heating lamps and rotating sample-plate holder, (b) Interior of the sputtering chamber showing an opened target shutter with the target at the top, and a closed target shutters. 42

Figure 3.5: DC sputtering setup. 43

Figure 3.6: Schematic diagram of preparation and analysis of the Zr/Fe/Si samples. 44

Figure 3.7: Illustration of the chamber of an MBE system. 47

Figure 3.8: Schematic diagram showing the thin film wedge-shaped layers on a wafer. 48

Figure 3.9: Schematic diagram of preparation and analysis of the Co/FeZr/Si samples. 49

Figure 3.10: Tube furnace annealing system consisting of data logging system, vacuum pumps and furnace 50

Figure 3.11: Annealing curves for samples at temperatures of 400 °C and 450 °C for 19 h versus time (hours). 51

Figure 3.12: Schematic overview of the RBS setup at the University of Pretoria 53

Figure 3.13: Schematic diagram showing the RBS experimental setup at the University of Pretoria. 54

Figure 3.14: (a) Scattering geometry and (b) spectrum of an RBS measurement of a thin compound target. 57

Figure 3.15: A schematic diagram showing the backscattering events in a target consisting of one element. The angles θ_1 and θ_2 are positive regardless of the side on which they lie with respect to the normal of the target. 59

Figure 3.16: Schematic diagram of an external view of the SEM's fundamental components. 61

Figure 3.17: Schematic demonstration of the interaction of the incident electron beam with the sample and the radiation signals generated during interaction. 62

Figure 3.18: The scanning electron microscope. 64

Figure 3.19: Illustration of Bragg's law for an incident X-ray beam impinging on a crystalline substrate 66

Figure 3.20: (a) XRD setup (b) XRD setup Goniometer axes in horizontal sample mount XRD (c) In-plane axis (optional). 67

Figure 3.21: The Auger process. The ionization, atomic transition and Auger electron emission processes are shown schematically in (a) an atomic energy level model and in (b) an atomic shell model. 70

Figure 3.22: A typical AES spectrum from two metal alloys. 73

Figure 3.23: A typical AES depth profile of Si/FeZr/Co sample after annealing. 74

Figure 4.1: Raw RBS spectrum of unannealed Si<100>/FeZr(63 nm)/Co(126 nm) sample with RUMP simulation spectrum. 83

Figure 4.2: SEM micrographs of Si<100>/FeZr(63 nm)/Co(126 nm) unannealed sample: (a) low magnification and (b) high magnification. 84

Figure 4.3: Overlay of RBS spectra of unannealed Si<100>|FeZr(33 nm)|Co(126 nm) and 400 °C annealed samples. 86

Figure 4.4: Overlay of RBS spectra of unannealed Si<100>|FeZr(33 nm)|Co(126 nm) and 450 °C annealed samples. 87

Figure 4.5: The AES depth profile of the Si<100>|FeZr(33 nm)|Co(126 nm) sample after annealing at 450 °C for 24 h. 88

Figure 4.6: (a) Comparison between the RBS spectrum and a simulation of the annealed Si<100>|FeZr(33 nm)|Co(126 nm) sample, and (b) a representative composition profile of the simulation used. 89

Figure 4.7: XRD pattern of the Si<100>|FeZr(33 nm)|Co(126 nm) sample annealed at 400 °C for 24 h showing the formation of CoSi.. 90

Figure 4.8: XRD pattern of the Si<100>|FeZr(33 nm)|Co(126 nm) sample annealed at 450 °C for 24 h showing the formation of CoSi.. 91

Figure 4.9: SEM micrographs of the Si<100>|FeZr(33 nm)|Co(126 nm) sample (a) at 400 ºC and (b) at 450 °C. 92

Figure 4.10: Overlay of RBS spectra of the Si<100>|FeZr(43 nm)|Co(126 nm) unannealed and 400 °C annealed samples. 93

Figure 4.11: Overlay of RBS spectra of the Si<100>|FeZr(43 nm)|Co(126 nm) unannealed and 450 °C annealed samples 94

Figure 4.12: XRD pattern of a sample of Si<100>|FeZr(43 nm)|Co(126 nm) annealed at 400 °C for 24 h showing the formation of CoSi. 95

Figure 4.13: XRD pattern of a sample of Si<100>|FeZr(43 nm)|Co(126 nm) annealed at 450 °C for 24 h showing the formation of CoSi. 95

Figure 4.14: SEM micrographs of the Si<100>|FeZr(43 nm)|Co(126 nm) samples (a) at 400 °C (b) at 450 °C. 96

Figure 4.15: Overlay of RBS spectra of Si<100>|FeZr(48 nm)|Co(126 nm) unannealed and 400 °C annealed samples. 97

Figure 4.16: XRD pattern of a sample of Si<100>|FeZr(48 nm)|Co(126 nm) annealed at 400 °C for 24 h, showing the formation of a mixture of CoSi and $CoSi_2$ 98

Figure 4.17: SEM micrographs of the Si<100>|FeZr(48 nm)|Co(126 nm) sample at 400 °C. 99

Figure 4.18: Overlay of RBS spectra of Si<100>|FeZr(53 nm)|Co(126 nm) unannealed and 450 °C annealed samples. 100

Figure 4.19: XRD pattern of the Si<100>|FeZr(53 nm)|Co(126 nm) sample annealed at 450 °C for 24 h. 101

Figure 4.20: SEM micrographs of the Si<100>|FeZr(53 nm)|Co(126 nm) sample annealed at 450 °C. 102

Figure 4.21: Overlay of RBS spectra of the Si<100>|FeZr(63 nm)|Co(126 nm) unannealed and 450 °C annealed samples. 103

Figure 4.22: The AES depth profile of the Si<100>|FeZr(63 nm)|Co(126 nm) sample after annealing at 450 °C for 24 h. 104

Figure 4.23: (a) Comparison between the RBS spectrum and a simulation of the annealed sample, and (b) a representative composition profile of the simulation used. 106

Figure 4.24: XRD pattern of the annealed Si<100>|FeZr(63 nm)|Co(126 nm) sample at 450 °C for 24 h, showing the formation of a mixture of CoSi and $CoSi_2$ 108

Figure 4.25: SEM micrograph of the annealed Si<100>|FeZr(63 nm)|Co(126 nm) sample at 450 °C. 109

Figure 4.26: Cross-sectional SEM image of the annealed Si<100>|FeZr(63 nm)|Co(126 nm) sample prepared by fracturing. 110

Figure 4.27: Overlay of RBS spectra of the Si<100>|FeZr(83 nm)|Co(126 nm) unannealed sample and 450 °C for 24 h annealed sample. 111

Figure 4.28: XRD pattern of a sample of Si<100>|FeZr(83 nm)|Co(126 nm) annealed at 450 ºC for 24 h showing the formation of a mixture of CoSi and $CoSi_2$ 112

Figure 4.29: SEM micrographs of Si<100>|FeZr(83 nm)|Co(126 nm) at 450 ºC. 112

Figure 4.30: Overlay of RBS spectra of the Si<100>|FeZr(100 nm)|Co(126 nm) unannealed and 450 °C for 24 h annealed samples. 113

Figure 4.31: XRD pattern of a sample of Si<100>|FeZr(100 nm)|Co(126 nm) annealed at 450 ºC for 24 h showing the formation of a mixture of CoSi and $CoSi_2$..... 114

Figure 4.32: SEM micrographs of Si<100>|FeZr(100 nm)|Co(126 nm) at 450 ºC. 115

Figure 5.1: A diagram showing cobalt silicide formation through different thicknesses of FeZr diffusion barrier layers. 119

Figure 5.2: Overlay of XRD diffraction patterns of samples annealed at 450 °C for 24 h and different thicknesses of barrier layer (33, 43, 53, 63, 83 and 100 nm). 121

LIST OF ABBREVIATIONS

AC	Alternating Current
AES	Auger Electron Spectroscopy
AFM	Atomic Force Microscope
AMRF	Average Matrix Relative sensitivity Factor
BE	Backscattered Electrons
CCPS	Concentration-Controlled Phase Selection
CM	Ceramic/Metal
CVD	Chemical Vapour Deposition
DC	Direct Current
EHF	Effective Heat of Formation model
FEG	Field Emission Guns
HF	High Frequency
HV	High Vacuum
ICDD-PDF-2	International Centre for Diffraction Data files
LN_2	Liquid of Nitrogen
M	Metal
MBE	Molecular Beam Epitaxy
PVD	Physical Vapour Deposition
RBS	Rutherford Backscattering Spectrometry
RF	Radio Frequency
RHS	Rectangular Hollow Section

RHEED	Reflection High-Energy Electron Diffraction
RUMP	Rutherford Universal Manipulation Program
SE	Secondary Electron
SEM	Scanning Electron Microscope
SSD	Solid-State Detector
TEM	Transmission electron microscopy
UHV	Ultra-High Vacuum
VLSI	Very large-scale integration
XRD	X-Ray Diffraction

CHAPTER 1

INTRODUCTION

1.1 Introduction

A silicide is a compound of silicon and another metal from the periodic table. Over the past few decades, silicides have been investigated extensively [1-7] due to their potential use in microelectronic devices. They have been used as contacts, barrier contacts, gate electrodes, local interconnects and diffusion barriers [8].

Metal silicide thin films are formed by a reaction between a silicon substrate and a deposited metal layer, usually as a result of thermal treatment. The interactions between metal film layers and silicon typically take place at temperatures well below the melting point of the product and the reactants. The phase diagrams for binary metal-silicide-forming systems usually show several equilibrium phases [9]. Some of these phases are present as detectable growth phases under steady-state annealing conditions. However, alternative methods such as sputtering [10, 11] or co-evaporation [12] are also employed to form these compounds. Reaction between the metal and the silicon substrate can also be achieved by depositing the metal onto a heated substrate in reactive deposition [13, 14] or reactive deposition epitaxy [15]. Moreover, silicides may also be produced by ion beam mixing [16] or by laser irradiation [17]. Amongst the metal silicides, epitaxial silicides have received considerable attention due to their thermal stability, lower electrical resistivity, and, more importantly, the potential to epitaxially overgrow the silicide layer with more silicon [18]. These features could potentially open the way to the creation of new classes of devices based on semiconductor-metal-semiconductor multilayer structures.

In thin film systems, only one compound phase usually forms between two components, silicon and metal. It is believed that phase formation in thin films is dictated by kinetics rather than by thermodynamics. After the metal layer has been totally consumed whilst forming the first phase, a second phase, when present in the phase diagram, will form at

higher temperature and longer annealing times [9]. For a new phase to form, it is necessary for the atoms of the metal and silicon to get together near the interface and form a nucleus of the appropriate composition and structure.

One of the epitaxial silicides that have been the subject of many studies is $CoSi_2$, which has replaced titanium in silicon technology to form highly conductive narrow lines on the gate stack of modern metal-oxide-semiconductor devices [19, 20].

1.2 Cobalt silicides

In the cobalt silicide system, in which ultra-thin layers of cobalt are deposited onto a silicon substrate, Si is observed at a temperature of 350 °C to diffuse through the Co- layer via the grain boundary of the Co layer, and accumulate at the sample surface [21]. The metal-rich silicide, Co_2Si, is reported [22-25] as the first phase to grow. However, Lau et al. [26] have reported that Co_2Si and CoSi initially grow side-by-side, and that Co_2Si transforms to CoSi once all the Co is consumed. Based on thermodynamic grounds, the CoSi phase should be the first to form as it constitutes the silicide with the most negative Gibbs energy of formation in the cobalt silicide system. On the other hand it is found that the activation energy of growth for the CoSi phase (1.9 eV) is considerably higher than that of the Co_2Si phase (1.5 eV) [20]. It is therefore possible, for kinetic reasons, that Co_2Si grows first and is followed by simultaneous growth of Co_2Si and CoSi. $CoSi_2$ phase on crystalline Si is characterized by a threshold temperature of approximately 550 °C [27]. Above this temperature, the growth of the silicide is controlled by diffusion of Co, mainly via grain boundaries with a smaller contribution of Si diffusion. The kinetics of the growth of the $CoSi_2$ phase is thus characterized by mixture of nucleation-and diffusion-controlled processes. The phase formation is summarised as follows:

$$Co_2Si \rightarrow CoSi \rightarrow CoSi_2$$

Similar to other metal silicides, these cobalt silicides have unique crystal structures. Table 1.1 summarises the phase sequences, crystal structures, and temperatures at which these

silicide phases begin to form, as reported in the literature reviewed. Figure 1.1 presents the crystal structure of the cobalt silicide phases.

Table 1.1: The formation sequence, crystal structure, and formation temperature of cobalt silicides [21, 27].

Phase sequence	**Silicide**	**Crystal structure**	**Lattice parameter**			**Density (at/cm^3)**	**Formation temperature**
			a(Å)	**b(Å)**	**c(Å)**		
First phase	Co_2Si	Orthorhombic	4.918	3.737	7.109	3.06×10^{22}	350 °C
Second phase	CoSi	Cubic	4.447	4.447	4.447	4.60×10^{22}	375 °C
Last phase	$CoSi_2$	Cubic	5.364	5.364	5.364	2.59×10^{22}	550 °C

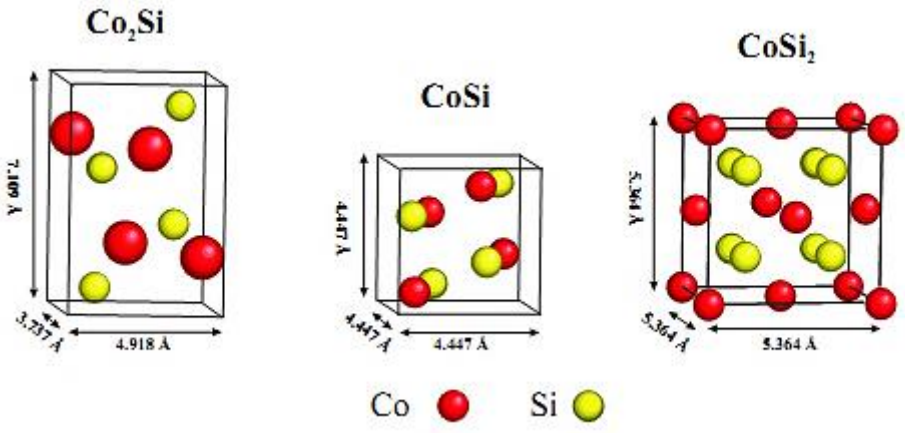

Figure 1.1: The crystal structure of the different cobalt silicides [28].

$CoSi_2$ currently in use has the advantage over other silicides in that this low resistivity silicide phase is not inhibited by geometry, and silicide formation occurs through the diffusion of cobalt rather than silicon. This prevents lateral growth and removes the possibility of short circuits. $CoSi_2$ also enjoys greater thermal stability and uniformity over other silicides, crucial for the implantation and annealing steps in device fabrication [28].
Cobalt disilicide ($CoSi_2$) is an attractive silicide for contact with Si due to favourable properties such as low resistivity (15 μΩ-cm compared to 147 and 110 μΩ-cm for CoSi and

Co_2Si, respectively) [29], high thermal stability, and low lattice mismatch with Si (approximately 1.2%) [30-31]. This approach is very important as it enables the device technologist to select the desired device characteristics like low resistivity, uniformity and good thermal stability. For example, the different phases of cobalt silicide have different resistivities. Some cobalt silicides have a relatively high resistivity whereas others have a low resistivity. This low resistivity makes it a desirable silicide phase for use in certain applications and thus also a desirable phase to attempt to form by using concentration-controlled phase selection.

Most of the epitaxial work [31-33] undertaken thus far has focused on Co/Si<111>, as it is easier to grow Co films with a high epitaxial quality on Si<111> substrates compared to Si<l00>, which has proven difficult [34]. However, it has become clear that the growth of epitaxial Co on Si<100> substrates, as opposed to Si<111>, could have a greater technological impact. As such, a great deal of work has been devoted to growing high-quality films on Si<100> substrates [14, 35-39]. Prior knowledge of which phase can be expected to form first, and at what temperature the reaction would occur, as well as the ability to predict the reaction sequence, obviously holds great advantages for the device technologist.

The effective heat of formation (EHF) model [40, 41] showed, for the first time, that thermodynamic data can be used to explain and predict phase formation in the solid state. This model defines an effective heat of formation that depends upon the concentrations of the reacting species at the interface between two materials in contact. It also illustrates how new phases can be formed by controlling the effective concentration at the growth interface. This approach to the formation of materials is known as concentration-controlled phase selection (CCPS) [42].

The EHF model [42] predicts the sequence of phase formation in binary systems by calculating the heat of formation when a given phase is formed under a restriction of an effective concentration [40-42]. The latter represents the concentration at which the two atoms are available for reaction and is difficult to determine by direct measurement. In the

EHF model it is assumed that the value of this concentration is equal to the liquidus minimum [42-44]. This makes the predictions more accurate [40, 45-47] than those obtained through the Walser-Bené [48, 49] approach. It has, moreover, been used extensively to explain phase formation sequences in a range of different systems. However, because the effective concentration cannot be directly determined, it is not obvious that the model predictions can be falsified, since there will always be a range of effective concentrations that will favour formation of a particular phase. Variations in experimental conditions have indeed been used to explain contrasting observations [50], the argument being that the effective concentration was different in the cases considered.

In the case of phase formation through a diffusion barrier, the flux of atoms arriving at the reaction interface is determined by the barrier's composition and, more especially, its thickness. Therefore, different thicknesses of the same layer will restrict the flux of atoms (J) to the reaction interface in a predictable manner, according to Fick's first law of diffusion [51].

$$J \approx -D\frac{\Delta C}{\Delta x} \tag{1.1}$$

Where D is the diffusion coefficient of atoms in the barrier layer and $\frac{\Delta C}{\Delta x}$ is the concentration gradient within the barrier layer, assuming $\Delta C_1 = \Delta C_2$, then ΔC is the same for different thicknesses, as shown in Figure 1.2.

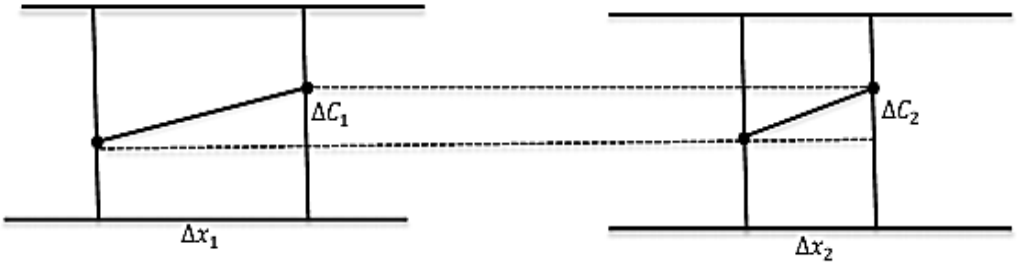

Figure 1.2: Illustration showing the same ΔC with different Δx values.

Controlling silicide phases formed in metal-Si systems through the application of a diffusion barrier is of vital importance, since contact characteristics, such as resistivity and thermal stability, can be pre-selected depending on the phases formed. The diffusion barrier would control phase formation by restricting the concentration of reactants at the reaction interface [52, 53].

The Co-Si binary phase diagram consists of Co_2Si, CoSi and $CoSi_2$ phases. This phase diagram has the liquidus minimum of 1195 °C at 23 at. % Si and three other eutectic points at 40, 62 and 77 at. % Si. According to the EHF diagram for the Co-Si binary system, the predicted first phase to form would be the metal-rich phase Co_2Si, since the liquidus minimum is on the Co-rich side of the phase diagram. The effective concentration can be shifted towards Si-rich by restricting the amount of Co that reach the reaction zone. At 40 at. % Si, it is predicted that CoSi would be the phase formed first, while at 60 at. % Si, $CoSi_2$ would be the first phase to appear. By increasing the thickness of a diffusion barrier, control of phase formation and, therefore, the electrical and physical properties of the Co-Si interface can be done.

In this study the solid-state reaction of thin Co film and single-crystalline Si p-type substrates, mediated by various thicknesses of an Fe_xZr_{1-x} diffusion barrier at 400 and 450 °C, is investigated. The formation of the silicon-rich silicides will be checked to see whether the results are consistent with predictions based on the EHF model. This thesis is particularly concerned with the effects of FeZr diffusion barrier interlayers on first-phase formation and phase-formation sequence in thin-film systems. The diffusion barriers were used to control the silicide phase that forms by controlling the effective concentration at the growth interface. For the purposes of this study, thin film Co/FeZr/Si systems were utilised.

1.3 Objectives and scope of research

The first aim of this thesis is to test whether the EHF model is correct in its predictions by forcing Co to first diffuse through an FeZr barrier layer before reaching a silicon substrate. By using different thicknesses of the FeZr barrier layer, the flux of the Co atoms arriving at

the silicide-forming interface will also be controlled. The second aim of this study is to investigate and gain more insight in the solid-state interaction between thin Co films deposited on an FeZr diffusion barrier layer which has been co-deposited on an Si substrate at low temperatures. This will involve investigating the temperature at which a Co thin film starts to react with Si in the thin film case and identifying the initial phases formed. The study also aims to investigate the concentration-controlled phase selection in solid-state reaction using a diffusion barrier layer to interpret first-phase formation occurring at solid interfaces.

1.4 Thesis outline

The thesis consists of five chapters and can be outlined as follows. Chapter 1 provides general information of silicides and cobalt silicides, as well as the scope of the investigation that informs this study. The second chapter discusses diffusion in solids, Co/Si reactions, and interface characteristics. It furthermore presents an overview of previous works concerned with Co/Si reactions. Chapter 3 discusses the approach used for sample preparation and the experimental techniques employed in sample analysis for this study. In the fourth chapter, the experimental results are presented and discussed. Lastly, conclusions are drawn from the above investigation and recommendations for future work are given in chapter five.

References

[1] C. M. Comrie and J. M. Egan, "Diffusion of silicon in Pd_2 Si during silicide formation.", *Journal of Applied Physics, (64), (1988).*

[2] C. M. Comrie, L.M. Egan, J.C. Liu and J. W. Mayer, "An investigation into the mechanism of epitaxial Pd_2Si formation," *South Africa Journal of Science, (84), (1988).*

[3] A. Falepin, C. M. Comrie, A. Vantomme and G. Langouche, "Study of phase formation in ε- FeSi layers by pulsed laser annealing", *Hyperfine Interactions 134(6), (2001) 153-160.*

[4] H. Leon, H. Won, Y. Kim, J. Lee and R. I. Nemanich, "Analysis of Ti silicide formation with Ta interlayer on Si(100)", *Journal of the Korean Physical Society 40, (2002) 903-907.*

[5] C. C. Theron, "The influence of oxygen on the solid-state reaction between nickel and silicon. Master thesis", *University of Stellenbosch, South Africa, (1994).*

[6] M. A. E. Wandt, C. M. Comrie, J. E. Mecleod and R. Pertorius, "Pt_2Si formation: diffusion marker and radioactive silicon tracer studies", *Journal of Applied Physics 67, (1990).*

[7] E. C. Zingu, C. M. Comrie and R. Pretorius, "The effect of interposed silicide thickness on grown rate in bilayer silicide thin-film structure: The Si (111)/Pd_2Si/ crystal", *Journal of Applied Physics 54(2), (1983).*

[8] L. J. Chen, "Metal silicides: An integral part of microelectronics", *JOM 57, (2005) 24-31.*

[9] J. W. Mayer and S. S. Lau, "Electronic Materials Science: For integrated Circuits in Si and GaAs", *Macmillan, New York, (1990) 251-308.*

[10] O. Chamirian, A. Lauwers, C. Demeurisse, H. Guerault and A. Vantomme, "$CoSi_2$ formation Co_x Ni_{1-x} / Ti system", *Microelectronic Engineering 64, (2002) 173-180.*

[11] R. Y. Naidoo, C. M. Comrie, T. Doyle and R. Pertorius, "High quality thin film super-conductors formed in in situ by sputter deposition", *South African Journal of Physics, 16, (1993).*

[12] F. M. d'HeurIe and C. Petersson, "Formation of thin films of $CoSi_2$: nucleation and diffusion mechanisms", *Thin Solid Films, 128, (1985) 283-297.*

[13] C. M. Comrie, H. Ahmed, C. C. Theron, D. Smeets, J. Demeulemeester, A. Vantomme and C. Detavemier, "Real-time RBS /XRD study of CoS_2 formation from CoSi grown by reactive deposition", *Nuclear Instruments and Methods in Physics Research B, (2007).*

[14] A. H. Reader, J. P. W. B. Duchateau, and J. E. Crombeen, "Epitaxial $CoSi_2$ formation on (001) Si by reactive deposition", *Semiconductor Science and Technology, 8(8), (1993) 1204-1207.*

[15] C. W. Lim, I. Petrov and J. E. Greene, "Epitaxial growth of CoS_2 on Si (001) by reactive deposition epitaxy: island growth and coalescence", *Thin Silod Films 515, (2006) 1340-1348.*

[16] H. C. Mogul, A. J. Steck and S. W. Novak, "Shallow Si p^+ -n junctions fabricated by focused ion beam Ga^+ implantation through thin Ti and $TiSi_2$ layers", *Journal of Applied Physics, 74, (1993).*

[17] C. M. Comrie, A. Falepin, O. Richard, H. Bender and A. Vantomme, "Metastable iron silicide phase formation by pulsed laser annealing", *Journal of Applied Physics 95, (2004).*

[18] M. A. Nicolet and S. S. Lau, "Formation and characterization of transition metal silicides", *VLSI Electronics: Microstructure Science 6, (1993) 329-464.*

[19] A. Alberti, C. Bongiorno, F. La Via and C. Spinella, "High-resolution investigation of atomic interdiffusion during Co/Ni/Si phase transition", *Journal of Applied Physics 94, (2003) 231-237.*

[20] A. Lauwers, M. D. Potter, O. Chamirian, R. Lindsay, C. Demeurisse, C. Vrancken, & K. Maex, "Silicides for the 100-nm node and beyond: Co-silicide, Co(Ni)-silicide and Ni-silicide", *Microelectronic Engineering 64(4), (2002) 131-142.*

[21] S. S. Lau, J. W. Mayer and K. N. Tu, "Interaction in Co/Si thin-film system kinetics", *Journal of Applied Physics, 49, (1978).*

[22] E. C. Cahoon, C. M Comrie and R. Pretorius, "Stability of $NiSi_2$ and $CoSi_2$ in contact with their free metal", *Applied Physics Letters, 44,(1984).*

[23] E. G. Colgan, C. C. Jr and D. E. Kotecki, "Activation energy for CoSi and CoS_2 formation measured during rapid thermal annealing", *Journal of Applied Physics 77, (1995) 614-619.*

[24] G. L. Gurp and C. Langereis, "Cobalt silicide layers on Si structure and growth", *Journal of Applied Physics, 45(5), (1975).*

[25] C. C. Theron, "In situ, real-time characterization of solid state reaction in thin films", *Ph.D. Thesis, University of Stellenbosch, South Africa, (1997).*

[26] S. S. Lau, J. W. Mayer and K.N. Tu, "Interaction in Co/Si thin-film system kinetic", *Journal of Applied Physics, 49, (1978).*

[27] G. Ottaviani, K. N. Tu, P. Psaras and C. Nobili, "In situ resistivity measurement of cobalt silicide formation", *Journal of Applied Physics 62(1), (1987) 2290-2294.*

[28] D. Smeets, "Nucleation diffusion and texture during growth of CoNi-silicides.", *Ph.D. Thesis, KU Leuven, Belgium, (2007).*

[29] K. Maex and M. Van Rossum, "Properties of Metal Silicides", *puplished by INSPE, the Institution of Electrical Engineers, London, (1995).*

[30] F. M. Liu, J. H. Ye, B. Ren, Z. L. Yang, Y. Y. Liao, A. See, L. Chan, and Z. Q. Tian, "Raman spectroscopic studies of the formation processes of cobalt silicide thin films", *Thin Solid Films, 471(1), (2005) 257-263.*

[31] R. T. Tung, "Epitaxial $CoSi_2$ and $NiSi_2$ thin films", *Material Chemistry and Physics, 32, (1992) 107-133.*

[32] C. W. T. Bulle-Lieuwma, "Epitaxial growth of CoS_2/Si structures, *Appllied Surface Science 68, (1993) 1-18.*

[33] C. M. Comrie and V. Hoffman, "Epitaxial cobalt disilicide formation by pulsed laser annealing", *South Africa Journal of Physics, 16, (1993) 171-174.*

[34] S. M. Yalisove, R. T. Tung and D. Loretto, "Epitaxial orientation and morphology of thin $CoSi_2$ films grown on SiC(100): Effects of growth parameters", *Journal of Vacuum Science and Technology A, 7, (1989) 1472-1474.*

[35] J. R. Jimenez, L. M. Hsiung, K.Rajan, L. J.Schowalter, S.Hashimoto and R. D. Thompson, "Control of misoriented grains and pinholes in $CoSi_2$ grown on si(100)", *Applied Physics Letters 57(10), (1990) 2811-5030.*

[36] P. Kluth, C. Detavernier, Q. T. Zhao, J. Xu, H. P. Bochem, S. Lenk and S. Mend, "Growth of patterned thin epitaxial $CoSi_2$ films by titanium oxide mediated epitaxy process", *Thin Solid Films 380, (2000) 201-203*.

[37] A. Vantomme, S. Degroote, J. Dekoster, H. Bender and G. Langouche, "Effects of growth parameters on epitaxy of $CoSi_2$(100) formation by reactive deposition epitaxy", *Mater. Res.Soc.Symp.Proc.402(3), (1996).*

[38] A. Vantomme, S. Degroote, J. Dekoster and G. Langouche, "Epitaxy of $CoSi_2$/Si(l00): from Co/Ti/Si(l00)", *Applied Swface Science, 91(3), (1995)24-29.*

[39] A. Vantomme, M. A. Nicolet and N. D. Theodore, "Epitaxial $CoSi_2$ films on Si(100) by solid-phase reaction", *Journal of Applied Physics 75, (1994) 3882-3891*.

[40] R. Pretorius, "Prediction of silicide first phase and phase sequence from heats of formation.", *Mater. Res. Soc. Symp. Proc, 25, (1984) 15.*

[41] R. Pretorius and J. W. Mayer, "Silicide formation by concentration controlled phase selection, *Journal of Applied Physics, 81(5), (1997) 2448-2450.*

[42] R. Pretorius, T. K. Marais and C. C. Theron, "Thin film compound phase formation sequence: An effective heat of formation model, *Materials Science Reports, 10(1), (1993)1-83.*

[43] J. M. Poate, K. N. Tu and J. W. Mayer, "Thin films–Interdiffusion and reactions", *John Wiley and Sons, New York, 1978).*

[44] R. Pretorius, "Phase sequence of silicide formation at metal-silicon interfaces", *Vacuum, 41.4, (1990) 1038-1042.*

[45] C. C. Theron, O. M. Ndwandwe, J. C. Lombaard, and R. Pretorius. "First phase formation at interfaces: Comparison between Walser-Bené and effective heat of formation model", *Materials Chemistry and Physics ,46(2), (1996) 238-247.*

[46] R. Pretorius, A. M. Vredenberg, F. W. Saris, R. de Reus, "Prediction of phase formation sequence and phase stability in binary metal-aluminum thin-film systems using the effective heat of formation rule", *Journal of Applied Physics, 70, (1991) 3636–3646.*

[47] R. Pretorius, T. K. Marais, C. C. Theron, "Thin film compound phase formation sequence: an effective heat of formation model, *Mater. Sci. Rep. 10, (1993) 1–83.*

[48] R. M. Walser and R. W. Bené, "First phase nucleation in silicon-transitionmetal planar interfaces", *Appl. Phys. Lett, 28, (1976) 624–625.*

[49] R. W. Bené, "1st nucleation rule for solid-state nucleation in metal-metal thin-film systems", *Appl. Phys. Lett, 41, (1982) 529–531.*

[50] R. Pretorius, C. C. Theron, T. K. Marais and H. A. Ras, "Evaluation of anomalies during nickel and titanium suicide formation using the effective heat of formation model.", *Materials Chemistry and Physics, 36(1), (1993) 31-38.*

[51] P. G. Shewmon, "Diffusion in solids", *Warrendale, PA: Minerals, Metals & Materials Society, (1989).*

[52] L. R. Doolittle, "Algorithms for the rapid simulation of Rutherford backscattering spectra", *Nuclear Instruments and Methods in Physics Research Section B: Beam Interactions with Materials and Atoms, 9(3), (1985) 344-351.*

[53] R. De Reus, H. C. Tissink and F. W. Saris, "Low temperature epitaxial $NiSi_2$ formation on Si(111) by diffusing Ni through amorphous Ni–Zr", *Journal of Materials Research, 5.02, (1990) 341-346.*

CHAPTER 2

THEORETICAL BACKGROUND AND LITERATURE REVIEW

2.1 Introduction

The formation and characterisation of thin metallic silicide layers on Si substrates has been the subject of a vast number of fundamental studies as metal silicides are widely used as gates, contacts and interconnects in silicon-based microelectronic devices. The studies of the formation of the silicides of cobalt, nickel and titanium have been most prolific due to the suitability of some of their silicides for applications in very large-scale integration (VLSI) technology.

Cobalt silicides have proven to be very useful for application in microelectronic devices as, for instance, contact materials, interconnects, and gate electrodes in addition to having a wide application in the semiconductor industry [1-9].

2.2 Diffusion

While diffusion can occur in solids, fluids, and gases, convective flow is only found to occur in fluids. Diffusion is a mass transport process from one region to another as a result of random molecular motions. These require a driving force which can take the form of differences in the concentration of a substance (atoms/molecules), thermal energy and mechanical energy [10]. Diffusion is also considered a kinetic process that leads to the uniform distribution of chemical components in a material by decreasing the concentration gradients. By increasing the time duration, the degree to which elements mix through the diffusion process increases and the length chemical homogeneity persists within a phase gradually extends to macroscopic distances [11]. Eventually the net flow of matter will cease when the system is at a state of equilibrium [12]. Therefore,

the simplest definition of diffusion is as follows: a process of material transport by atomic motion from higher to lower regions of concentration. In gases, diffusion occurs by the free flights of atoms (or molecules) between collisions; the individual path lengths are distributed around some well-defined mean free path. Atomic motion in liquids is more subtle and can be thought of as a "shuffling" process where each motion is less than the average spacing of atoms in a liquid. Diffusion in the solid state is the result of random atomic "hops" in a lattice. The diffusivity of each "hop" can be expressed by considering a number of physical quantities that describe the elementary jump processes. These factors include: jump rates, jump distances, and geometric and correlation factors [13]. The intrinsic point defects, mentioned previously, are often the vehicles that allow atoms to perform the tiny jumps, which constitute diffusion. For each defect type there is a specific migration mechanism and, in many cases, combinations of these point defects lead to more complex diffusion mechanisms. What follows is a brief description of the simplest mechanisms by which atoms can be transported through a crystal lattice.

To form a compound at the interface between two adjoining elemental solids, there must be the relative motion of atoms past each other. The mechanism by which movement occurs is referred to as diffusion. An understanding of diffusion mechanisms is important in order to comprehend changes that occur in solid state reaction during the annealing process. During silicide growth, atoms may diffuse from the silicon substrate or from the metal, as indicated by arrows in Figure 2.1.

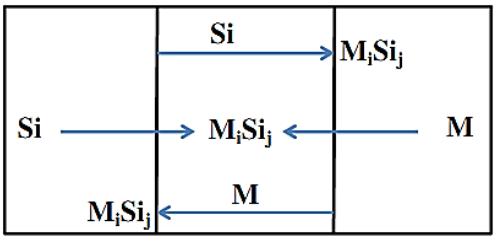

Figure 2.1: Schematic diagram of the formation of metal silicide M_iSi_j formed from the diffusion of either silicon or metal or both atoms.

Metal silicides (M_iS_j) are formed at the interface in both cases. However, it is difficult to tell the direction in which atoms diffuse during solid-state reaction unless a marker technique [14, 15] is employed.

Generally, there are different ways in which atoms can diffuse in a lattice composed of an ordered matrix. The diffusion may move substitutionally by occupying lattice sites, or interstitially by transferring through a sub-lattice of vacant interstitial sites between the main matrix atoms [16]. However, different mechanisms, such as vacancy and interchange mechanisms, have also been postulated with respect to substitutional atom movement [17, 18].

Another possible diffusion mechanism is grain-boundary diffusion. Figure 2.2 shows a schematic representation of a grain boundary. The term grain-boundary diffusion refers to atomic movements occurring in the interfacial region separating two grains. This region provides high mobility routes for atomic migration relative to lattice diffusion. Therefore, diffusion through a highly defected area, such as grain boundaries, often requires a lower activation energy compared to that of lattice diffusion [19]. This diffusion mechanism is commonly observed in thin films due to the high density of grains that occur within them.

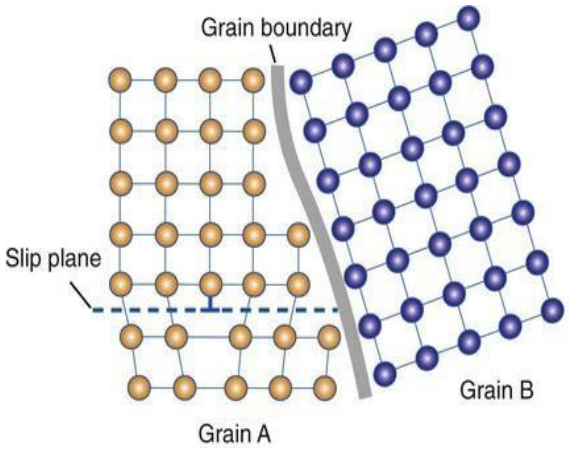

Figure 2.2: Schematic representation of a grain boundary [20].

2.2.1 Solid-state diffusion

Diffusion can be considered as the net number of atoms to pass through a plane of unit area per unit time. This process is driven by a non-uniform gradient, generally referred to as a driving force. A concentration or chemical gradient is one of the most common driving forces, whereby atoms move from a region of high concentration to a region of low concentration. The formal mathematical description of diffusion was derived by Fick [21] and is given in equation (2.1) for a single spatial dimension,

$$J = -D\frac{\partial C}{\partial x} \tag{2.1}$$

where J is the flux of atoms, D is the diffusion coefficient and $\frac{\partial C}{dx}$ represents a concentration gradient.

From a microscopic point of view, diffusion occurs by the Brownian motion [22] of atoms or molecules. By studying the motion of pollen granules in water, the Scottish botanist Robert Brown [22] observed that the particles moved chaotically. Albert Einstein [23] argued that the motion of mesoscopic particles is due to the presence of molecules in the liquid. He further maintained that these molecules, owing to the Boltzmann distribution of their energies, are subject to thermal movements of a statistical nature. These statistical fluctuations are the source of stochastic motions occurring in matter all the way down to the atomic scale [13].

2.2.2 Diffusion mechanisms in solids

Several atomic mechanisms exist that can lead to the movement of atoms in solid-state diffusion. These can generally be classified into diffusion via lattice, also known as volume diffusion, and diffusion via short circuits (which usually occurs along surface or grain boundaries). Due to this movement and transport of atoms in solids, diffusion,

chemical reactions and microstructural changes occur at the interface of two materials. Atom diffusion in solids occurs due to the presence of defects, which include point defects and grain boundaries. Point defects, such as vacancies and interstitials, are responsible for lattice diffusion. Diffusion also takes place along line, planar and surface defects which include grain boundaries, dislocations, and inner and outer surfaces. Grain boundary and dislocation diffusion mechanisms generally have lower activation energies than lattice diffusion, and, as a result, these mechanisms are dominant at lower temperatures in solids with a given microstructure. At higher temperatures, the number of point defects in a solid multiplies, leading to increased volume diffusion which surpasses grain boundary and dislocation diffusion mechanisms.

2.2.3 Lattice diffusion

Lattice or volume diffusion is diffusion through the crystal lattice, which takes place through the movement of point defects. The existence of different types of defects gives rise to different mechanisms of diffusion. The most prominent lattice diffusion mechanisms are the vacancy, interstitial, and interstitialcy. These are briefly discussed in the following subsections.

2.2.3.1 Vacancy mechanism

The vacancy mechanism is facilitated by the presence of vacancy point defects. In the process, an atom on a lattice site hops into a neighbouring vacant lattice site, as illustrated in Figure 2.3.

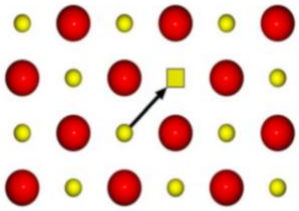

Figure 2.3: Vacancy diffusion mechanism [24].

2.2.3.2 Interstitial mechanism

An interstitial migration process occurs when an ion moves from one interstitial site to a neighbouring interstitial site. This process is illustrated in Figure 2.4.

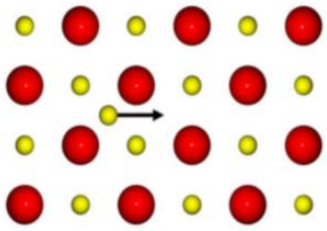

Figure 2.4: Interstitial diffusion mechanism [24].

2.2.3.3 Interstitialcy mechanism

If the energy required to facilitate migration via a direct interstitial mechanism is too great, there is another mechanism by which an interstitial ion can be transported. In this process an interstitial ion moves onto an occupied lattice site. The atom formally occupying the lattice site is forced to form a new interstitial, which can then continue the process (Figure 2.5).

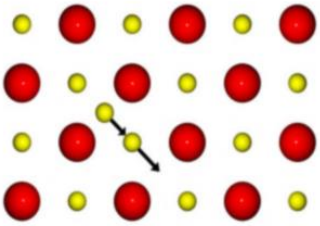

Figure 2.5: Interstitialcy diffusion mechanism [24].

2.2.4 The diffusion coefficient

The diffusion coefficient is the mathematical function that relates the gradient in the concentration of a given species with the flux at a given temperature. As there are several different mechanisms, such as vacancy and interstitial mechanisms, by which matter can be transported through the lattice, the overall diffusion coefficient can be given as the sum of these contributions, as shown in equation (2.2).

$$D_{Total} = D_{Vacancy} + D_{Interstitia} \tag{2.2}$$

Here, D_{Total} is the total diffusion of a species and D_{Vacancy} and $D_{\text{Interstitial}}$, which includes both methods of interstitial diffusion; represent the contributions of the individual diffusion processes. There are numerous factors that combine to determine which of the diffusion processes is responsible for the majority of atomic transport. The two predominant factors are the concentration of the transport-mediating point defects and the ease with which that mechanism can provide transport, often referred to as the diffusivity d_x. Equation (2.3) shows how these factors combine to give the overall diffusion coefficient for a given species,

$$D_{Total} = \frac{n_{Vanancy}}{N} d_{Vanancy} + \frac{n_{Interstitial}}{N} d_{Interstitial} \tag{2.3}$$

where n_{Vacancy} and $n_{\text{Interstitial}}$ are the number of vacancies and interstitials respectively, and d_{Vacancy} and $d_{\text{Interstitial}}$ are the diffusivities of the vacancy and d interstitials. This addresses the diffusivity, whereas the relationship between the diffusivity and the rate constant is given by equation (2.4),

$$d_x = \frac{1}{6} f z a^2 k^{HTST} \tag{2.4}$$

where f is the correlation factor which relates diffusion of actual atoms to the diffusion of the defect, which will be examined more closely in the next section. Additionally, z is the number of equivalent pathways the diffusing mechanism can follow, and a is the jump distance. In order to simplify the expression shown in equation (2.4), the temperature independent terms are collected together in the constant D_0^x for a given process, as shown in equation (2.5).

$$d_x = D_0^x \exp\left(\frac{-E_m}{k_B T}\right) \tag{2.5}$$

If the defect concentration is included, this then gives

$$D = D_0^x exp\left(\frac{-E_m}{k_B T}\right) exp\left(\frac{E_f}{k_B T}\right) = D_0^x exp\left(\frac{-(E_m + E_f)}{k_B T}\right) = D_0^x exp\left(\frac{-E_a}{k_B T}\right) \tag{2.6}$$

where E_a is the overall activation energy for the process. In the majority of experimental investigations of diffusion in the solid state, a plot of 1000 T^{-1} against log D is a straight line and values for E_a and D_0 are obtained from an Arrhenius plot [25].

2.3 Heats of reaction

The heating or annealing of a thin cobalt film in contact with a silicon substrate usually leads to the formation of a cobalt silicide. The phase of the cobalt silicide depends on the temperature of formation, which in turn is determined by the reaction between the two different solid phases in direct contact at the growth interface. These two phases are the Si substrate, comprised of covalently bonded single crystal, and the thin cobalt film, which is usually poly-crystalline.

The cobalt silicides can roughly be grouped in three main classes, namely cobalt-rich silicides, monosilicides and disilicides, which typically start to form at different

temperatures respectively [26]. In the normal formation sequence for cobalt silicides, for example, the cobalt-rich Co_2Si phase forms as the first phase, the monosilicide CoSi forms second, and the disilicide $CoSi_2$ forms third. This last phase is called the "end phase" as no phase changes occur at higher temperatures.

Heats of reaction can be calculated for the interaction between elements and other elements, elements and compound phases, or compound phases and other compound phases. Heats of reaction are equivalent to heats of formation when there is interaction between two elements to form a compound phase, as the standard enthalpy H^o of an element is zero by definition. There is often much confusion when using heats of formation to calculate heats of reaction. This is usually due to the fact that the standard heats of formation ΔH^o for compound phases can be expressed in many different ways for some Co-Si phases, as is illustrated in Table 2.1. Care must be taken to understand what is exactly meant in each case. For instance, a heat of formation (see Table 2.1) for Co_2Si of -115.5 kJ$(mol)^{-1}$ means that 115.5 kJ of energy will be released if Avogadro's number of Co_2Si "molecules" are formed during the reaction between the elements Co and Si. The heat of formation value for Co_2Si, -38.5 kJ $(mol.at.)^{-1}$, is obtained by dividing by the number of atoms in the compound phase. This is sometimes also expressed as kJ $(gm.at.)^{-1}$.

The interpretation in such a case would be that 38.5 kJ is released when the total number of atoms (Co and Si) involved in forming the phase Co_2Si is equal to Avogadro's number. The heats of formation for the Co-Si phases can also be expressed in terms of kJ $(mol.Co.at.)^{-1}$ or kJ $(mol.Si.at.)^{-1}$, as indicated in the last two columns of Table 2.1. In the case of the first compound, for example, it means that 57.7 kJ (115.5/2) of energy is released when Avogadro's number of Co atoms are consumed in forming Co_2Si, whereas 115.5 kJ is released for consuming Avogadro's number of Si atoms.

Table 2.1: Heats of formation of some Co-Si compounds expressed in different ways [27].

Compound	kJ(mol)$^{-1}$	kJ(mol.at)$^{-1}$	kJ(mol.Co.at)$^{-1}$	kJ(mol.Si.at)$^{-1}$
Co_2Si	-115.5	-38.5(3)	-57.7(2)	-115.5(1)
CoSi	-100.4	-50.2(2)	-100.4(1)	-100.4(1)
$CoSi_2$	-102.9	-34.3(3)	-102.9(1)	-51.4(2)

The value in brackets is the number by which the heats of formation, expressed as kJ (mol.at)$^{-1}$, is divided to express the heat of formation in a particular way.

The heats of formation of compounds cannot be used on their own to predict phase formation. This is because concentration at the growth interface is not taken into account. The heats of formation, when expressed per mole of Co or Si atoms (see Table 2.1), are however interesting. It can be seen that the heat of formation for $CoSi_2$ is the most negative when expressed per mole of Co atoms (-102.9 kJ). This means that if there is thin Co on thick Si, the system will eventually thermodynamically go to $CoSi_2$ as formation of this phase will lead to the biggest free energy change. On the other hand, with thin silicon on thick Co, formation of Co_2Si will lead to the biggest free energy change as this phase has the most negative heat of formation (-115.5 kJ) when expressed per mole of silicon atoms.

The heats of reaction (ΔH_R) for the interactions of Co with Si, and CoSi and $CoSi_2$ to form Co_2Si will now be considered. The heats of reaction can be calculated as follows:

(1) $2Co + Si \leftrightarrow Co_2Si$

$2(0) \quad 1(0) \quad 3(-38.5)$

$\Delta H_R = (0 - 115.5)/3 = -38.5$ kJ (mol.at)$^{-1}$

(2) $Co + CoSi \rightarrow Co_2Si$

$1(0) \quad 1(-50.2) \quad 3(-38.5)$

$\Delta H_R = (50.2 - 115.5)/3 = -21.8$ kJ (mol.at)$^{-1}$

(3) $3Co + CoSi_2 \rightarrow 2Co_2Si$

$3(0) \quad 3(-34.3) \quad 6(-38.5)$

$\Delta H_R = (102.9 - 231.0)/6 = -21.3$ kJ $(mol.at)^{-1}$

When calculated as kJ $(mol.at.)^{-1}$, the heats of reaction give the energy when the total number of atoms (Co and Si) expended in the formation of Co_2Si is equal to Avogadro's number. As can be expected, the ΔH_R value is the most negative for the reaction of Co with Si precisely because, as opposed to the other two cases, bonding between Co and Si does not already exist prior to interaction.

Although heats of reaction cannot as such be used to predict phase formation sequence, they do, however, indicate whether a reaction, is thermodynamically possible or not. Consider, for instance, the possibility of $CoSi_2$ formation through the interaction of Co with CoSi.

$Co + 2CoSi \rightarrow CoSi_2 + 2Co$

$1(0) \quad 4(-50.2) \quad 3(-34.3) \quad 2(0)$

$\Delta H_R = (200.8 - 102.9)/5 = +19.6$ kJ $(mol.at)^{-1}$

The heat of reaction is positive and, therefore, the reaction is thermodynamically improbable. This is due to the fact that the reaction leads to less bonding and applies to all reactions, which in turn leads to a product with a composition lying outside the reactants' range of compositions.

2.4 Effective heat of formation (EHF) model

Pretorius [28-30] used a much more fundamental approach in predicting first-phase formation by postulating the effective heat of formation (EHF) model. The model shows how heats of formation, when expressed as effective heats of formation ($\Delta H'$), can be used in conjunction with the composition of the lowest eutectic (or liquidus minimum)

of the binary system to predict the formation of both the first phase and subsequent phases. This model combines thermodynamics with the availability or effective concentration of the elements at the interface.

The driving force for a process like phase formation is provided by the change in the Gibbs free energy, $\Delta G^o = \Delta H^o - T\Delta S^o$ where ΔH^o is the change in enthalpy during the reaction at temperature T i.e. heat of formation, and ΔS is the change in entropy. Since thin-film reactions occur in the solid state, the Gibbs free energy can be approximated by the standard enthalpy of reaction alone, as the change in entropy may be considered close to zero for most systems.

Thus, $\Delta G°_T \approx \Delta H°_{298}$, according to the Neumann-Kopp rule [31], whereby the standard values (at T = 298K) of enthalpy and entropy in solids can be used for thermodynamic calculations at any temperature. An effective heat of formation [30] is defined as:

$$\Delta H' = \Delta H° \left(\frac{\text{effective concentration of limiting element}}{\text{compound cocentration of limiting element}} \right)$$

where ΔH^o and $\Delta H'$ are expressed in kJ $(mol.at)^{-1}$. According to the EHF model, solid-state phase formation is controlled by the effective concentrations of the reacting species at the growth interface.

For example, consider a silicon-cobalt growth interface and the prospective formation of CoSi. If the effective concentration at the interface was 20 at. % Si, then Si would be the limiting species. Obviously the compound concentration of Si in CoSi is 50 at. % and the standard enthalpy value $\Delta H^o = -50.0$ kJ $(mol.at)^{-1}$ for the formation of CoSi. This gives an effective heat of formation value of:

$$\Delta H' = -50.0 \left(\frac{0.2}{0.5} \right) = -20.0 \text{ kJ (mol. at)}^{-1}$$

Figure 2.6 includes the phase diagram [31] and EHF diagram for the Co-Si binary system, showing the linear relationship between effective heat of formation (or heat released) and the concentration of the limiting element. Note that, at the concentration of the liquidus minimum, the phase Co_2Si has the most negative effective heat of formation and would thus be the first phase to form.

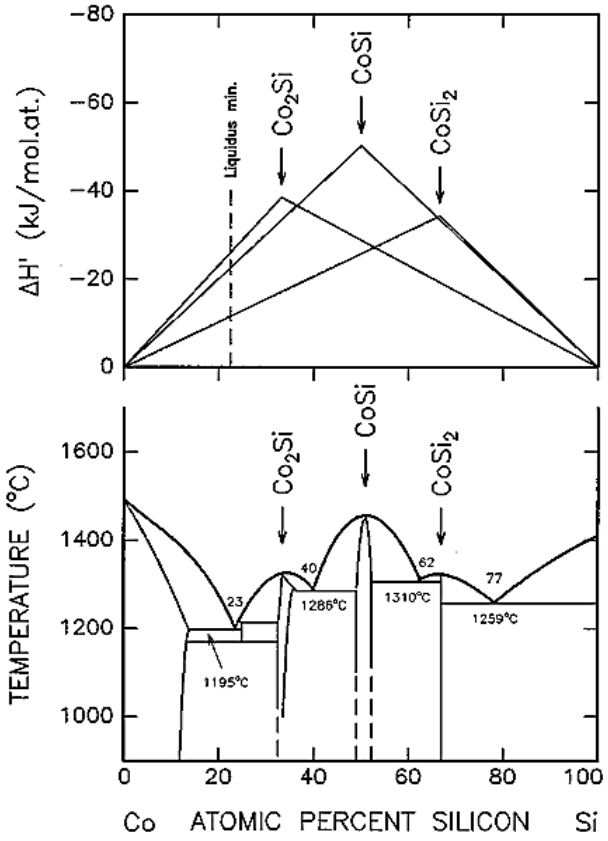

Figure 2.6: Phase diagram and EHF diagram for the Co-Si binary system

The success of the EHF model for predicting phase formation is due to the fact that heats of formation as well as concentration are taken into account. The EHF model has been successfully used in metal-metal, metal-silicon and metal-germanium systems to predict first-phase formation as well as phase formation sequence [30].

2.5 Cobalt silicides formation

2.5.1 Cobalt silicides formation on a Co-Si system

Table 2.2 lists some studies that have been used to investigate the possibility of enhanced formation of cobalt silicides by deposited Co on Si. Normally, when a thin cobalt film is deposited on silicon the phase formation sequence is Co_2Si as first phase, then CoSi and finally $CoSi_2$ [32-35]. Very often, the latter phase is only formed at a relatively high temperature, that is, when a certain nucleation temperature has been exceeded [36-42]. On the other hand, by depositing the cobalt on silicon, the first phase is bypassed, leading to the direct formation of CoSi and $CoSi_2$ on Si(100) and Si(111) substrates [43-46].

Table 2.2: Review of studies concerned with cobalt silicides formation on a Co-Si system.

Cobalt Silicides					
System	**Ambient**	**Si-Type**	**Reference**	**Silicide Formations**	**Temperature**
Si/Co	vacuum	(100)	32, 33	CoSi	350 ºC
				CoSi	375 ºC
				$CoSi_2$	550 ºC
Si/Co	vacuum	(100), (111)	34	CoSi	350 ºC
				Co_2Si	425 ºC
				$CoSi_2$	550 ºC
Si/Co	vacuum	(100)	35	CoSi	420 ºC
				Co_2Si	500 ºC
				$CoSi_2$	700 ºC
Si/Co	vacuum	(100), (111)	36	$CoSi_2$	400-650 ºC
Si/Co	vacuum	(100)	37	$CoSi_2$	800 ºC
Si/Co	N_2	(111)	38	$CoSi_2$	450 ºC
Si/Co	vacuum	(001)	39	$CoSi_2$	500 ºC

Si/Co	vacuum	(100)	40	$CoSi_2$	430 ºC
Si/Co	vacuum	(111)	41	$CoSi_2$	400 ºC
Si/Co	N_2	(001)	42	$CoSi_2$	600 ºC
Si/Co	vacuum	(100)	43	CoSi, $CoSi_2$	450 ºC
Si/Co	vacuum	(111)	44	CoSi	450 ºC
				$CoSi_2$	600 ºC
Si/Co	vacuum	(100)	45	CoSi	450 ºC
				$CoSi_2$	600 ºC
Si/Co	vacuum	(100)	46	CoSi	500 ºC
				$CoSi_2$	600-700 ºC

2.5.2 Cobalt silicides formation through diffusion barrier

The previous section discussed Co-Si systems studied without a barrier layer, whereas this section focuses on Co-Si systems studied in the presence of different barrier layers between Co and Si. Table 2.3 lists the different barrier layers that have been used to investigate the possibility of enhanced formation of cobalt silicides.

Table 2.3: Review of studies on cobalt silicide formation through diffusion barrier layers.

Cobalt Silicides					
System	**Ambient**	**Si-Type**	**Reference**	**Silicide Formations**	**Temperatures**
Si/Ti/Co	N_2	(001)	47	$CoSi_2$	850 ºC
Si/Ti/Co	N_2	(100)	48	$CoSi_2$	550 ºC
Si/Ti/Co	vacuum	(100)	49	$CoSi_2$	600 ºC
Si/Ti/Co	N_2	(100)	50	$CoSi_2$	750-900 ºC
Si/Ti/Co	N_2	(100)	51	CoSi	600 ºC
				$CoSi_2$	700-750 ºC

Si/Ti/Co	vacuum	(100)	52	CoSi	500 ºC
				$CoSi_2$	600-700 ºC
Si/Ti/Co	vacuum	(100)	53	CoSi	420 ºC
				$CoSi_2$	500 ºC
Si/Ti/Co	vacuum	(100)	54	CoSi	500 ºC
				$CoSi_2$	600-700 ºC
Si/Hf/Co	vacuum	(100)	52	CoSi	500 ºC
				$CoSi_2$	800 ºC
Si/Hf/Co	vacuum	(100)	53	CoSi	420 ºC
				$CoSi_2$	600 ºC
Si/Hf/Co	vacuum	(100)	54	CoSi	500 ºC
				$CoSi_2$	800 ºC
Si/Nb/Co	vacuum	(100)	52, 54	CoSi	600 ºC
				$CoSi_2$	800 ºC
Si/Ge/Co	N_2	(100)	55	CoSi	400 ºC
				$CoSi_2$	750 ºC
Si/Mo/Co	N_2	(100)	56	CoSi	600 ºC
				$CoSi_2$	800 ºC
Si/W/Co	vacuum	(100)	57	CoSi	450 ºC
				$CoSi_2$	750 ºC
Si/Cr/Co	N_2	(100)	56	CoSi + $CoSi_2$	560 ºC
Si/Ta/Co	vacuum	(100)	58, 59	CoSi + $CoSi_2$	700 ºC
	vacuum	(111)	58, 59	CoSi + $CoSi_2$	700 ºC
	N_2	(100)	60	$CoSi_2$	600 ºC
Si/Zr/Co	vacuum	(100), (111)	61, 62	$CoSi_2$	600 ºC
Si/Zr/Co	NH3	(100)	61	$CoSi_2$	600 ºC
Si/W/Co	vacuum	(001)	63	$CoSi_2$	600 ºC

It is clear from Table 2.3 that, for the formation of cobalt silicides, most of the previous studies [47-50] have been done by using titanium as a barrier layer, viz. the Si/Ti/Co system and most of the results confirm the formation of $CoSi_2$. This reversal occurs because the Co diffuses through the barrier to react with the Si substrate. In this instance it has been shown that the barrier is actually a ternary Co-Ti-Si compound. Titanium interlayers have proven to be the best epitaxy promoters for the formation of $CoSi_2$. By placing a thin Ti interlayer between the cobalt and silicon, the first phase is bypassed and leads to the direct formation of CoSi and $CoSi_2$ on Si-substrate [51, 54].

As shown in Table 2.3, interlayers composed of hafnium (Hf), niobium (Nb), germanium (Ge), molybdenum (Mo) and tungsten (W) can also be used successfully on Si(100) as a diffusion barrier for CoSi and $CoSi_2$ formation instead of titanium [52-57]. It is also a well-known fact that temperature hardly has any effect on the thermodynamics of solid-state interaction. Forcing interaction at a higher temperature by using a barrier interlayer therefore does not give a thermodynamic reason why the Co_2Si phase is bypassed. The other metals that have received the most attention from researchers as barriers to promote uniform $CoSi_2$ or both CoSi and $CoSi_2$ formation are chromium (Cr), tantalum (Ta), W, and zirconium (Zr) [58-63] (see Table 2.3).

Of particular interest is the addition of an alloying element to the metal so that the silicidation reaction is offered additional degrees of freedom (choice of the element and its concentration) that may be used to tailor the properties of the resultant silicide (texture, grain size) and/or to engineer the reaction path through which the phase of interest is formed. Several authors have studied the effect of alloying elements on the formation and properties of $CoSi_2$ [64-70]. Others have focussed on the use of barrier layers to influence the phase formation sequence. Using a Ti barrier layer, it was reported that from 550 to 900 ºC $CoSi_2$ has been formed [71]. When using a Ta barrier layer between Co and Si, the formation of $CoSi_2$ at 560 ºC and CoSi at 850 ºC was observed [72]. There have been some efforts to grow crystalline $CoSi_2$ above 600 ºC by making using of an Fe layer as a barrier between the cobalt and Si-substrate [73]. In

addition, Zr was used as a diffusion barrier between Si-substrate and Co, leading to the formation of $CoSi_2$ above 600 ºC [74, 75].

Since the Fe-Zr system is known to be a good amorphous forming system [76], it should be very interesting to study the effects of a Co-deposited $Fe_{90}Zr_{10}$ layer, used as a barrier in the Co-Si system with the view to alter the phase formation sequence, on cobalt silicide formation.

References

[1] D. Leong, M. Harry, K.J. Reeson and K.P. Homewood, "A silicon/iron disilicide light emitting diode operating at a wavelength of 1.5 m", *Nature, 387, (1997) 686–688.*

[2] R. T. Tung, J.M. Poate, J.C. Bean, J.M. Gibson and D.C. Jacobson, "Epitaxial silicides", *Thin Solid Films, 93, (1982) 77–90.*

[3] I. P. Jain and G. Agarwal, "Ion beam induced surface and interface engineering", *Surf. Sci. Rep, 66, (2011) 77–172.*

[4] S. L. Zhang and U. Smith, "Self-aligned silicides for Ohmic contacts in complementary metal-oxide-semiconductor technology: $TiSi_2$, $CoSi_2$, and NiSi" *J. Vac. Sci. Technol., A 22, (2004) 1361–1370.*

[5] L. J. Chen, "Silicide technology for integrated circuits", *The Institution of Electrical Engineers., London, UK, (2004).*

[6] M. A. Nicolet and S. S. Lau, "Formation and characterization of transition-metal silicides", *VLSI Electronics: Microstructure Science, 6, (2014) 329.*

[7] S. P. Murarka, "Silicides for VLSI applications", *Academic Press, New York, (1983).*

[8] K. Maex and M. Van Rossum, "Properties of metal silicides", *puplished by INSPE, the Institution of Electrical Engineers, London (1995).*

[9] F. M. Liu, J.H. Ye, B. Ren, Z.L. Yang, Y.Y. Liao, A. See, L. Chan, and Z.Q. Tian, "Raman spectroscopic studies of the formation processes of cobalt silicide thin films", *Thin Solid Films., 471(1), (2005) 257-263.*

[10] D. S. Wilkinson, "Mass transport in solids and fluids", *Cambridge: Cambridge University Press, (2000).*

[11] M. E. Glicksman and M. Glicksman, "Diffusion in solids: field theory", *Solid-State Principles, and Applications. New York: Wiley, (2000).*

[12] P. G. Shewmon, "Diffusion in solids". *Warrendale, PA: Minerals, Metals & Materials Society, (1989).*

[13] H. Mehrer. "Diffusion in Solids", *Springer,155, (2007).*

[14] C. M. Comrie, "Diffusing species and growth interfaces during cobalt disilicide formation", *Nuclear Instruments and Methods in Physics Research B, (1996) 118-122.*

[15] J. E. Mcleod, M. A. E. Wandt, R. Pretorius and C. M. Comrie (1992), "Marker and radioactive silicon tracer studies of PtSi formation", *Journal of Applied Physics 72(1).*

[16] J. W. Christain, "The theory of transformation in metals and alloys". *PART 1: Equilibrium and general kinetic theory, Pergamon Press, Oxford,* (1975).

[17] M. E. Glicksman, "Diffusion on solid", *Wiley, New York, (2000).*

[18] A. J. Walton, "Three phases of matter", *second edn, Oxford, (1982).*

[19] R. Smoluchowski, "Theory of grain boundary diffusion", *Physical Review 87, (1952)* .

[20] J. A. Kenneth , C. Shen, and H. Ralph, "Phillip's Science of Dental Materials", 4th April, 2014.

[21] A. Fick, "V. On liquid diffusion", *The London, Edinburgh, and Dublin Philosophical Magazine and Journal of Science, 10(63), (1855) 30-39.*

[22] R. Brown Phil. *Mag, 4, (1828) 161.*

[23] A. Einstein, *Ann. d. Phys* 17.549 (1905) 19.

[24] D. Smeets, Nucleation diffusion and texture during growth of CoNi-silicides. *Ph.D. Thesis, KU Leuven, Belgium, (2007).*

[25] A. F. Voter, F. Montalenti and T. C. Germann, "Extending the time scale in atomistic simulation of materials", *Annual Review of Materials Research, 32(1), (2002) 321-346.*

[26] O. Kubaschewski and C.B Alcock,"Metallurgical Thermochemistry", *Pergamon Press, Oxford, (1979).*

[27] M. E. Schlesinger, "Thermodynamics of solid transition-metal silicides", *Chemical Reviews, 90.4, (1990) 607-628.*

[28] R. Pretorius, *MRS Proc, 25, (1984) 15.*

[29] R. Pretorius and J. W, Mayer, *Journal of Applied Physics, 81, (1997) 2448.*

[30] R. Pretorius, T.K. Marais and C.C. Theron, *A Review, Mat, Sci. and Eng R10, 1 (1993).*

[31] O. Kubaschewski and C. B. Alcock, "International Series on Materials Science and Technology: Metallurgical Thermo-Chemistry", *Pergamon Press, Oxford, (1979) 294.*

[32] S. S. Lau, J. W. Mayer and K. N. Tu, "Interaction in Co/Si thin-film system kinetics", *Journal of Applied Physics, (1978) 49.*

[33] G. Ottaviani, K. N. Tu, P. Psaras and C. Nobili, "In situ resistivity measurement of cobalt silicide formation", *Journal of Applied Physics 62(1),* (1987) *2290-2294.*

[34] M. A. Nicolet, S. S. Lau, N. G. Einspruch and G. B. Larrabee, "VLSI electronics: microstructure science", *Academic, New York, 6, (1983) 329.*

[35] J. Y. Shim, S. W. Park and H. K. Baik, "Silicide formation in cobalt/amorphous silicon, amorphous CoSi and bias-induced CoSi films", *Thin Solid Films, 292(1), (1997) 31-39.*

[36] D. H. Zhu, Y. G. Chen, and B. X. Liu, "Formation of a $CoSi_2$ layer by Co ion implantation using a metal vapor vacuum arc ion source", *Nuclear Instruments and Methods in Physics Research Section B: Beam Interactions with Materials and Atoms, 101(4), (1995) 394-399.*

[37] C. T. Joensson, I. A. Maximov, H. J. Whitlow, V. Shutthanandan, L. Saraf,D. E. McCready and S. Thevuthasan, "Synthesis and characterization of cobalt silicide films on silicon", *Nuclear Instruments and Methods in Physics Research Section B: Beam Interactions with Materials and Atoms, 249 (1), (2006) 532-535.*

[38] H. C. Cheng and M. H. Juang, "Growth of single-crystalline $CoSi_2$ on (111) Si at low annealing temperatures by a nonultrahigh vacuum method", *Journal of Crystal Growth, 115(1), (1991) 572-578.*

[39] L. J. Schowalter, J. R. Jimenez, L. M. Hsiung, K. Rajan, S. Hashimoto, R. D. Thompson and S. S. Iyer, "Control of misoriented grains and pinholes in $CoSi_2$ grown on Si (001)", *Journal of Crystal Growth, 111(1), (1991) 948-956.*

[40] L. Haderbache, P. Wetzel, C. Pirri, j. C. Peruchetti, D. Bolmont and G. Gewinner, "Epitaxial growth of $CoSi_2$ on Si (100)", *Thin Solid Films, 184(1), (1990) 317-323.*

[41] L. Haderbache, P. Wetzel, C. Pirri, J. C. Peruchetti, D. Bolmont and g. Gewinner, "Quantum well states in a metal-semiconductor system: $CoSi_2$/Si (111)", *Thin Solid Films, 184(1), (1990) 365-371.*

[42] M. H. Juang and H. C. Cheng, "Film thickness effect on the epitaxial growth of $CoSi_2$ on Si (111)", *Thin Solid Films, 215(1), (1992) 71-75.*

[43] F. M. D'Heurle and C. S. Petersson, "Formation of thin films of $CoSi_2$: Nucleation and diffusion mechanisms", *Thin Solid Films, 128(3), (1985) 283-297.*

[44] W. T. Lin, K. C. Wu and F. M. Pan, "A new epitaxial orientation of $CoSi_2$ on (111)Si", *Thin Solid Films, 215, (1992) 184-187*

[45] C. Krontiras, J. Salmi, L. Grönberg, I. Suni, J. Heleskivi and A. Rissanen. Measurements on the electrical transport properties in $CoSi_2$ and $NiSi_2$ formed by thin film reactions. *Thin Solid Films, 125(1), (1985) 93-99.*

[46] M. Novaković, M. Popović, K. Zhang, K. P. Lieb and N. Bibić, "Silicide phases formation in Co/c-Si and Co/a-Si systems during thermal annealing", *Applied Surface Science, 295, (2014) 158-163.*

[47] A. Alberti, F. La Via and F. Rimini, "Reaction and thermal stability of cobalt disilicide on polysilicon resulting from a Si/Ti/Co multilayer system", *Journal of Vacuum Science & Technology B, 17(4), (1999) 1448-1455.*

[48] M. L. A. Dass, D. B. Fraser and C. S. Wei, "Growth of epitaxial $CoSi_2$ on (100)Si", *Applied physics letters, 58(12), (1991) 1308-1310.*

[49] A. Vantomme, S. Degroote, J. Dekoster and G. Langouche, "Epitaxy of $CoSi_2$ Si(100): from Co/Ti/Si (100) to reactive deposition epitaxy", *Applied Surface Science, 91(1), (1995) 24-29.*

[50] P. Liu, B. Li, Z. Zhou, C. Lin and S. Zou, "Growth of epitaxial $CoSi_2$ film on Si(100) substrate induced by an interfacial Ti layer", *Materials Letters, (17), (1993) 383-387.*

[51] A. Lauwers, R. J. Schreutelkamp, B. Brijs, H. Bender and K. Maex, "Technological aspects of epitaxial $CoSi_2$ layers for CMOS", *Applied Surface Science, 73, (1993) 19-24.*

[52] Y. Kwon, C. Lee, H. K. Kang and D. L. Bae. Silicidation of Co/Ti, Co/Nb, and Co Hf bilayers on the Si (100) substrate. *Journal of the Korean Physics, 34, (1999) S499-S503.*

[53] Y. Kwon and C. Lee, "Silicidation behaviors of Co/Ti and Co/Hf bilayers on doped polycrystalline Si substrate", *Materials Science and Engineering: B, 65(3), (1999)187-193.*

[54] Y. Kwon and C. Lee, "Formation of epitaxial cobalt silicide films on (100)Si using Co/Ti, Co/Nb, and Co/Hf bilayers", *Materials Chemistry and Physics, 63(3), (2000) 202-207.*

[55] C. Detavernier, R. L. Van Meirhaeghe, F. Cardon and K. Maex, "$CoSi_2$ nucleation in the presence of Ge", *Thin Solid Films, 384(2), (2001) 243-250.*

[56] C. Detavernier, R. L. Van Meirhaeghe, F. Cardon, K. Maex, H. Bender, B. Brijs and W. Vandervorst, "Formation of epitaxial $CoSi_2$ by a Cr or Mo interlayer: Comparison with a Ti interlayer", *Journal of Applied Physics, 89(4), (2001) 2146-2150.*

[57] F. M. Yang and M. C. Chen, "Formation of cobalt silicide under a passivating film of molybdenum or tungsten", *Journal of Vacuum Science & Technology B, 9*(3), (1991) 1497-1502.

[58] G. Briskin, J. Pelleg and M. Talianker, "Phase formation between co-deposited Co-Ta thin film and single-crystal silicon substrates", *Thin Solid Films, 288(1), (1996) 132-138.*

[59] J. Pelleg, "Formation of Co and Ta silicides on Si(111) and Si(100) substrates from co-deposited Co and Ta thin films", *Thin Solid Films, 325(1), (1998) 60-71.*

[60] J. S. Byun, D. H. Kim, W. S. Kim and H. J. Kim, "Epitaxial growth of $CoSi_2$ layer on (100)Si and facet formation at the $CoSi_2$/Si interface", *Journal of Applied Physics, 78(3), (1995) 1725-1730.*

[61] J. P. W. B. Duchateau, A. E. T. Kuiper, M. F. C. Willemsen, A. Torrisi and van G. J. der Kolk, "The reaction of amorphous Co–Zr layers with Si(100) and SiO_2 substrates by annealing in vacuum and NH_3, *Journal of Vacuum Science & Technology B, 9(3), (1991) 1503-1510.*

[62] D. Kim and H. Jeon, "The growth of $CoSi_2$ using a Co/Zr bilayer on different Si substrates", *Thin Solid Films, 346(1), (1999) 244-250.*

[63] A. H. Reader, J. P. W. B. Duchateau, J. E. Crombeen, E. P. Naburgh and M. A. J. Somers, "The formation of epitaxial $CoSi_2$ thin films on (001) Si from amorphous Co-W alloys", *Applied Surface Science., 53, (1991) 92-102.*

[64] C. Detavernier, R. L. Van Meirhaeghe, F. Cardon and K. Maex, "$CoSi_2$ nucleation in the presence of Ge", *Thin Solid Films, 384(2), (2001) 243-250.*

[65] C. Detavernier, R. L. Van Meirhaeghe, F. Cardon, K. Maex, H. Bender, B. Brijs and W. Vandervorst, "Formation of epitaxial $CoSi_2$ by a Cr or Mo interlayer: Comparison with a Ti interlayer", *Journal of Applied Physics, 89(4), (2001) 2146-2150.*

[66] C. Lavoie, C. Cabral Jr, F. M. d'Heurle, J. L. Jordan-Sweet and J. M. E. Harper, "Effects of alloying elements on cobalt silicide formation", *Journal of Electronic Materials, 31(6), (2002) 597-609.*

[67] C. Detavernier, R. L. Van Meirhaeghe, F. Cardon and K. Maex, "Influence of mixing entropy on the nucleation of $CoSi_2$", *Physical Review, B 62(18), (2000) 12045.*

[68] C. Detavernier, R. L. Van Meirhaeghe, F. Cardon, K. Maex, W. Vandervorst and B. Brijs, "Influence of Ti on $CoSi_2$ nucleation", *Applied Physics Letters, 77(20), (2000) 3170-3172.*

[69] B. I. Boyanov, P. T. Goeller, D. E. Sayers and R. J. Nemanich, "Film thickness effects in the Co–Si_{1-x} Ge_x solid phase reaction", *Journal of Applied Physics, 84(8), (1998) 4285-4291.*

[70] D. B. Aldrich, F. M. d'Heurle, D. E. Sayers and R. J. Nemanich, "Interface stability of $Ti(SiGe)_2$ and SiGe alloys: Tie lines in the ternary equilibrium diagram", *Physical Review B, 53(24), (1996) 16279.*

[71] P. Liu, B. Z. Li, Z. Sun, Z. G. Gu, W. N. Huang, Z. Y. Zhou and G. A. Rozgonyi, "Epitaxial growth of $CoSi_2$ on both (111) and (100) Si substrates by multistep annealing of a ternary Co/Ti/Si system", *Journal of Applied Physics, 74(3), (1993) 1700-1706.*

[72] C. Detavernier, C. Lavoie and R. L. Van Meirhaeghe, "$CoSi_2$ formation in the presence of Ti, Ta or W", *Thin Solid Films, 468(1), (2004) 174-182.*

[73] C. Detavernier, R. L. Van Meirhaeghe, F. Cardon and K. Maex, "Influence of mixing entropy on the nucleation of $CoSi_2$", *Physical Review B, 62(18), (2000) 12045.*

[74] J. P. W. B. Duchateau, a. E. T. Kuiper, M. F. C. Willemsen, A. Torrisi and G. J. van der Kolk, "The reaction of amorphous Co–Zr layers with Si (100) and SiO_2 substrates by annealing in vacuum and NH_3", *Journal of Vacuum Science & Technology B, 9(3), (1991) 1503-1510.*

[75] D. Kim and H. Jeon, "The growth of $CoSi_2$ using a Co/Zr bilayer on different Si substrates", *Thin Solid Films, 346(1), (1999) 244-250.*

[76] A. Iljinas, D. Milčius and J. Dudonis, "Deposition of amorphous Fe–Zr alloys bymagnetron co-sputtering", *Vacuum, 81(10), (2007) 1213-1215.*

CHAPTER 3

EXPERIMENTAL TECHNIQUES

3.1 Introduction

This chapter discusses the main analytical methods and experimental procedures that were used to analyse the samples utilized in this study. These instruments and techniques include the Compact Arc Melter MAM-1, electron beam or (E-beam) evaporation**,** sputter deposition**,** 3.2.3.1 Molecular beam epitaxy (MBE), Rutherford backscattering spectrometry (RBS), Auger electron spectroscopy (AES), scanning electron microscope (SEM), fracture cross-section, and X-ray diffraction (XRD). The procedures that were used to run experiments are described in detail.

3.2 Barrier layer fabrication

3.2.1 CrZr by arc-melting

3.2.1.1 The Compact Arc-Melter (MAM-1)

Arc-melting is a fast and clean way of producing alloys from electrically conductive materials. The raw materials are placed on a water-cooled hearth in a vacuum chamber. After evacuation, the chamber is refilled with Argon to be employed as an inert working gas. An electric arc is produced with a pointed electrode, which heats the raw materials above their melting point, fusing them into an alloy droplet. The facility operates a MAM-1 arc-melter manufactured by Edmund Bühler GmbH, Germany, as shown in Figure 3.1.

The Compact Arc, designed for melting samples from 5 g to 15 g and up to 3500 °C, is sufficient for most laboratory purposes. It has a small melting chamber, which ensures good and fast melting [1]. Samples of nominal composition CrZr were prepared and melted in an argon atmosphere using the MAM-1 arc-melter at the University of Pretoria, as shown in Figure 3.1.

Figure 3.1: The Compact Arc-Melter (Edmund Bühler GmbH MAM-1) at the University of Pretoria.

In this case, the Compact Arc-Melter MAM-1 was used to combine a mixture composed of 85% Zr and 15% Cr to prepare $Cr_{15}Zr_{85}$ as an amorphous CrZr alloy to be used for use as a diffusion barrier. The chromium and the zirconium are put on the cold copper base of the chamber, as shown in Figure 3.2. Then, to prevent the risk of oxidation during melting, the air in the chamber is replaced by argon. A rotary pump is used to empty the chamber and argon is injected until a pressure of 800 mbar is reached. A potential difference is supplied between a tungsten tip and the sample, which generates an electric arc that heats the sample at a high temperature. The arc-melter is designed to enable high temperatures if using it at the maximum power [2]. After the metals have melted, the chamber is again evacuated to avoid the escape of toxic gases, then air is injected to increase the pressure up to 1 bar and the alloy can be removed [3].

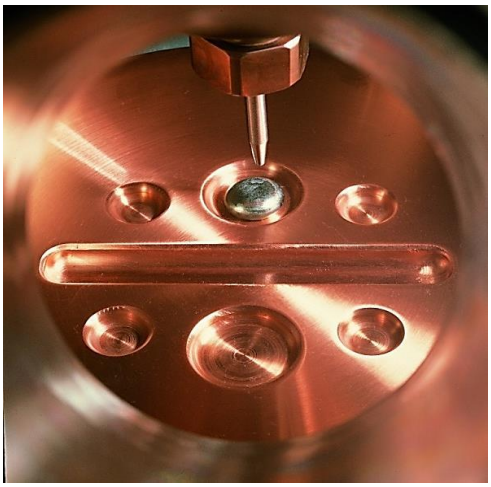

Figure 3.2: Interior view of the Compact Arc-Melter containing a prepared sample.

3.2.1.2 The E-beam evaporation technique

The CrZr was evaporated by using the E-beam evaporation technique. The simplest method to deposit metals on a substrate is to heat and evaporate it. The vapour can then condense on the substrate. This is possible for most fusible materials. There are several reasons why evaporation is performed under vacuum atmosphere. Under low pressure, the evaporation process starts at a much lower temperature than at atmospheric pressure. Consequently, much less energy is required to melt the same material. In addition, vacuum prevents material conversions with residual gases [4]. Evaporation of the material can be done, for example, by using resistance, inductive or electron beam heating. Most applications for thin films use these methods or variants of them. The low-end method of heating is resistance heating or inductive heating (see Figure 3.3), in which the material is placed in a crucible and heated by either an electric current or high frequency. Most materials can be melted in this way if the melting temperature of the crucible is higher than that of the material intended for evaporation. For of this reason, tungsten, tantalum, or molybdenum is used for the crucible. Ideally, the crucible should not contaminate, react with the evaporation material, nor release gases at the process

temperature. Crucibles are made of thin sheet metal and hundreds of amperes are able to flow through them [5].

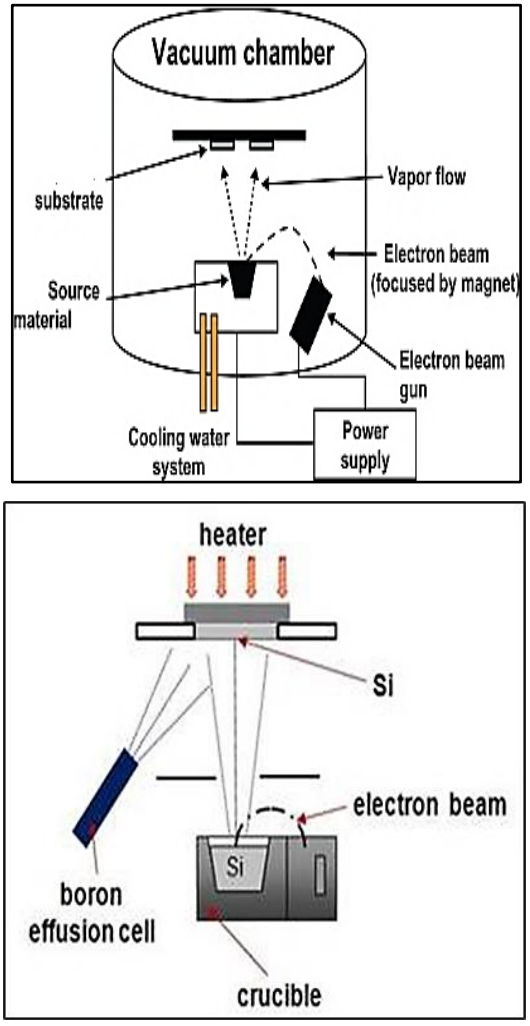

Figure 3.3: A simple diagram of electron beam evaporation [6].

3.2.1.3 E-beam evaporation setup

An E-beam system was used to evaporate the $Cr_{15}Zr_{85}$ and deposit it as an alloy layer on Si-substrate. E-beam deposition depends on temperature vapour pressure. Although anticipated different rates of evaporation thought perhaps substrate alloy could still be

formed, but because the vapour pressure temperature of Cr is less than that of Zr, as shown in Table 3.1, only Cr come off without Zr on Si-substrate.

When Cr and Zr were chosen to form an alloy layer on Si-substrate, it was even a little bit of Zr with mostly formation of Cr, regardless of the difference in the temperature vapour pressure of Cr and Zr. Initially the proportion of Zr was 85 % and Cr was 15 %, but during deposition the Cr displaced the Zr, leaving no percentage of Zr. Additionally, the RBS results showed that only Cr had been deposited. Therefore, since a CrZr alloy was not deposited on the Si-substrate, this attempt was discarded to search for another procedure.

Table 3.1: The temperature vapour pressures of Cr and Zr [7].

Name	**symbol**	**Melting point(°C)**	**Temperature(°C) Vapor Pressure**	
			10^{-8} torr	10^{-4} torr
Chromium	Cr	1875	837	1157
Zirconium	Zr	1851	1748	1987

3.2.2 FeZr by solid-state diffusion

3.2.2.1 Sputter deposition

The second attempt made use of solid-state interdiffusion, leading to creation of an alloy was sputter deposition. Fe and Zr multilayers were deposited on a single-crystalline Si substrate using DC sputtering technique. By starting heat up the Fe and Zr multilayer to get an a homogenized amorphus alloy of FeZr.

The deposition of thin films involves the vaporisation of material from a solid source to produce atomic, molecular, or ionic species. These species are then transported through

a medium, such as vacuum, to a substrate where condensation and accumulation of material occurs to form a solid deposit [8].

Sputtering is one of the most common forms of physical vapour deposition (PVD) techniques. Sputter deposition of thin films promotes uniformity, good adhesion to the substrate, and a smoother surface at lower deposition temperatures. A thin film prepared by any deposition method consists of three parts: the surface layer, the film and the film interface [9]. The sputter deposition process involves the physical ejection of atoms from an electrode target surface by energetic ion bombardment. This involves scraping off surface atoms, which is why sputtering is also used to clean target surfaces.

Physical sputtering occurs via momentum transfer by ions (Ar^{+}), which are accelerated by a plasma while bombarding a target. The dislodged target atoms, which are in vapour phase, are thereafter transported and deposited onto the substrate. The sputtered atoms are allowed to condense on a substrate for a particular duration to form a thin film [10]. The film deposition rate depends on the amount of current and sputtering pressure. Sputtering is usually done in an evacuated chamber at pressures typically in the range of 10^{-4} to 10^{-7} Torr, as shown in Figure 3.4.

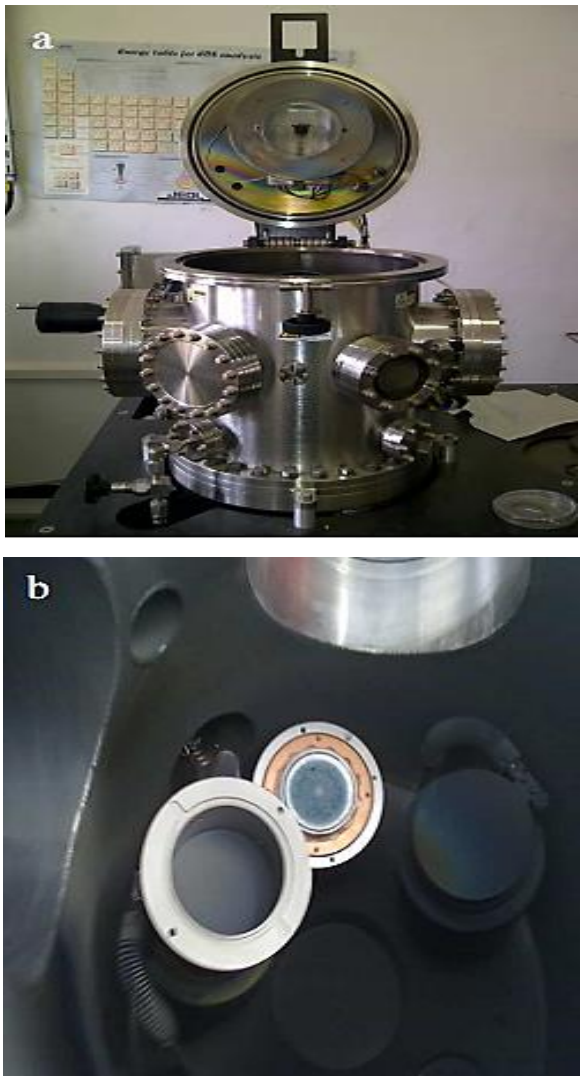

Figure 3.4: (a) The sputtering chamber with the lid open showing the heating lamps and rotating sample-plate holder, (b) Interior of the sputtering chamber showing an opened target shutter with the target at the top, and a closed target shutter.

The sputtering process can be categorised into direct current (DC), radio frequency (RF), magnetron, and reactive sputtering. RF or DC sputtering can be applied depending on target material characteristics. For electrically conductive materials like metals, the DC diode configuration is usually applied. In this configuration, the sputtering target (source of material to be deposited) is used as the cathode electrode needed to sustain the glow discharge and the substrate acts as an anode connected to ground. DC diode

configuration is simple and is, therefore, the most commonly used sputtering configuration, which is illustrated in Figure 3.5.

In the case of insulators and semiconductors, accumulation of surface charge occurs at the target, which cannot be conducted away electrically and prevents ion bombardment. Consequently, DC methods cannot be used to sputter non-conducting targets [11]. In an RF sputtering setup, a potential, with a large peak-to-peak voltage, is capacitively coupled to an electrode. The power supply is operated at a high frequency, typically around 13.56 MHz or multiples of 2 or 3 [12]. For a fraction of the RF cycle, the cathode and anode terminal polarities are electrically reversed to eliminate the charge build-up [9]. This makes this configuration applicable for sputtering insulators and semiconductors.

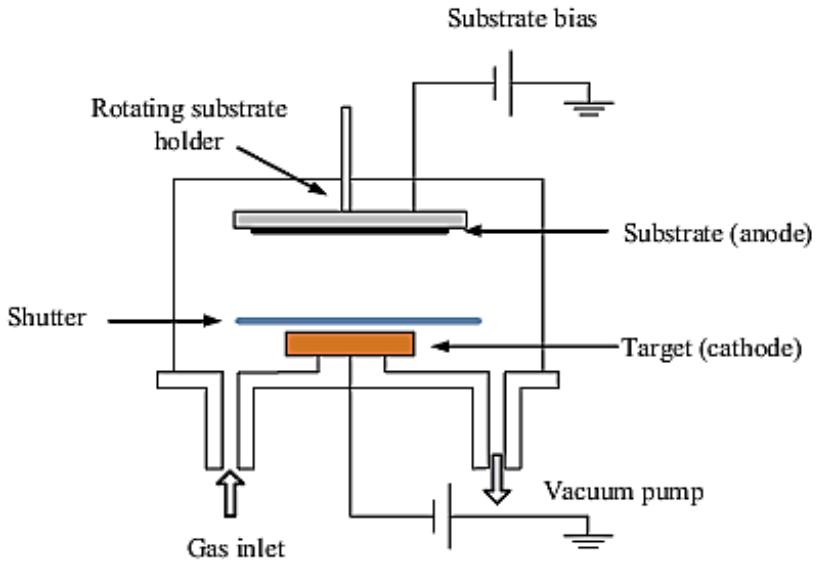

Figure 3.5: DC sputtering setup [13].

The AJA International Inc. Orion 5 sputtering system was used to deposit Fe and Zr films as sandwich on a Si wafer. The Si wafer was mounted on a rotating sample holder to ensure a uniform deposited layer and the target-to-substrate distance was set at

34 mm. The sputtering chamber was degassed by heating it to approximately 500 °C for about an hour while evacuating it. This was done to remove water vapour, and gaseous and metallic contaminants from the chamber. The chamber was pumped down to a base pressure of 10^{-6} Torr and then refilled with Ar gas to a pressure of 10^{-3} Torr.

The steps of preparation and analysis of the Zr/Fe/Si samples are shown in Figure 3.6, and the deposition of the Fe/Zr thin films on the Si substrate is decscribed in Table 3.2.

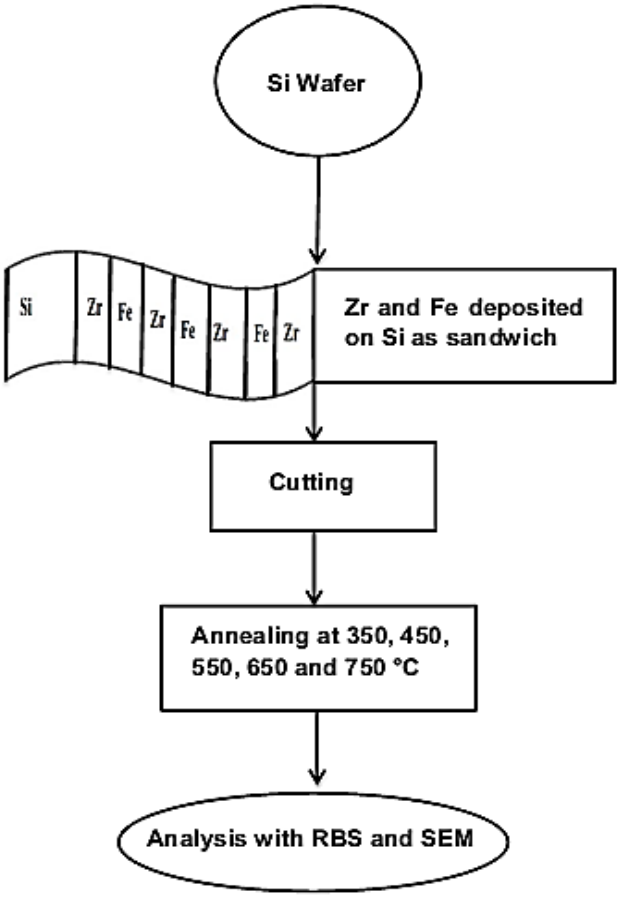

Figure 3.6: Schematic diagram of preparation and analysis of the Zr/Fe/Si samples.

Table 3.2: The FeZr/Si samples preparation.

Layers	**Thickness (nm)**	**Sputter time seconds**	**Power (W)**
Zr	3	20	100
Fe	46	56	150
Zr	10	40	100
Fe	46	56	150
Zr	10	40	100
Fe	46	56	150
Zr	10	40	100
Si-substrate	30000 Å		

This attempt was also discarded to search for another procedure because the presence of so much O_2 in the Zr was problematic and an FeZr alloy was not deposited on the Si-substrate after annealing.

3.2.3 FeZr by co-evaporation

3.2.3.1 Molecular beam epitaxy (MBE)

MBE technology is suitable for the preparation of compound structures in which the various layers are very thin and have differing compositions and properties. The junctions between the layers have to be very smooth. Thicknesses as low as one monolayer are possible to prepare by this controlled growth. The growth method described here is based on the use of effusion sources charged with pure solid elements.

Selected elements are heated in vacuum furnaces called effusion cells. Evaporated atoms and molecules leave the cells in collimated beams and impinge on a heated surface of a mono-crystalline wafer. Here, they enter different processes (physical adsorption,

chemisorption, and migration), undergo transformation (dissociation, association, etc.) and, finally, form a mono-crystalline lattice. Molecular beams can be interrupted by shutters placed in front of the cell orifices. In this way, it is possible to change the composition and properties of grown layers. Some cells usually contain dopant elements (Si and Be for n^- or p^- doping in GaAs), which control the type of electrical conductivity. The growth process is realised in an ultra-high vacuum chamber with ultimate pressure in the order of 10^{-11} mbar. The chamber is equipped with a number of effusion cells, a manipulator for sample heating (0-1000 °C) and azimuthal rotation, as well as an electron gun and screen for reflection high-energy electron diffraction (RHEED) and other accessories. The inner chamber walls are surrounded by cryopanels, which are cooled by LN_2 (-197 °C) during the growth.

MBE is an ultra-high vacuum (UHV) atomic-layer by atomic-layer crystal growth technique based on a reaction of molecular or atomic beams with a heated crystalline substrate (Figure 3.7). MBE is capable of producing extremely high purity and highly crystalline thin films with precise control over composition, doping, and interfaces in the fraction of nanometer range in the growth direction with precise lateral uniformity. MBE is widely employed to grow semiconductor, metal, insulator, and ceramic thin films [14, 15].

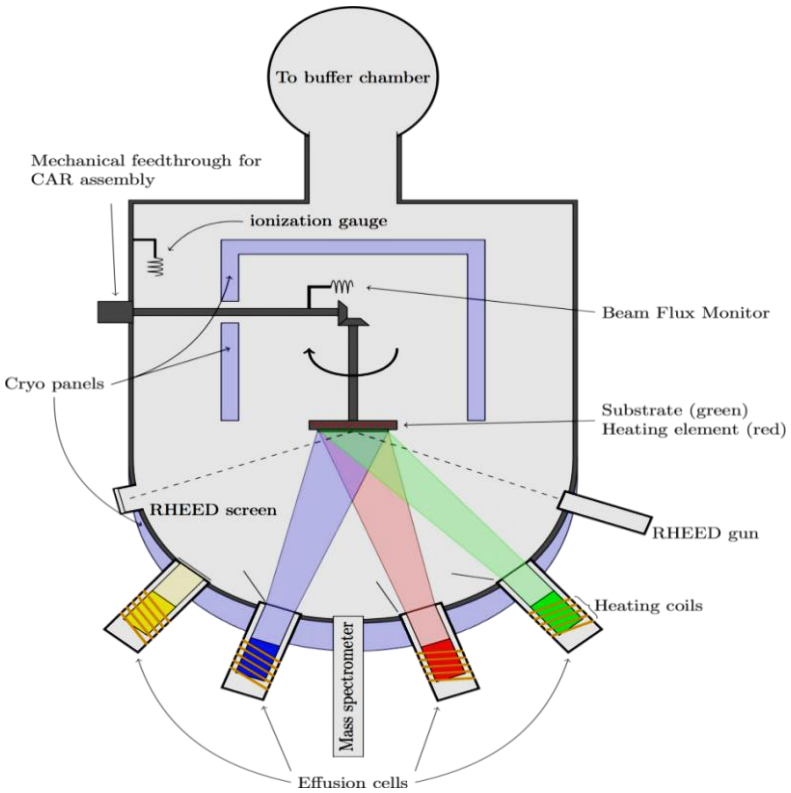

Figure 3.7: Illustration of the chamber of an MBE system [16].

3.2.3.2 Deposition setup

A 50 mm diameter Si(100) single-crystalline p-type substrate was cleaned in solvents and etched in a 4% HF solution prior to being mounted in an MBE chamber. A wedge of $Fe_{90}Zr_{10}$ was co-deposited onto the Si by slowly moving the shutter over the sample during growth. This resulted in a film varying in thickness across the wafer ranging from zero thickness to a total nominal $Fe_{90}Zr_{10}$ thickness of 200 nm at the other end of the wedge, as shown in Figure 3.8. The geometry of the e-guns in the MBE was such that Fe was deposited perpendicular to the main shutter before the substrate, while the Zr e-gun was at a slight angle. This resulted in an enrichment of Zr at the top of this wedge layer. On top of the wedge, a uniform 126 nm Co film was deposited. The base pressure of the

deposition system was less than 2×10^{-11}Torr and never exceeded $2x10^{-9}$ Torr during growth. Following deposition, the samples were cut into approximately 5×5 mm pieces with a diamond scriber and placed in a desiccator when not being subjected to analysis. In this study, the results obtained from different thicknesses of FeZr layers, serving as the diffusion barrier layer between Co and Si-substrate will be assessed.

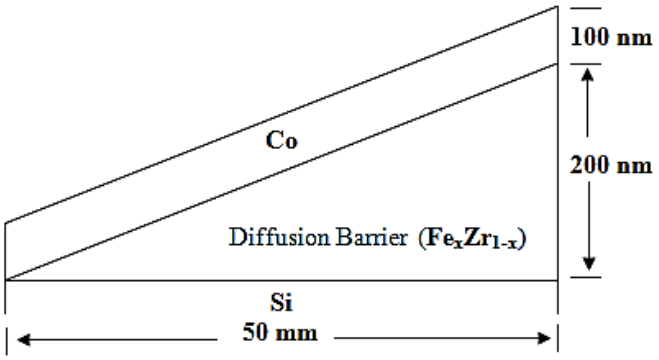

Figure 3.8: Schematic diagram showing the thin film wedge-shaped layers on a wafer.

3.2.3.3 Preparation and analysis of the Co/FeZr/Si system

The deposition of Co/FeZr/Si thin films was prepared using the MBE technique. The stages involved in the preparation and analysis of the Co/FeZr/Si samples are outlined in the flowchart shown in Figure 3.9.

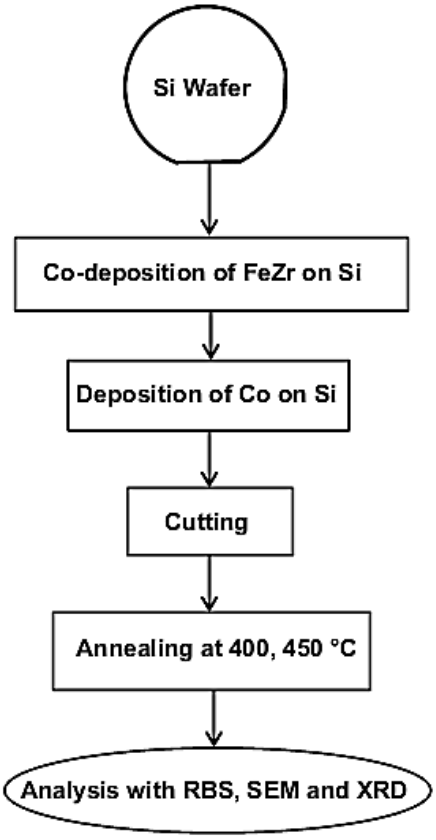

Figure 3.9: Schematic diagram of preparation and analysis of the Co/FeZr/Si samples.

3.3 Annealing of samples

For all solid-state reactions, the annealing stage is the most important and, in this study, isochronal annealing was employed. The vacuum tube furnace was heated up to 1000 °C for 1 hour to clean up the lingering impurities from any previous annealing before the sample was placed within. The unannealed samples were annealed at high vacuum (HV) conditions in a quartz tube furnace. Figure 3.10 presents a schematic diagram of the tube furnace annealing system at the University of Pretoria. The turbo pump shown in the diagram provides high vacuum; that is, the vacuum gauge reads a pressure of approximately 10^{-8} mbar. A thermocouple was placed close to the sample to measure its temperature, which was pre-set prior to switching on the furnace while it was in the out

position. Once the oven had stabilised at the required annealing temperature, it was dragged over the quartz tube until the sample was in the middle of the oven. This step ensured that the sample quickly reached the required temperature. At the same time, the data acquisition program was running on the computer. After the annealing, the furnace was pulled away from the quartz tube to allow the sample to cool down to room temperature.

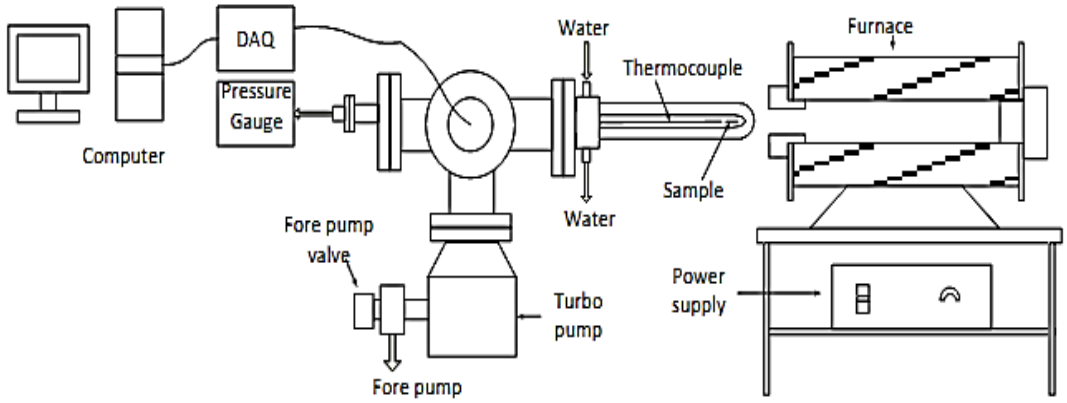

Figure 3.10: Tube furnace annealing system consisting of data logging system, vacuum pumps and furnace [13].

The annealing process was controlled with the use of a computer programme and executed in two steps. The first step usually entails simply heating the sample for as little as 3-6 hours and then cooling it down in order to avoid any damage or demolition. In this case, the first heating duration consisted of five hours and the second of 19 hours, which brought the total heating duration to 24 hours. After the initial heating, there was no need to break down the furnace and thus the process of heating the sample continued for the second step. The annealing strip chart provides a clear understanding of the temperature levels for second step, annealing and cooling down processes. The annealing curves shown in Figure 3.11 are at 400 °C and 450 °C for 19 hours.

The sample was annealed isochronally, using the tube furnace. The annealing temperature ranged was from 400 °C to 450 °C. RBS, SEM and XRD were used to investigate changes on the sample after every annealing.

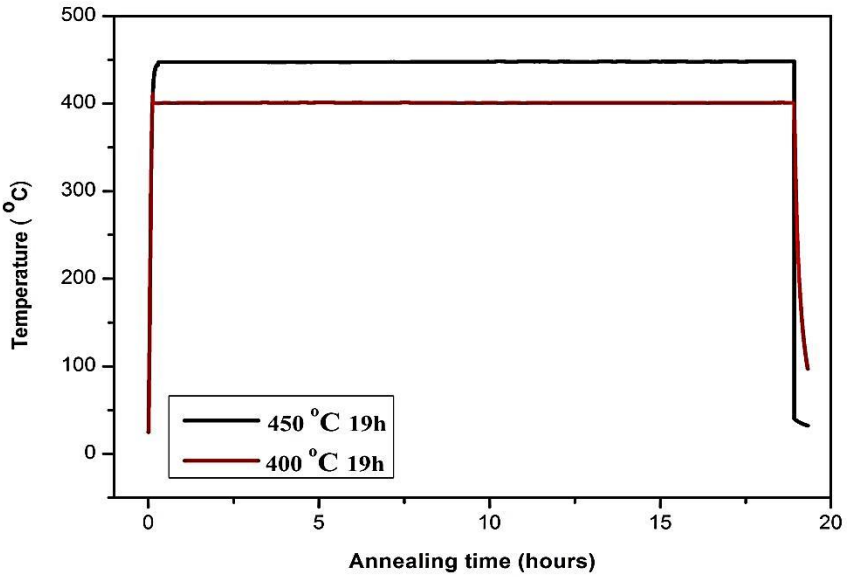

Figure 3.11: Annealing curves for samples at temperatures of 400 °C and 450 °C for 19 h versus time (hours).

3.4 Rutherford backscattering spectrometry

In Rutherford backscattering spectrometry (RBS), charged particles like He^+ or H^+ are incident on a target material. The charged particles used in this study were helium ions (He^+). The first occurrence of backscattering was carried out by Geiger and Marsden in 1909 [17], the effects of which were later explained by the Rutherford atomic model in 1911 [18]. But it was during the 1960s that RBS became an important and commonly applied technique for the study of thin films, silicide formation, and diffusion studies [19]. The technique has the advantage of allowing analysis to be done reliably and with almost no destruction [20]. RBS is a fast and direct method for obtaining element depth profiles in solids [19, 20]. The RBS technique, simple in nature, is a non-destructive

analytical tool for the microanalysis of materials, and the most suitable for measuring heavy elements on light substrates [21]. The well-collimated beam of energetic particles is shot into a high-vacuum scattering chamber containing the target [22]. The energy of the backscattered ions is then measured from scattering events occurring at both the surface and a particular depth. The typical backscattering angles used are optimised for mass resolution at $160° \leq \theta \leq 170°$ [19].

When a beam of mono-energetic ions is incident on a material, some of the projectile ions will be elastically scattered in two different ways, depending on the energy and velocity of the ion. The interactions occur either with the orbital electrons or the nuclei of the target atoms. The RBS technique is based on the principle that the energy of an elastically backscattered particle depends on the mass of the target atom (kinematic factor), the depth at which the scattering event takes place (energy loss into and from the point of interaction) and the scattering cross-section [23]. The RBS technique can determine the masses of the elements used and thus their chemical composition in a sample, and their depth profiles over distances as small as a few nanometres to about 2 μm for incident He^+ ions from the surface. This technique allows for the determination of crystalline structure through channelling experiments [24 , 25]. The RBS technique is best suited for analysing thin films and multi-layered structures, and can determine the composition and depth profiles with a depth resolution of typically ten nanometres over a depth of hundreds of nanometres without eroding the material surface [26 , 27]. The elemental composition of a sample may be determined to very good precision, since RBS is very sensitive to heavy elements in the order of parts per million. The signals between peaks can convey information about the diffusion, interface creation and phase changes. This extends the RBS technique's capabilities into the measurement of the kinetics of transformation in thin film structures.

The setup of the accelerator at the University of Pretoria, as illustrated in Figure 3.12, was capable of producing a He^+ beam with an energy of 2.0 MeV, but the energies used in this study were 1.4 and 1.6 MeV. Lower beam energy in conventional RBS has been

known to extend the depth resolution and sensitivity of the RBS technique, as observed by Brijs et al. [28].

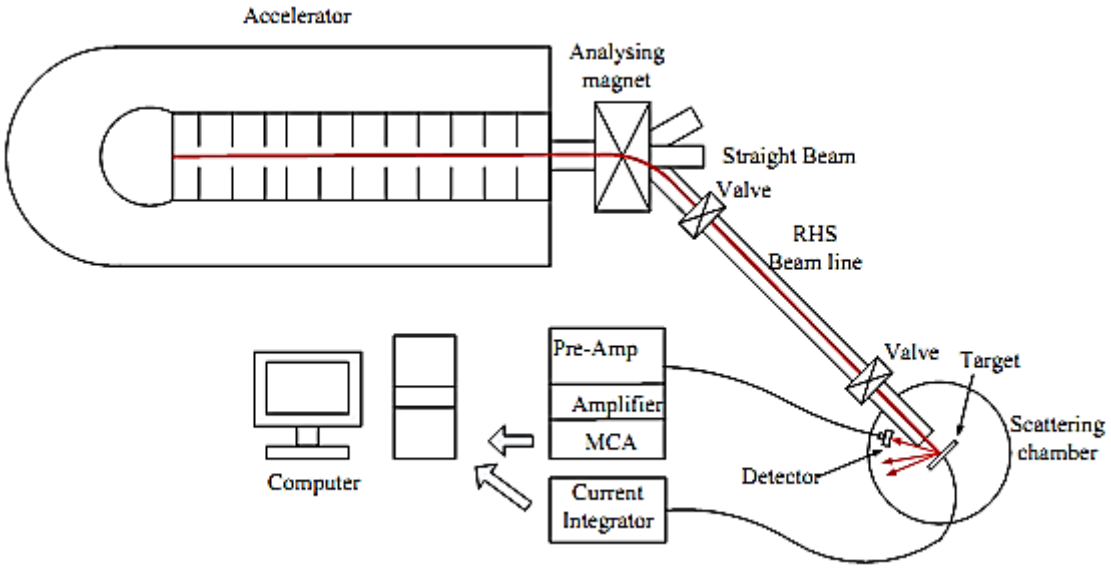

Figure 3.12: Schematic overview of the RBS setup at the University of Pretoria [13].

A beam of mono-energetic (in the MeV range) collimated He^{+} particles impinge on a target and a fraction of the backscattered particles is analysed with a silicon barrier detector placed at a fixed scattering angle. The scattered particles that strike the detector generate an electrical signal proportional to their energy, which is amplified and processed with rapid analogue and digital electronics. The data collected in the final stage has the form of a digitised spectrum [29]. The backscattering energy spectra of counts against channel number were obtained by collecting a charge of $8\mu c$, constituting a run.

RBS essentially relies on the following three physical concepts:

- the kinematic factor *K*,

- the energy loss of a particle ($\frac{dE}{dx}$), and
- the differential scattering cross-section ($\frac{d\sigma}{d\Omega}$).

3.4.1 Kinematic factor

When a beam of He^+ particles collides with a stationary target atom the incident particles may be scattered by the target atoms. Provided that the energy of the incident particles is considerably larger than the binding energy of atoms in the target, but also below the energy at which nuclear reactions will occur, the interaction can be treated as a simple elastic collision. Figure 3.13 illustrates a collision between an incident energetic particle with mass M_1, velocity υ_o, energy E_o and a target atom with mass M_2. During the collision, a transfer of energy from the moving particle to the stationary target atom occurs, leading to final velocities and energies υ_1, E_1 and υ_2, E_2 respectively.

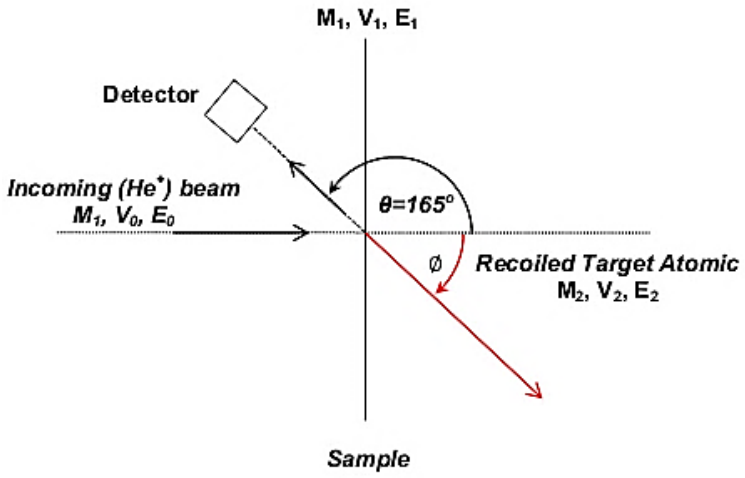

Figure 3.13: Schematic diagram showing the RBS experimental setup at the University of Pretoria [29].

The reduction in energy of the scattered incident particles depends on the masses of the incident and target atoms. The ratio of the projectile energies, E_o and E_l, are defined as kinematic factor *K*.

$$K = \frac{E_1}{E_o} \tag{3.1}$$

If the collision between the incident particle (He^+ particles) of mass M_1 and the stationary target particle of mass M_2, as shownin the equation below, is an elastic collision, it can be described. Based on this decription, the energy of the backscattered incident He^+ particle is given as [29]:

$$E_1 = KE_o = \left[\frac{M_1 cos\theta \pm (M_2{}^2 - M_1{}^2 sin^2\theta)^{1/2}}{M_1 + M_2}\right]^2 E_o \tag{3.2}$$

E_o and E_1 are respectively the incident and backscattered energies of the alpha particles. The energy ratio of the incident particle after and before collision is the kinematic factor *K*, and θ is the backscattering angle. Equation (3.2) must be adapted if the incident particle travels deeper into the substrate material. From the above equation it is clear that the energy of the backscattered He^+ particle E_1 can be calculated if the kinematic factor *K* is known. *K* can be calculated using M_1, M_2 and the scattering angle θ. At a fixed scattering angle, the kinematic factor *K* depends only on the mass ratio, namely M_1/M_2. The plus sign in equation (3.2) is only valid when $M_1 < M_2$, but when $M_1 > M_2$ there are two solutions, resulting in two kinematic factors *K* for backscattered He^+ particles at angle θ corresponding to different recoil angles [29]. Then incident He^+ particles of the same energy and incident angle will have varying backscattered energies when they bombard target particles that have different masses, which justifies the use of the use of Rutherford backscattering to identify the constituents of a sample. Equation (3.2) shows the dependence of the backscattered particle's energy on the target mass and the scattering angle θ. However, during measurement the kinematic factor *K* only depends

on the mass of the target atom M_2, since the detector angle θ and the mass of the projectile M_1 is constant. If the energy of the projectile E_o and its mass M_1 are known, one can determine M_2 (i.e. the mass of the atoms from which they are scattered), by measuring the energy E_1 of the backscattered particles. It is also evident from equation (3.2) that the energy of the particles scattered by the heaviest element is higher than those scattered by lighter ones. Furthermore, the energy E_1 of the projectile attains its maximum value when the scattering angle θ is 180º. The importance of the kinematic factor is that it describes the reduction of incident energy during the collision, and this then allows identification of the target atom's mass by measuring the scattered particle's energy.

3.4.2 Depth scaling of thin film systems

With regard to thin films deposited on the substrates, it is mainly the stoichiometry and depth profile of heavy elements within that are of primary interest here.

Figure 3.14 shows the scattering layout and the RBS spectrum of a thin compound film A_yB_{1-y} on a substrate *S*, where in many cases during semiconductor research, *A* is usually a heavy element, *B* is either *O* or *N*, and *S* is usually Si. The signals from elements *A* and *B* in the spectrum have high energy edges at K_AE_0 and K_BE_0 respectively, with the substrate signal *S* pushed back to lower energy by ΔE_s due to the ions losing energy within the thin film. The signal from *B* rests on top of the substrate signal *S*, due to $K_BE_0 < K_sE_0 - \Delta E_s$. Elemental depth profiling of the thin film is shown more clearly in the signal from *A*, which is isolated at higher energies.

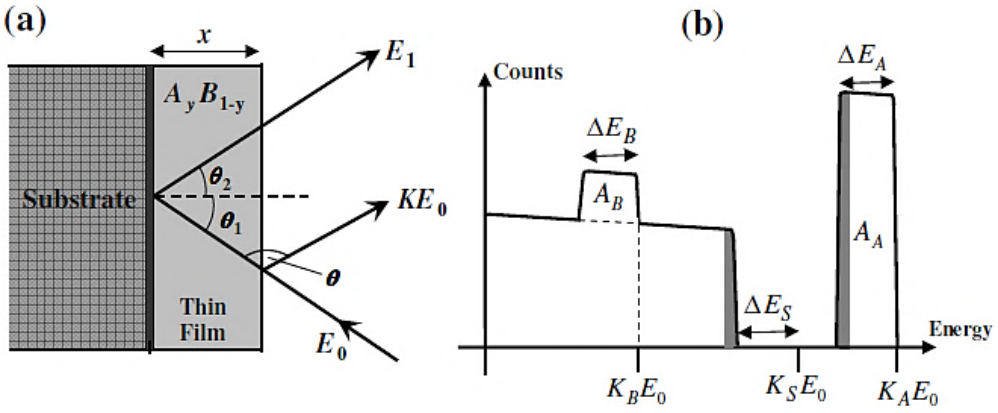

Figure 3.14: (a) Scattering geometry and (b) spectrum of an RBS measurement of a thin compound target [32].

Collisions with atoms of both *A* and *B* will now contribute to the energy loss process. Ions will lose the same amount of energy per unit length along the way in, but may lose a different amount along the way out, depending from which atom they backscatter, due to the difference in *K* values. The energy widths of the respective signals in the spectrum are [32]:

$$\Delta E_A = [S]_A^{AB} N^{AB} x \text{ and } \Delta E_B = [S]_B^{AB} N^{AB} x \tag{3.3}$$

with

$$[S]_A^{AB} = \frac{K_A}{\cos\theta_1} S_{IN}^{AB} + \frac{1}{\cos\theta_2} S_{OUT.A}^{AB} \tag{3.4}$$

$$[S]_B^{AB} = \frac{K_B}{\cos\theta_1} S_{IN}^{AB} + \frac{1}{\cos\theta_2} S_{OUT.B}^{AB} \tag{3.5}$$

and where $N^{AB}x$ is the areal density of the thin film, S_{IN}^{AB} is the stopping cross-section of the ions along the way in, while $S_{OUT.A}^{AB}$ and $S_{OUT.B}^{AB}$ are the cross-sections along the way out after backscattering from atoms of *A* and *B*, respectively. We assume that

Bragg's rule of additivity applies to the stopping cross-sections for both inward and outward paths at the same energy *E*, so that [32]:

$$S^{AB}(E) = [y]S_A(E) + [1-y]S_B(E) \tag{3.6}$$

The area of the signals in the spectrum from elements *A* and *B* are:

$$A_A = \frac{\Omega}{\cos\theta_1}\int_{E_0}^{E_x}\frac{\sigma_A(E)}{S_A(E)}dE \tag{3.7}$$

and

$$A_B = \frac{\Omega}{\cos\theta_1}\int_{E_0}^{E_x}\frac{\sigma_B(E)}{S_B(E)}dE \tag{3.8}$$

These can then be used to determine the stoichiometric ratio between the elements in the film. Depth profiles of elements *A* and *S* are shown in shaded regions in the spectrum.

3.4.3 Energy loss

When the alpha particle penetrates a target, it loses energy along its trajectory due to interaction between bound and free electrons, and to small-angle nuclear collisions, which is only of significance at low energies. The magnitude of energy lost depends on the total distance travelled by the incident particles, and on the density and composition of the target, as well as the incident particle's velocity [31]. The energy loss per unit length *dE*/*dx* at the energy *E* of the incident projectile is defined as:

$$\lim_{\Delta x\to 0}\frac{\Delta E}{\Delta x} \equiv \frac{dE}{dx}(E) \tag{3.9}$$

Depth scaling explains the relationship between the exit (from the substrate) energy E_1 of the alpha particle, backscattered at depth *x* inside the target substrate (see Figure 3.15)

and The energy of the incident alpha particle E_o. The energy E_o reduces to E just before the backscattering because the particle loses energy as it moves through the substrate. The backscattered particle at depth x loses more energy while exiting the target and eventually reduces to the exit energy E_1.

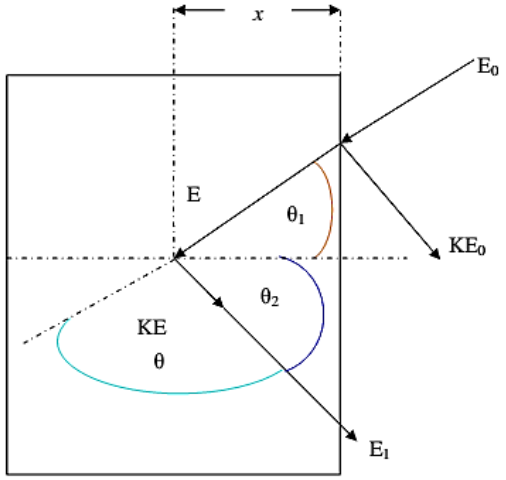

Figure 3.15: A schematic diagram showing the backscattering events in a target consisting of one element. The angles θ_1 and θ_2 are positive regardless of the side on which they lie with respect to the normal of the target [30].

The energy lost by the alpha particle upon entering the target particle is given as $E_o - E$, while the energy lost on its way out is given as $KE_o - E_1$. Assuming that the energy loss $(dE|dx)$ is constant over each path, the energy of the backscattered alpha particle at depth x is then given as [29, 33]:

$$KE_o - E_1 = \left[\frac{K}{cos\theta_1}\frac{dE}{dx}(in) + \frac{1}{cos\theta_2}\frac{dE}{dx}(out)\right]x \qquad (3.10)$$

The subscripts 'in' and 'out' refer to the constant values along the inward and outward paths. KE_o is the energy of the backscattered particles scattered from surface atoms of the target particle.

If ΔE is the energy difference between E_1 and KE_o, then:

$$\Delta E = KE_o - E_1 \tag{3.11}$$

The term $\frac{K}{cos\theta_1}\frac{dE}{dx}(in) + \frac{1}{cos\theta_2}\frac{dE}{dx}(out)$ in equation (3.10) above is the backscattering energy-loss factor $[S]$. It gives the relationship between the backscattered energy and the depth. Equation (3.10) can be rewritten as:

$$\Delta E = [S]x \tag{3.12}$$

3.4.4 Scattering cross-section

The scattering cross-section provides the relationship between the number of target atoms and detected particles. The number of particles that will be identified in a detector with solid angle Ω is determined by:

$$Y = \sigma(\theta)\Omega Q N_s \tag{3.13}$$

In such a case where $\sigma(\theta)$ is the scattering cross-section, a particle is backscattered towards a detector at an angle θ, Ns is the number of target atoms per cm^2 , and Q is the total number of incident particles [29, 31]. By considering the Coulomb repulsion of two nuclei (which is the case with RBS energy), the differential scattering cross-section can be calculated [29] with the Rutherford scattering cross-section in the laboratory frame of reference,

$$\frac{d\sigma}{d\Omega} = \left[\frac{Z_1 Z_2 e^2}{2E}\right]^2 \frac{\left[cos\theta + (1 - M_1/M_2\, sin^2\theta)^{1/2}\right]^2}{sin^4\,\theta\,(1 - M_1/M_2\, sin^2\theta)^{1/2}} \tag{3.14}$$

where Z_1 and Z_2 are the respective atomic numbers of the projectile particles of mass M_1 and target atoms of mass M_2. It is clear from equation (3.14) that the differential cross-section $\sigma(\theta)$ depends on Z_2^2, which indicates that RBS is significantly more sensitive to

high *Z* elements. Therefore, if equal amounts of a light and heavy element are present, the number of particles scattered from the heavy element will be much greater.

3.5 Scanning electron microscope (SEM)

The scanning electron microscope (SEM) is the most widely used system in the family of electron microscopes because it has unique features. It produces an electron beam which, upon hitting the sample, produces primary backscattered electrons, secondary electrons, X-rays and Auger electrons, as shown in Figure 3.16. The first SEM was constructed in 1942 and became available for commercial purposes since 1965 [34 - 36]. It uses magnetic lenses to direct a highly energetic beam of electrons towards the specimen [36]. Once the incident beam of electrons hits the surface of the specimen, the electrons rapidly lose speed. A strong interaction takes place on the surface of the specimen.

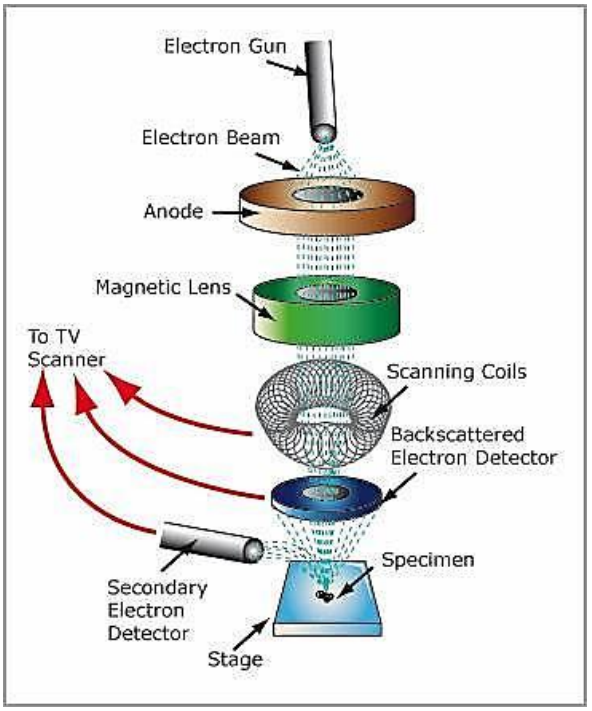

Figure 3.16: Schematic diagram of an external view of the SEM's fundamental components [37].

This interaction produces a variety of radiation signals from the surface of the specimen (see Figure 3.17), which scan across the entire surface. The radiations signals are collected by the detectors in the chamber and then displayed on the screen. The final image gives details about the sample's morphology, topography, crystallographic arrangement, and elemental composition [34-36]. The advantage of the SEM is that it provides a clear image, similar to a conventional photograph, and that it uses electromagnets, which allow the user of the system to adjust the desired level of magnification [34, 35].

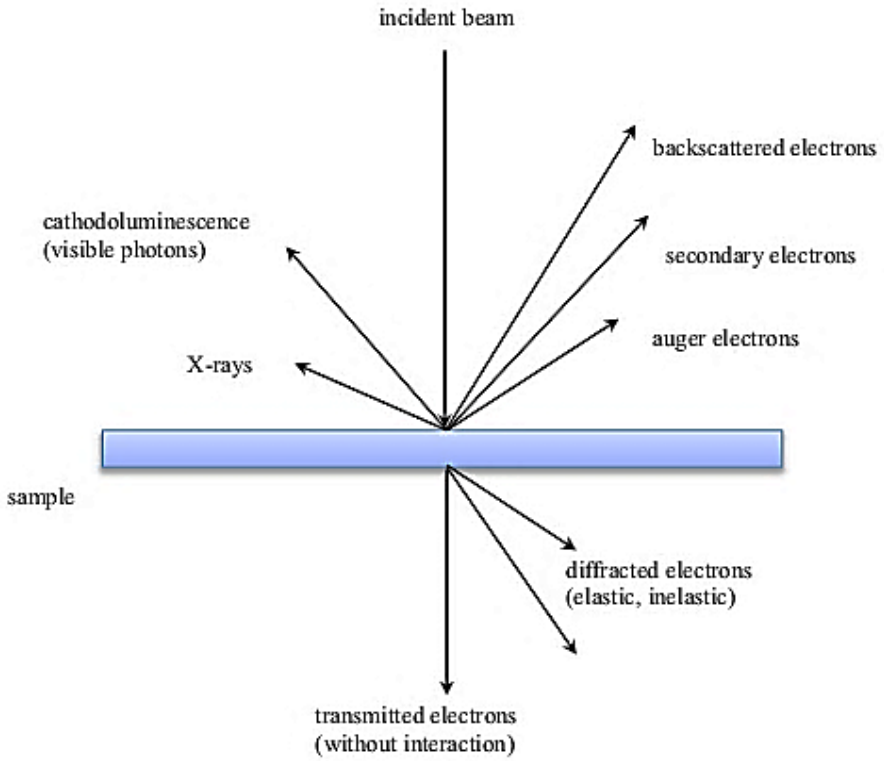

Figure 3.17: Schematic demonstration of the interaction of the incident electron beam with the sample and the radiation signals generated during interaction in SEM [34].

There is a variety of materials that can be used to produce electrons, the most common of which is a tungsten filament. The source material is heated up in order to release its electrons [34-36]. Once the electrons are extracted from the source material they are

directed towards the specimen by means of magnetic lenses and electromagnetic fields, which are on both sides of the column [34]. The speed of the extracted electrons is increased by placing a positive anode below the source material, and since the tungsten is a negative cathode, the force of attraction causes the acceleration of the electrons [36]. When electrons are extracted from the source, minimal ionisation energy is required. Tungsten, for example, requires 4.5 eV for electron release. The whole process must be conducted in vacuum [34].

The specifications of SEM are [35-37]:

- The electron beam scans over the entire surface of the specimen, bouncing back after having collided with the surface.
- No special preparation of the sample is required and a sample of any thickness can be used on the aluminium stub.
- The image is displayed on a computer monitor.
- The sample is placed in the chamber at a level below the column.
- It provides a two-dimensional image projection of the specimen.

3.5.1 SEM Experimental Setup

In this study, a Zeiss Ultra 55 field SEM was used for surface topography and morphology analysis of the Co thin film co-deposited on FeZr/Si (see Figure 3.18). This machine employs a field emission electron gun (FEG); therefore, emphasis would be laid on the FEG. An FEG consists of a wire (usually tungsten) with a sharp tip and a radius of less than 100 nm. When the field at the tip reaches a magnitude of about 10V/nm, electrons are emitted. A cathode current density of about 10^5 A/cm^2 may be obtained from a field emitter in comparison with 3 A/cm^2 from a thermionic source [30]. The Zeiss Ultra 55 is equipped with SE secondary electron (SE) detectors, backscattered

electron (BE) detectors, and an in-lens SE detector. The latter detector is highly surface-sensitive; its efficiency improves as the acceleration voltage drops lower. For this study, the in-lens SE detector was used to examine the surface of the thin film before and after annealing [38]. The results are discussed in Chapter 4.

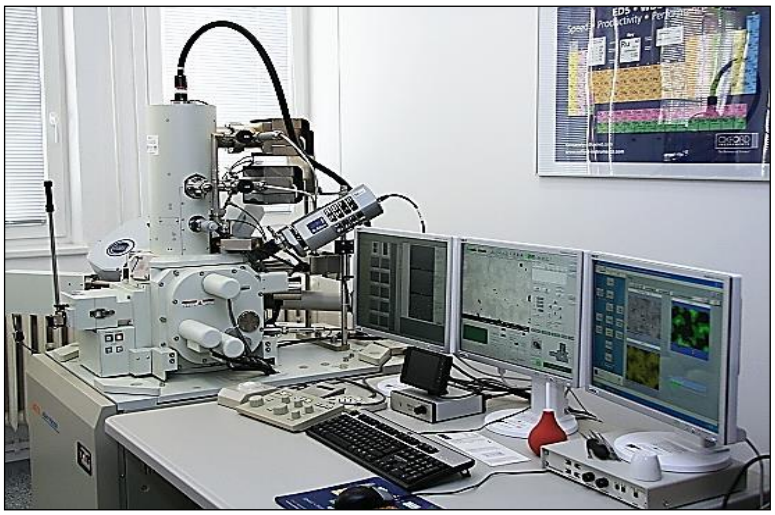

Figure 3.18: The scanning electron microscope at the University of Pretoria.

3.5.2 Fracture cross-section

Cross-section preparation is a very powerful way of examining how a material, laminate or component, is assembled and manufactured; determining how different layers interact; or searching for the mechanisms causing a failure. In all of these cases it is vital that any cross-section preparation does not disturb, smear or alter the sample, otherwise it could lead to false analysis and conclusions. The technique selected to generate the section is, therefore, vital, as is the skill and experience of the individual preparing the sample, particularly when samples are scarce.

In this study, the cross-sectional SEM samples were prepared by a fracture technique. The sample was rested on a pin lying on a brass block. The sample, pin and block were

submerged in LN_2 until the boiling stopped. Then one side of the sample was kept in contact with the block while pressure was applied at the free end, causing the sample to fracture at the location of the pin.

3.6 X-ray diffraction (XRD)

The XRD is a widely used technique employed to study the crystalline structure of materials based on the ability of atoms to scatter X-rays. The principle of XRD is that a collimated beam of X-rays impinges on the sample and the intensity of the diffracted beam is measured. This occurs only when certain geometrical conditions are satisfied, which may be expressed by Bragg's law,

$$n\lambda = 2d\sin\theta \tag{3.15}$$

where d is the spacing between planes in the atomic lattice of the sample generating the diffraction, n is an integer, λ is the wavelength of the X-rays, and θ is the incidence angle in degrees. From this equation, constructive interference will occur at a scattering angle of θ for a given interplanar distance and X-ray energy. By varying the incident angle θ and recording the positions of constructive interference, it is possible to measure the d-spacing of the crystal planes. A plot of X-ray counts versus 2θ gives a series of peaks, and the position of each peak defines the spacing between a set of planes. The intensity of the peak is determined by the interference of the X-rays reflecting off the other sets of planes in the crystal [31].

As seen in Figure 3.19, the diffraction from a set of planes will only occur if the normal to these planes bisects the angle between the incident and the scattered beam. It allows the identification of the phases (but provides no depth information) in a thin film because it determines the interplanar distance d_{hkl} (the latter is characteristic for a silicide). The Co-K_{alpha} X-rays (wavelength 1.789 Å) were used together with a linear detector.

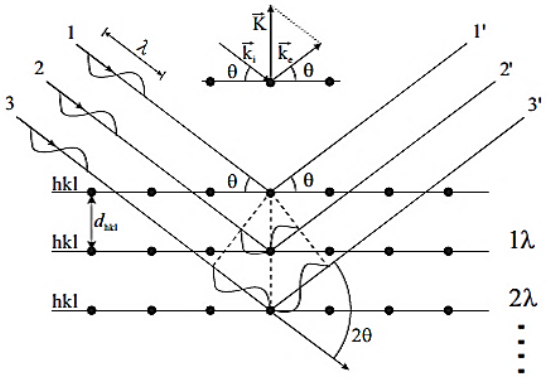

Figure 3.19: Illustration of Bragg's law for an incident X-ray beam impinging on a crystalline substrate [38].

XRD is a quick and efficient technique for phase identification in thin films, and is most suited to films thicker than a few tenths of nanometers (nm). To limit the penetration of the beam and enhance the diffraction pattern of the film with respect to the substrate, glancing angle geometries are used. Individual crystalline phases are identified by the characteristic diffraction patterns. Such X-ray patterns also reveal information on the orientation and size distribution of crystallites. X-ray techniques provide superior angular resolution and more accurate structural data than available from electron diffraction, and does so over a large volume area of the sample. The XRD setup is shown in Figure 3.20 (a).

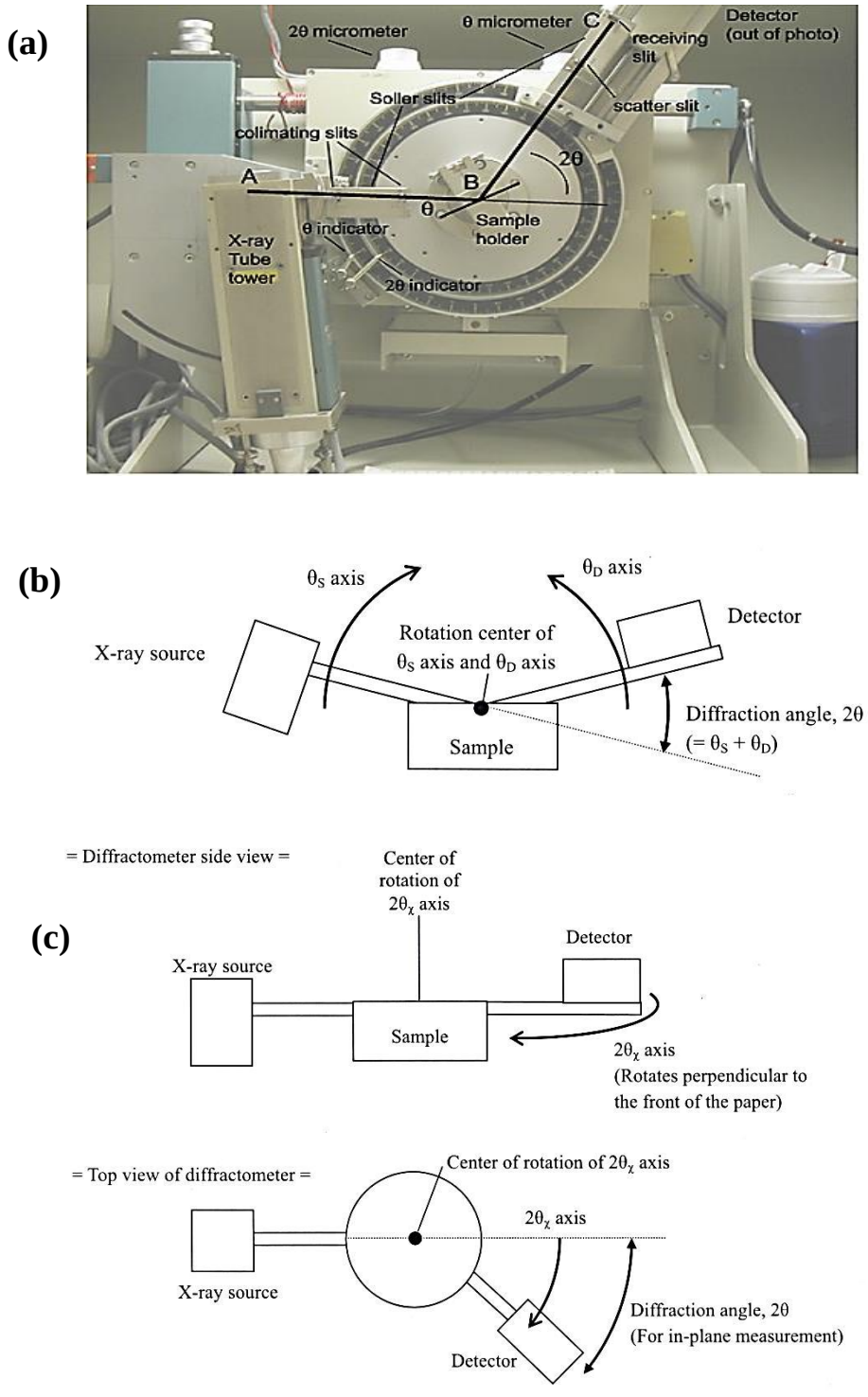

Figure 3.20: (a) XRD setup (b) XRD setup Goniometer axes in horizontal sample mount XRD (c) In-plane axis (optional)[38].

A horizontal sample mount X-ray diffractometer has the following two goniometer axes [38]:

- θs axis: The axis for setting the angle of the X-ray source with respect to the sample surface. (The "*S*" in "θs" refers to "source.").

- θ_D axis: The axis for setting the angle of the detector with respect to the sample surface. (The "*D*" in "θ_D" refers to "detector.")

- The θs axis and the θ_D axis are used to set 2θ, the diffraction angle.

The optional in-plane arm has a $2\theta_x$ axis, which rotates the detector in a plane parallel to the sample surface, shown in Figure 3.20 (c). In in-plane measurements, which perform measurements in the range close to $\theta_S = 0°$ and $\theta_D = 0°$, the diffraction angle $2\theta_x$ can be assumed to take the same value as the $2\theta_x$ axis. If the measurement range is not close to $\theta_S = 0°$ and $\theta_D = 0°$, as in pole figure measurements or reciprocal space mapping measurements (also known as mesh measurement), diffraction angle 2θ differs from $2\theta_x$ and assumes a value based on angles, θ_S, θ_D, and $2\theta_x$ [38].

3.6.1 XRD Experimental Setup

The XRD analysis was performed at the University of Pretoria. Bragg-Brentano scattering geometry XRD analysis was done using a Bruker-AXS diffractometer, D8 Advanced XRD system with a Co(Kα1) X-ray radiation source, at two-theta step size of 0.05° and dwell time of 2*s* per frame. For an analysis, the X-ray incident beam was kept at an angle of 5° relative to the surface of the sample, and the diffraction pattern was collected by a detector rotated by a goniometer from 20° to 90°. Bragg-Brentano or wide-angle XRD analysis was also performed on the annealed samples. The radiation source angle (θ) was maintained at 20° and the detector angle scanned from 30° to 70°.

The XRD diffraction data was converted to two theta positions corresponding to the wavelength of cobalt kα radiation (λ = 1.789 Å). This was done to enable comparison of the results of this study with the standard diffraction files from the International Centre for Diffraction Data files (ICDD-PDF-2) for indexing purposes.

3.7 Auger electron spectroscopy (AES)

Auger electron spectroscopy (AES) is the principal technique used to determine the concentration of elements on a surface [39]. It is an element-sensitive technique and can, unlike RBS, distinguish between Co, Fe and Zr atoms. It is based on the ionisation of atoms by high-energy electron radiation and the subsequent emission of Auger electrons. The technique can be used to determine the relative amount of the elements present in the thin film under investigation. It is also surface sensitive. Only information from the top 10-100 Å of the film is accessible. Therefore, layers of the film have to be removed, followed by new AES measurements to obtain depth information on the (relative) atomic concentration of the elements in the film. This procedure is applied in AES sputter experiments, where Ar^+ sputtering is used to remove the topmost layers of the specimen.

AES is a surface analysis technique that ascertains the chemical composition in the near surface area of a specimen. In combination with ion sputtering, AES can be used to obtain a depth profile of the atomic ratio of the entire thickness of a thin film or bulk specimen. Many publications on surface analysis also discuss AES, for example references [40, 42]. For a book-length study completely dedicated to Auger and X-ray photoelectron spectroscopy, one can refer to references [43, 44].

In AES, the atoms in the specimen are ionised by irradiation of the sample with high-energy electrons, typically by means of a 6 keV electron beam, with beam currents of the order of 100 nA. This irradiation results in the ejection of electrons from the low-energy electron shells (*K*, *L*, *M*,...) in the atom, as shown in Figure 3.21.

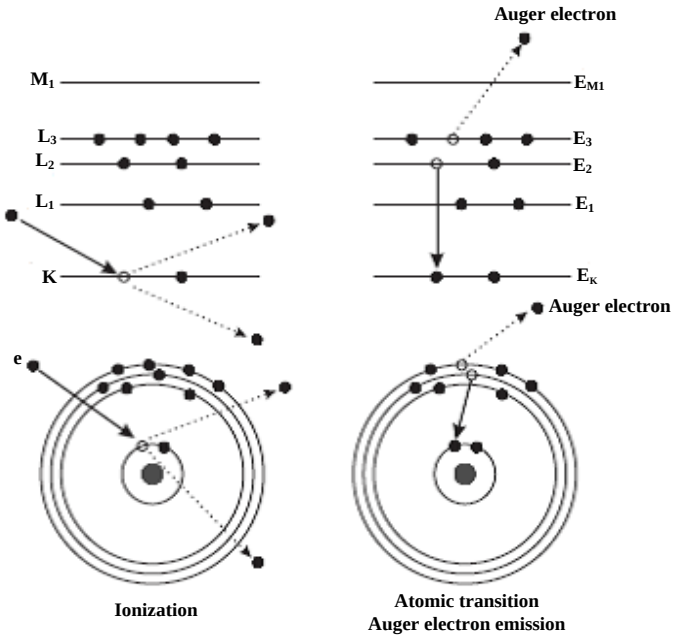

Figure 3.21: The Auger process. The ionization, atomic transition and Auger electron emission processes are shown schematically in (a) an atomic energy level model and in (b) an atomic shell model [42].

The vacancy in the atom's electron shells is then filled by an electron from a shell with a lower binding energy. The energy gained in this process is transferred to another electron that is subsequently emitted from the atom (Figure 3.21). After leaving the atom, this Auger electron has energy E_{KL2L3}, given in equation (3.16). This equation neglects contributions from the interaction energy between the vacancy in the L_2 and L_3 levels, as well as intra-atomic and extra-atomic relaxation [44]:

$$E_{KL_2L_3} \approx E_K - E_2 - E_3 \qquad (3.16)$$

where E_K corresponds to the binding energy of an electron in the *K*-shell of the atom. The nomenclature for the atomic electron shell is reflected in the names given to Auger electrons. For example, a Co_{KL2L3}-Auger electron is an electron emitted from the L_3-shell of a Co atom after an L_2-electron has filled a vacancy in the *K*-shell.

The energy of Auger electrons is characteristic for the element. Consequently, Auger electron spectroscopy is an element-sensitive technique. Only Auger electrons from the atoms in the near-surface region of the specimen will appear in the Auger peaks. Electrons emitted from within the sample, further from the sample surface than the electron mean free path, lose energy before they leave the sample and will not be counted in the Auger peak, hence the surface sensitivity of the technique.

3.7.1 Quantitative analysis

To extract quantitative information from AES spectra, one has to relate the (background-subtracted) intensity of an AES peak to the atomic density of the electron-emitting atom in the compound. A comprehensive exploration of the large number of factors that influence the intensity of an Auger peak can be found in reference [44]. These parameters include, for example, the fluorescence yield, ionisation cross-section, atomic density, and inelastic mean free path.

For practical use, one defines a matrix factor F_{Am} for element *A*, that contains most of the matrix-related parameters. The atomic concentration X_A of element *A* in matrix *m* is then given by [44]:

$$X_A = \frac{F_{Am}\left(\frac{I_{Am}}{I_A^{\infty}}\right)}{\sum_i F_{im}\left(\frac{I_{im}}{I_i^{\infty}}\right)} \qquad (3.17)$$

where I_{Am} is the intensity of the selected AES peak for element *A* in matrix *m*. The sum in the denominator is taken over all elements in the matrix. I_A^{∞} is the sensitivity factor, which is related to the intensity of the Auger peak when a matrix of single element *A* is analysed. This factor implicitly contains all experimental and theoretical parameters that are not included in the matrix factor.

For quantitative Auger analysis, one defines a weak matrix factor, which does not depend on the atomic density of the element in the matrix, and an average matrix relative sensitivity factor (AMRF) I_{Am}^{av}. For most Auger electrons and matrices, the weak matrix factors in equation (3.17) cancel out, and the atomic fraction X_A of element *A* in a random matrix *m* is obtained from:

$$X_A = \frac{\frac{I_{Am}}{I_A^{av}}}{\sum_i \frac{I_{im}}{I_i^{av}}} \tag{3.18}$$

Two approaches can be followed from this point forward. One can calculate the AMRF theoretically or determine I_{Am}^{av} experimentally. The experimentally-determined sensitivity factors will implicitly contain a matrix effect. Therefore, one should keep in mind that the sensitivity factors might be slightly different for separate matrices or silicide phases. In this study, cobalt silicide thin films were utilised to determine the sensitivity factors for those elements relative to Si. This comparison with Si Auger peaks reduces the errors on the determined atomic concentrations due to different experimental conditions, since both the Si and metal Auger peaks are measured in the same experiment. The exact method applied to obtain reliable sensitivity factors is explained in reference [45].

In equation (3.8) the atomic fraction of an element is determined from the ratio of peak intensities. Therefore, any measurement that is proportional to the full Auger peak intensity for a certain element can be used for the analysis. Examples of these are the area under an AES peak and the peak-to-peak height of a broadened differential of the direct Auger spectrum. In this work, the derivative approach for the quantitative Auger analysis was used. An example of a differential AES spectrum is shown in Figure 3.22. Reference [45] contains more details on the choice of this type of analysis over the integration of the area under an AES peak.

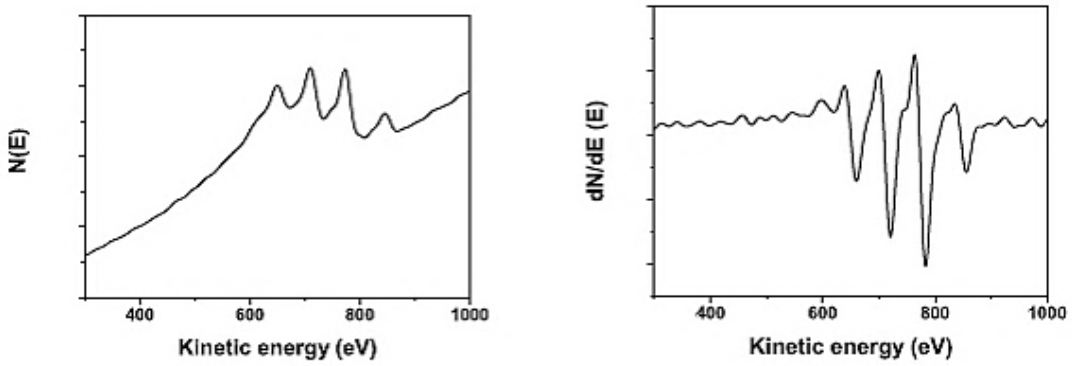

Figure 3.22: AES and differential ASE spectra from two metal alloys [42].

In view of the fact that AES is a surface-sensitive technique, the only way to get in-depth information on the atomic concentrations in a thin film is by removing the topmost layers of the film (with ion sputtering) and performing another AES measurement. This procedure is repeated in order to measure Auger depth profile. From the quantitative analysis of each of these AES spectra, an AES depth profile can be constructed. Such a depth profile is shown in Figure 3.23. For a constant sputter rate, the linear timescale in the x-axis corresponds to a depth from the sample surface. The y-axis represents the normalised atomic ratio between all the elements that are taken into account in the analysis. This value can be regarded as the atomic concentration of a specific element in the film, if there are no other elements in that film than the ones that are analysed.

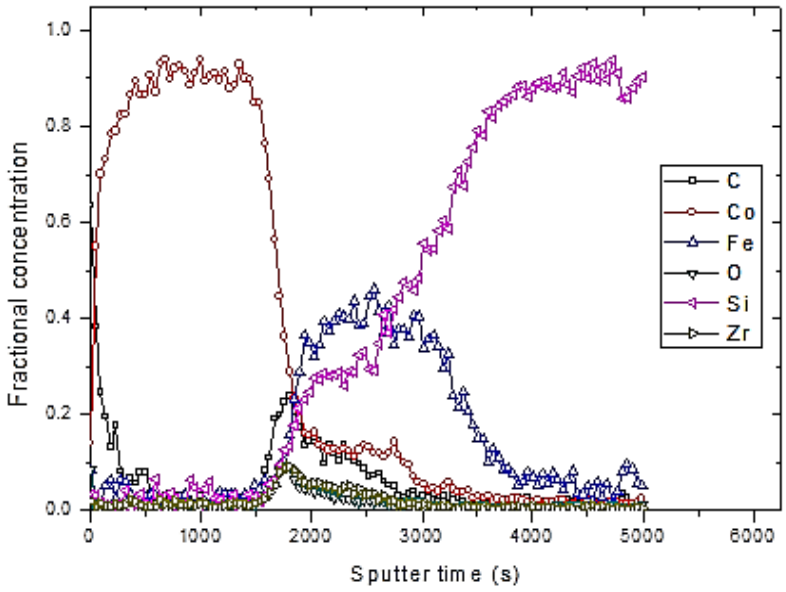

Figure 3.23: A typical AES depth profile of Si/FeZr/Co sample after annealing.

In these experiments, a PHI 600 spectroscope was used with electron beam energy of 10 KeV and 2.6 μA current with dual gun Ar^+ ion sputtering for concentration depth profile analysis in order to obtain information on the solid-state reactions. The peak-to-peak heights were converted to concentrations without the use of specific standards.

References

[1] A. V. Tkachuk and A. Mar, "Electron-poor Sr Au_x In_{4-x} ($0.5 \leqslant x \leqslant 1.2$) and Sr Au_x Sn_{4-x} ($1.3 \leqslant x \leqslant 2.2$) phases with the $BaAl_4$-type structure", *Journal of Solid State Chemistry, 180(8), (2007) 2298-2304.*

[2] Z. Altounian, T. Guo hua and J. O. Strom Olsen, "Crystallization andcharacteristics of Cu-Zr metallic glasses from $Cu_{70}Zr_{30}$ to $Cu_{25}Zr_{75}$", *Journal of Applied Physics, 53(7), (1982) 4755- 4760.*

[3] M. J. Brahamcha. "Crystallization study on CuZr alloys with fixed stoichiometry and different microstructures (amorphous or nanocrystal line)." *(2013).*

[4] R. Reuschling,"Konzepte und KomponentenfürVakuum-Beschichtung sanlagen", *Special, Wiley-vch Verlag Gmbh & Co Kga A, D-Weinheim, (2004).*

[5] O. Milton, "Material Science of Thin Films (Deposition and Structure)", *Academic Press; London, (2002).*

[6] T. Raimond, S. Puckett and T. J. Webster. "Greater osteoblast and endothelial cell adhesion on nanostructured polyethylene and titanium", *International journal of Nano medicine 5, (2010) 647.*

[7] Y. Wang and M. Nastasi, "Handbook of Modern Ion Beam Materials Analysis", *Aooendices, (2009).*

[8] D. M. Mattox, "*Handbook of Physical Vapor Deposition (PVD) Processing: Film Formation, Adhesion, Surface Preparation and Contamination Control", Westwood: Noyes Publications, (1998) 365.*

[9] M. Becht, F. Atamny, A. Baiker, and K.-H. Dahmen, "Morphology analysis of nickel thin films grown by MOCVD", *Surface Science, 371, (1997) 399–408.*

[10] K. L. Chopra and I. Kaur, "Thin Film Phenomena", *New York: McGraw-Hill, (1969).*

[11] J. A. Thornton and J. E. Greene, "Sputter Deposition Processes", in *Handbook of Deposition Technologies and Applications*, 2*nd ed., R. F. Bunshah, Ed. Park Ridge: Noyes Publications, (1994) 275–345.*

[12] S. Rossnagel, "Sputtering and Sputter Deposition", in *Handbook of Thin Film Deposition Processes and Techniques*, 2nd ed., K. Seshan, Ed. *Norwich, NY: Noyes Publications, (2002) 319–348.*

[13] E. G. Njoroge, Solid-state interactions between Zr thin films and SiC, *University of Pretoria, (2014).*

[14] A. Y. Cho and J. R. Arthur, "Molecular beam epitaxy". *Progress in Solid State Chemistry, 10, (1975) 157-191.*

[15] A. Y Cho, "Molecular Beam Epitaxy", *Am. Inst. Physics, New York (1994).*

[16] J. R. Arthur, "Molecular beam epitaxy." *Surface Science 500, no. 1 (2002) 189-217.*

[17] H. Geiger and E. Marsden, "On a diffuse reflection of a particles", *Royal Society 82, (1909) 495-500.*

[18] E. Rutherford," The scattering of alpha and beta particles by matter and the structure of the atom", *Philosophical Magazine 21, (1911) 669-688.*

[19] W. K. Chu, J. W. Mayer, M. A. Nicolet, T. M. Buck, G. Amsel, and F. Eisen, "Principles and applications of ion beam techniques for the analysis of solids and thin films," *Thin Solid Films, vol. 17, (1973)1–41.*

[20] J. F. Ziegler, "Material analysis by nuclear backscattering", *Prenum press, New York, (1975).*

[21] K. Kusao, M. Satoh, and K. Morita, "An Area Ratio Method for RBS Compositional Analysis of Thin films," *Surface and Interface Analysis, vol. 18, (1992) 417–420.*

[22] H. Matzke, "Application of Ion Beam Techniques to Solid State Physics and Technology of Nuclear Materials," *Journal of Nuclear Materials, vol. 136, (1985)143-153.*

[23] L. G. Earwaker, "Rutherford backscattering and nuclear reaction analysis," *Vacuum, vol. 45, (1994) 783–803.*

[24] C. Jeynes, Z. H. Jafri, R. P. Webb, A. C. Kimber, and M. J. Ashwin, "Accurate RBS Measurements of the Indium Content of InGaAs Thin Films," *Surface and Interface Analysis, vol. 25, (1997) 254–260.*

[25] P. Aloupogiannis, A. Travlos, X. Aslanoglou, M. Pilakouta, and G. Weber, "Rare-earth silicide thin film study. Comparison of heavy ion and conventional RBS," *Vacuum, vol. 44, (1993) 37–39.*

[26] A. Climent-Font, M. T. Fernandez-Jimenez, U. Watjen, and J. Perriere, "RBS: An analytical technique for elemental characterization of standards; advantages and limits of application," *Nuclear Instruments and Methods in Physics Research A, vol. 353, (1994) 575–578.*

[27] L. Palmetshofer, "Surface and Thin Film Analysis," in Surface and Thin-film Analysis, H. Bubert and G. Friedbacher, Eds. *Weinheim: Wiley Online Library, (2011) 191–202.*

[28] B. Brijs, J. Deleu, C. Huyghebaert, S. Nauwelaerts, K. Nakajima, K. Kimura, and W. Vander vorst, "Advanced RBS Analysis of Thin Films in Micro-Electronics", *in Application of Accelerators in Research and Industry - Sixteenth International Conference, 3, (2001) 470–475.*

[29] W. K. Chu, J. W. Mayer and M. A. Nicolet, "Backscattering spectrometry", *Academic Press, New York, (1978).*

[30] T. T. Hlatshwayo, "Diffusion of Silver in 6H-SiC" PhD diss., *University of Pretoria, (2010).*

[31] L. C. Feldman and L. W Mayer, "Fundamentals of surface and thin film analysis, *North Holland, New York, (1986).*

[32] C. T. Kuei, "High depth resolution Rutherford backscattering Spectrometry with Magnet spectrometer: Implementation and Application to Thin Film", *National University of Singapore, (2009).*

[33] J. R. Tesmer, M. A. Nastasi, J. C. Barbour, C. J. Maggiore, J. W. Mayer, "Handbook of Modern Ion Beam Materials Analysis", *Materials Research Society, Pittsburgh, PA, (1995).*

[34] E. J. Mittemeijer , "Fundamentals of Materials Science: The Microstructure–Property Relationship Using Metals as Model Systems", *Chap. 9: Phase Transformations." (2010) 424-458.*

[35] A. Vilalta-Clemente and K. Gloystein, "Principles of Atomic Force Microscopy AFM", *Physics of Advanced Materials Winter School, (2008).*

[36] P. J. Goodhew, J. Humphreys and R. Beanland, "Electron Microscopy and Analyses", *Taylor and Francis Group, (2001) 122-166.*

[37] J. Goldstein, D. Newbury, D. Joy, C.Lyman, P.Echlin, E. Lifshin, L.Sawyerr and J. Michael, "scanning electron microscope and X-Ray microanalysis", *3rd edition, Springer, USA (2003).*

[38] C. Rigku, "X-ray diffraction analysis for thim film samples", *Training Textbook, 1st Edition", July (2009).*

[39] R. Pretorious, C. L. Ramiller, S. S. Lau, and M. A. Nicolet, "Radioactive silicon as a marker in thin-film silicide formation", *Apply Phys., Lett. 30, (1977) 501-503.*

[40] C. L. Feldman and J. W. Mayer, 'Fundamentals of surface and thin film analysis", *North-Holland, New York, (1986).*

[41] J. M. Walls and W. A. Grant, "Methods of surface analysis", *Cambridge university Press, Cambridge, (1990).*

[42] D. Smeets, Nucleation diffusion and texture during growth of coni-silicides. *Ph.D. Thesis, KU Leuven, Belgium, (2007).*

[43] D. Briggs and M. P. Seah, "Practical surface analysis", *Volume 1, Auger and X-ray photoelectron spectroscopy, John Wiley & Sons, Frankfurt am Main, 1994.*

[44] D. Briggs and J. T. Grant, "Surface analysis by Auger and X-ray photo-electron spectroscopy", *IM Publications, Chichester, (2003).*

[45] L. Rik, "Nucleatie en groeikinetica van dunne CoNi-silicidelagen op Si(100)", *Licentiaatsthesis,KULeuven, (2006).*

CHAPTER 4

RESULTS AND ANALYSIS

4.1 Introduction

The initial idea for this project was to configure a diffusion barrier layer by mixing two suitable metals that would form a well-mixed barrier layer. The first two attempts to make a suitable sample were unsuccessful–the first aimed to fabricate a CrZr barrier layer by arc melting, and the second sought to prepare FeZr as a barrier layer through solid-state diffusion. The results for both experiments are briefly discussed below. On the third attempt, FeZr was again prepared, but with a different method, namely co-evaporation (MBE), and the diffusion barrier layer that was to be placed between the Co and Si-substrates was successfully created.

4.2 Si/CrZr/Si system by arc melting

The first attempt was a pre-mixed (Zr + Cr) barrier layer made by alloying Zr and Cr using an Arc Melter MAM-1 and deposited $Cr_{15}Zr_{85}$ on Si by an E-beam evaporation system. But this was not successful because an alloy comprising a mixture of $Cr_{15}Zr_{85}$ was not produced. This was due to the fact that the evaporation temperature of Cr is less than that of Zr, thus only Cr was evaporated. This has, however, already been the subject of detailed discussion in this study. Since a CrZr alloy was not produced, another approach for fabricating an alloy composed of two metals that would serve as a diffusion barrier between the Co and Si-substrates had to be found.

4.3 Si/FeZr/Co system by solid-state diffusion

It was clear that pre-mixing would not work, and so, in a second attempt, Fe and Zr were deposited using the DC sputtering technique of metals onto a single-crystalline Si-substrate. Seven layers of Zr and Fe were deposited sequentially on the silicon substrate.

The thin layers of Zr were 10 nm thick, followed by a thicker Fe layer of 46 nm. These thicknesses were chosen to create an overall composition percentage. After deposition, solid-state diffusion was used to attempt fabrication of an FeZr alloy. The samples were annealed at low temperature ranging between 350 to 450 °C for as long as 1-14 days. The temperature was deliberately not raised to avoid any interaction between Zr or Fe with Si. All the RBS spectra of samples annealed between 350 and 450 °C were found to perfectly overlay with the unannealed samples; hence, they are not reported here as there was no visible reaction, even after annealing for 14 days. And when the samples were annealed at high temperatures between 550 and 750 °C, it was very difficult to avoid the interaction between Zr and Fe with the Si-substrate. All the RBS spectra of samples annealed between 550 and 750 °C showed the afore-mentioned interaction. This was an undesired occurrence, rendering the attempt unsuccessful as it was not possible to fabricate an FeZr alloy.

Therefore, this procedure was discarded in search of another in light of the fact that there was too much O_2 in the Zr, which was problematic, and an FeZr alloy was not deposited on the Si-substrate after annealing.

4.4 Si/FeZr/Co system by MBE

After two unsuccessful attempts, another method to create an alloy for use as a diffusion barrier layer was sought. FeZr was retained as the combination of choice for use in yet another technique, namely co-evaporation MBE.

4.4.1 Introduction

The solid-state interactions between Co and Si through different thicknesses of FeZr diffusion barrier layers, annealed in vacuum and at different annealing temperatures, are presented and discussed in this chapter. The purpose of using multi-step annealing of 400 and 450 °C in this study is to improve the growth of cobalt silicides. All the prepared samples were analysed by RBS before and after annealing. The surface and interface

morphology of the samples was investigated by SEM. The thin-film structure and phases formed were identified by X-ray diffraction and these results are examined further on.

In order to discuss the cobalt-silicide phase formation, one has to begin by considering the cobalt-silicon EHF and phase diagram, as shown in Figure 2.6. On the Co-Si phase diagram, there are three congruent compound phases, specifically CoSi, Co_2Si and $CoSi_2$. The EHF model states that the first phase to form will be the one that has the most negative heat of formation ($\Delta H'$) at the concentration of the liquidus minimum. It can be seen from the EHF diagram in Figure 2.6 that at the concentration of the liquidus minimum the formation of Co_2Si will lead to the biggest free energy change. It follows that Co_2Si will normally be the first phase to form at a temperature of about 350 °C, followed by CoSi formation at about 375 °C, and then $CoSi_2$ forms at about 550 °C [1, 2].

By using concentration-ontrolled phase selection (CCPS) [3], it is possible to control or influence phase formation so that only phases with suitable physical and electrical properties are formed. A Ti diffusion barrier has been used in the presence of different ambient atmospheres and different capping layers to successfully form uniform, epitaxial $CoSi_2$ directly as first phase [4-7] instead of Co_2Si, which is usually found as first phase. In this study of cobalt-silicide formation, all depositions and annealing were peformed successfully. Two different metals were used for a diffusion barrier layer of varying thicknesses to determine the possible successful application of concentration-controlled phase selection. The aim was to attempt to form CoSi or $CoSi_2$ as first phase, instead of the normal Co_2Si by controlling the Co concentration at the growth interface.

4.4.2 Unannealed sample

4.4.2.1 RBS results

The RBS technique has been used in this study to investigate the reaction between Co and Si through FeZr as diffusion barrier layer. All the samples prepared in this study were analysed by RBS before and after annealing. RBS analysis was performed to obtain the elemental composition of the unannealed and annealed samples, the thickness of deposited Co film and the thickness of the reaction area. The RBS spectrum of the unannealed sample is shown in Figure 4.1, along with the simulated spectra done using the Rutherford Universal Manipulation Program (RUMP) computer code [8]. RBS analysis using RUMP found the Co layer to be 1130×10^{15} at/cm^2 thick. Assuming an atomic density of 9.00×10^{22} at/cm^3, this yields a thickness of 126 nm. This is of course a lower bound on the Co thickness, as the actual density of the layer may be less than the standard density. The vertical axis is the normalised yield; that is, the number of particles scattered into the detector and normalised to the total incident beam dosage, the detector solid angle, and the channel width of the multichannel analyser [9]. This normalisation procedure allows direct comparison of spectra from the different samples. The energy of the backscattered particles and channel numbers are plotted on the horizontal axis of this graph. The arrows in the graph shown in Figure 4.1 indicate the surface positions of Si and Co. The peak observed at about 1.15 MeV is from the enriched Zr part of the FeZr layer and is superimposed on the Co-signal. The corresponding Fe signal is visible between channels 300-340. The narrowness of the Zr peak is due to the overgrowth of a thin Zr layer. Due to the asymmetric e-gun geometry, the rest of the Zr peak overlaps with Co, up to an energy of 1.08 MeV. The FeZr was found to be 490×10^{15} at/cm^2 thick. Assuming that the density of $Fe_{90}Zr_{10}$ can be estimated from the elemental densities, this equals 63 nm.

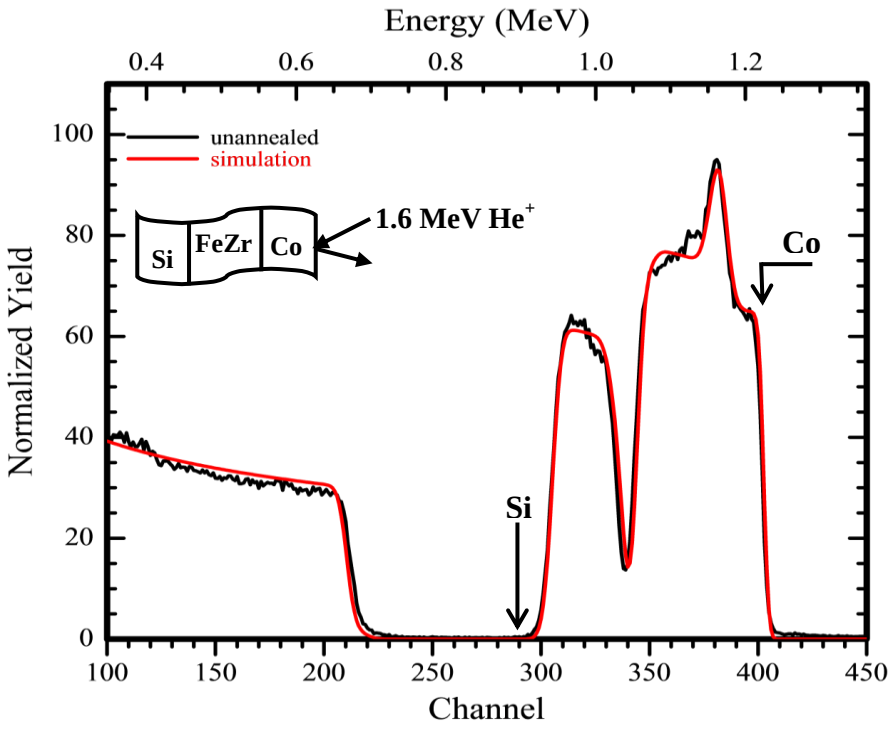

Figure 4.1: Raw RBS spectrum of unannealed Si<100>/FeZr(63 nm)/Co(126 nm) sample with RUMP simulation spectrum.

4.4.2.2 SEM results

The micro-structure and nano-structure of the Co/FeZr/Si sample surface and cross-section were analysed by SEM. Surface morphology analysis of the samples was performed on the unannealed and annealed samples.

The surface topography can affect the RBS spectra, especially where broadening of the peaks is of interest. The topography of the sample was investigated using the scanning electron microscope. Surface changes, as a result of annealing the samples, were investigated and monitored using the SEM in-lens mode.

The SEM results depicted in Figure 4.2 (a) show that the unannealed sample is fairly smooth and possesses a homogenous structure. The uniform deposition can be observed from the low magnification image and the granular Co surface in the high magnification

one. The deposition of a Co/FeZr thin film onto the Si surface resulted in a uniform granular surface. At low magnification, the surface is uniform, smooth and nearly featureless. But at higher magnification, the granular surface features are clearly visible, as seen in Figure 4.2 (b).

It can be observed from these plane view SEM images that the granules on the unannealed sample are uniformly distributed and have nearly the same size. The granules are closely packed and the Si substrate is fully covered by the Co/FeZr thin film. There is a clear absence of pores and other surface defects in the film.

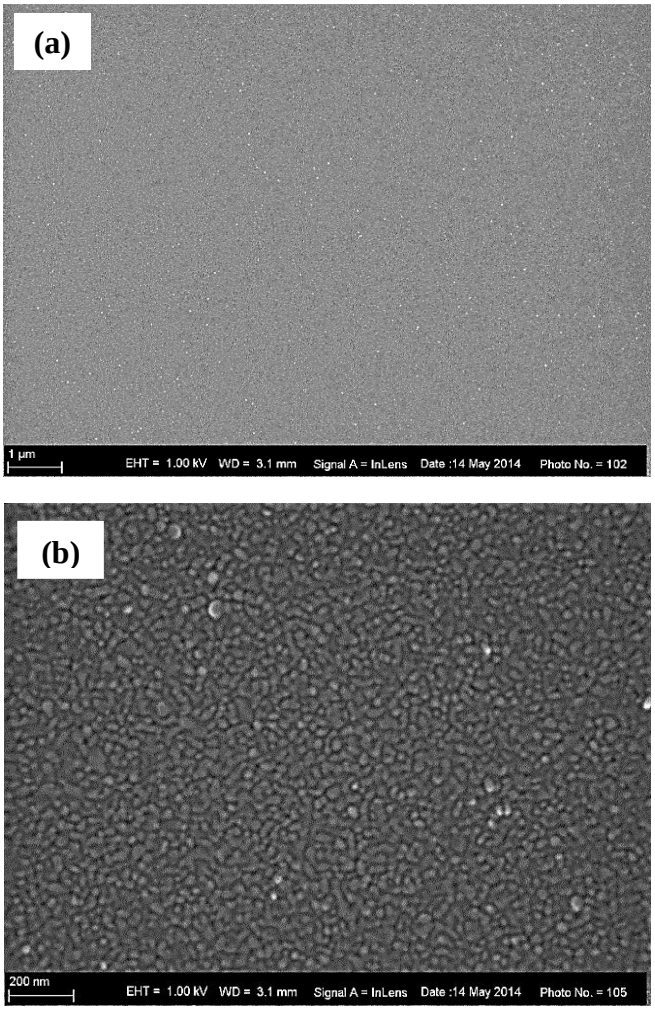

Figure 4.2: SEM micrographs of Si<100>/FeZr(63 nm)/Co(126 nm) unannealed sample: (a) low magnification and (b) high magnification.

4.5 Annealed Si<100>/FeZr(33 nm)/Co(126 nm) sample

4.5.1 RBS results

In the subsequent analysis, the unannealed sample served as a reference sample for analysing the spectra of annealed samples. RBS analysis was done on annealed samples to investigate the interactions between Co and Si. All the RBS spectra of samples annealed up to 350 °C were found to perfectly overlay with the unannealed samples; hence, these are not reported here as there was no visible reaction, even after annealing for 7 days.

The overlay of RBS spectra from the unannealed and annealed samples at 400 °C and 450 °C for 24 h are given in Figure 4.3 and Figure 4.4. Qualitative information can be derived from these figures, which show a reduction in the height of the Zr and Fe peaks, and these are shifted a little bit toward the higher energy channels in comparison with unannealed spectra. After annealing, the back edge (lower energy) of the Co signal has a progressive shift towards the higher energy channels, which indicate diffusion and reactions. At the same time, a shift may be observed on the low energy Si edge, which tends to shift toward the higher energy channels. The initial diffusion process involved Co diffusing through an FeZr diffusion barrier layer and reacting with Si. This indicates that Co diffusion is taking place towards Si and vice versa.

The spectra of the samples annealed at 400 and 450 °C for 24 h have a slight difference in the Si edge slope compared to the unannealed. A shift to higher energies by the Si edge can be observed with the annealing duration indicating a growing reaction. These results indicate that the Co/Si interface begins to react at a temperature of 400 °C with the formation of cobalt silicide.

Furthermore, while annealing at 400 and 450 °C for 24 h with a diffusion barrier thickness of 33 nm, it can be observed in Figure 4.3 and Figure 4.4 that the high energy edge of the Si signal starts to progressively shift towards Si surface channel. This confirmed that a silicide was conforming next to the Si substrate. That means the area which grows on the

Si edge continues to grow towards the Si surface channel position.

Although barely visible after annealing the sample at 400 and 450 °C for 24 h, there is a reduction in height and a further shift to lower energies of the Co signal. This is accompanied with the appearance of a small step at the high energy edge of the Si signal. From Figure 4.4 it is clear that the extent of the inter-diffusion is greater in the sample annealed at 450 °C for 24 h, which has a clear step forming of silicide phase.

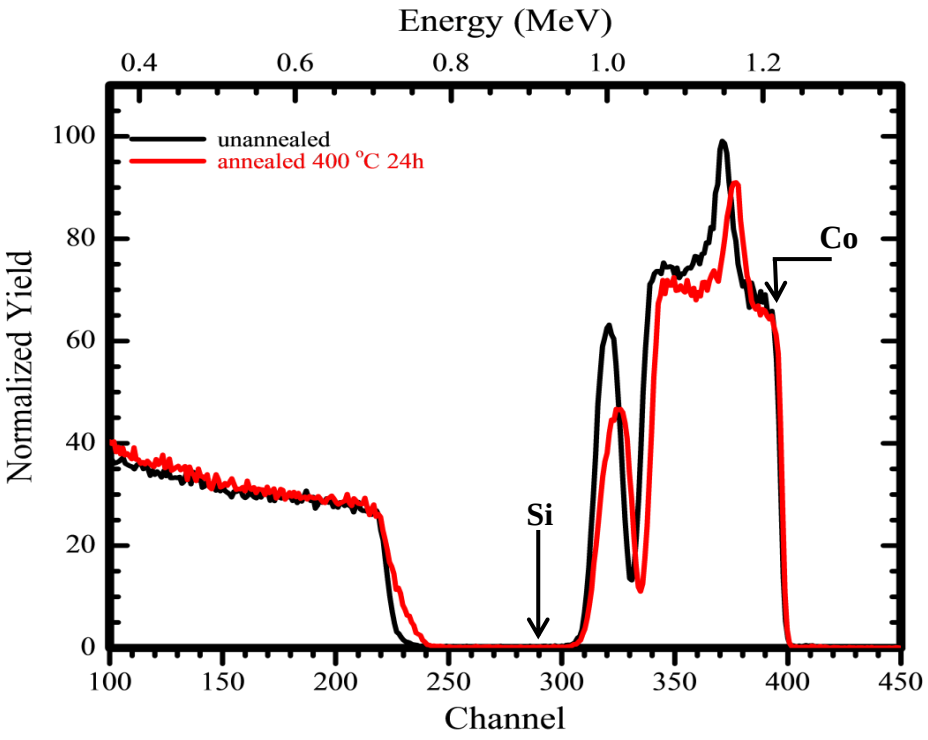

Figure 4.3: Overlay of RBS spectra of unannealed Si<100>|FeZr(33 nm)|Co(126 nm) and 400 °C annealed samples.

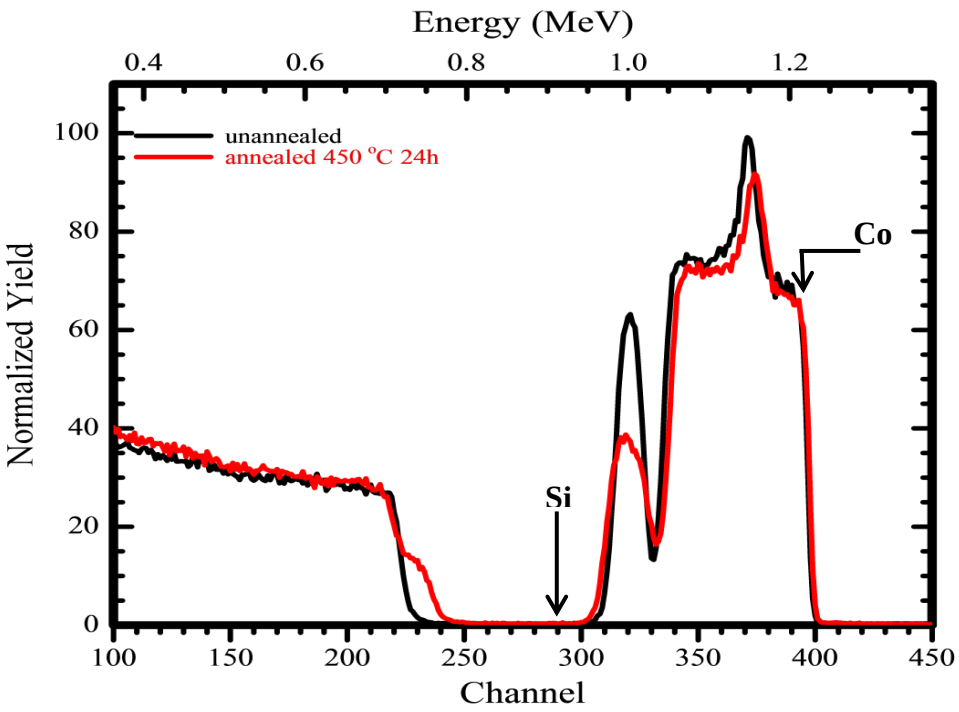

Figure 4.4: Overlay of RBS spectra of unannealed Si<100>|FeZr(33 nm)|Co(126 nm) and 450 °C annealed samples.

The depth profiles in Figure 4.5, obtained by AES analysis, shows Co, Fe, Zr, and Si peaks, as well as the presence of carbon at the surface and the Co/FeZr interface. Oxygen was also detected by AES analysis and it is striking that its variation in concentration follows that of Zr. This could be due to Zr's affinity for oxygen, linking the two elements strongly together. The AES results indicate that a complex mixed-phase region with up to six elements could be identified. In this region of sputtering time between 2000-2250s, it is interesting to note that the Si and Co concentrations are constant and in at 1:1 ratio. This suggests that the Co and Si are in a phase with a narrow composition range. Fe is also found to be uniformly distributed in the Co layer, with the concentration approximately 5-10%. According to the Co-Fe phase diagram [10], as much as 10% of Fe can dissolve into Co.

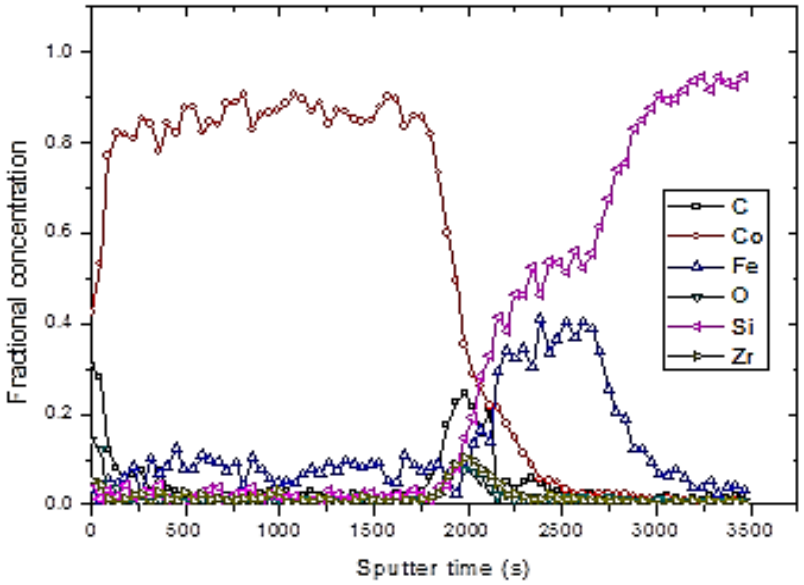

Figure 4.5: The AES depth profile of the Si<100>|FeZr(33 nm)|Co(126 nm) sample after annealing at 450 °C for 24 h.

The AES results informed the RBS simulations, and the resulting depth profiles determined from the RBS simulations are shown in Figure 4.6. The Co and Si profiles, which could indicate the formation of cobalt silicides, are similar and consistent with the AES profile. The simulation of the RBS spectra of samples annealed at 450 °C for 24 h was done in terms of seven layers. The simulations were performed by dividing the hypothetical sample into several sub-layers, each with a particular thickness and composition. In the case of 24 h annealing, the thickness of the cobalt layer was 1100×10^{15} at /cm^2 wide, comprising of 96.2 % cobalt and 3.8 % iron. The layer next to the remaining Co was 5×10^{15} at/cm^2 wide, comprised of 90.7 % iron and 9.3 % zirconium. The third layer was 5×10^{15} at/cm^2 wide, comprised of 34.8 % Fe, 43.5 % Si, 8.3 % Zr and 13 % C. The fourth layer was 180×10^{15} at/cm^2 wide, comprised of 23.1 % Fe, 51.9 % Si, 4 % O, 16.9 % Zr and 4.1 % C. The fifth layer was 220×10^{15} at/cm^2 wide, comprised of 38.3 % Fe, 51.1 % Si, 5.3 % O and 5.3 % C. The layer next to the Si was 70×10^{15} at/cm^2 wide, comprised of 26.1 % Co, 21.7 % Fe and 52.2 % Si. The silicon layer was very thick and wide, comprised of 100 % silicon.

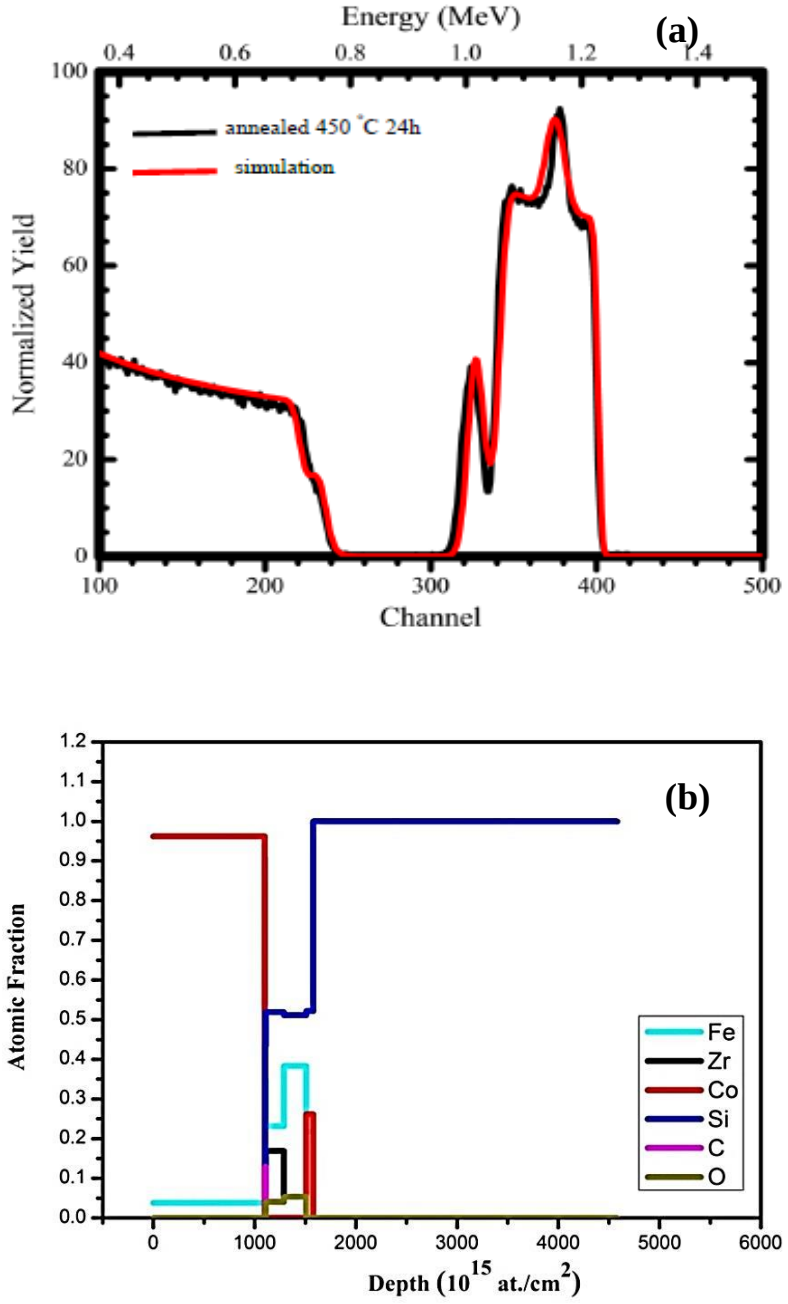

Figure 4.6: (a) Comparison between the RBS spectrum and a simulation of the annealed Si<100>|FeZr(33 nm)|Co(126 nm) sample, and (b) a representative composition profile of the simulation used.

4.5.2 XRD results

The crystal structure, chemical composition of the phases that formed in the annealed samples, was characterised by means of XRD analysis.

The wide-angle diffraction pattern of the Si<100>/FeZr (33 nm)/Co(126 nm) sample annealed at 400 and 450 °C for 24 h is presented in Figure 4.7 and Figure 4.8, which reveal peaks of Co, CoSi and Si substrate. High intensity Co (hexagonal) peaks may be observed at 2θ = 52.2° position with (002) orientation plane. The weakest reflections are due to the predominant peaks of the CoSi at two-theta positions; 47.5° and 56.3º, indicating 200 and 220 preferential of CoSi. Si peaks are also observed at 2θ = 38.7º and those are indexed to the 210 planes.

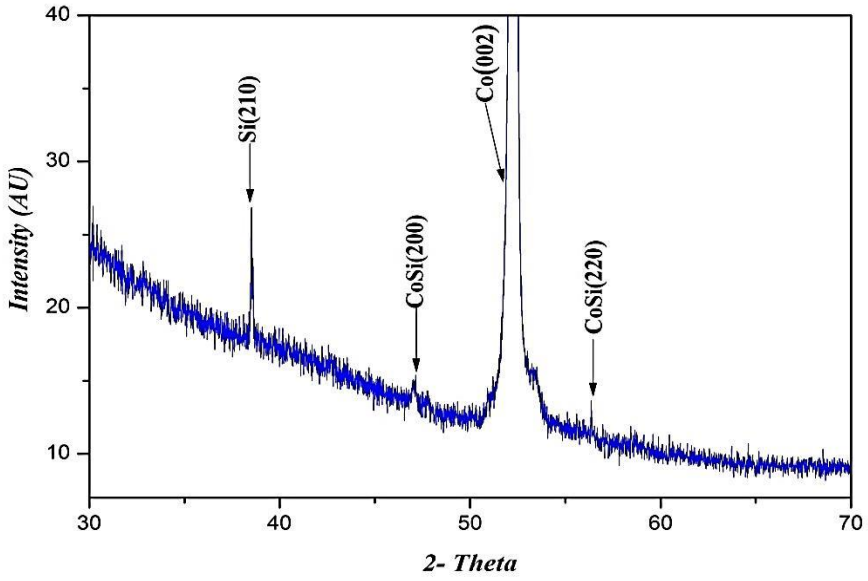

Figure 4.7: XRD pattern of the Si<100>|FeZr(33 nm)|Co(126 nm) sample annealed at 400 °C for 24 h showing the formation of CoSi.

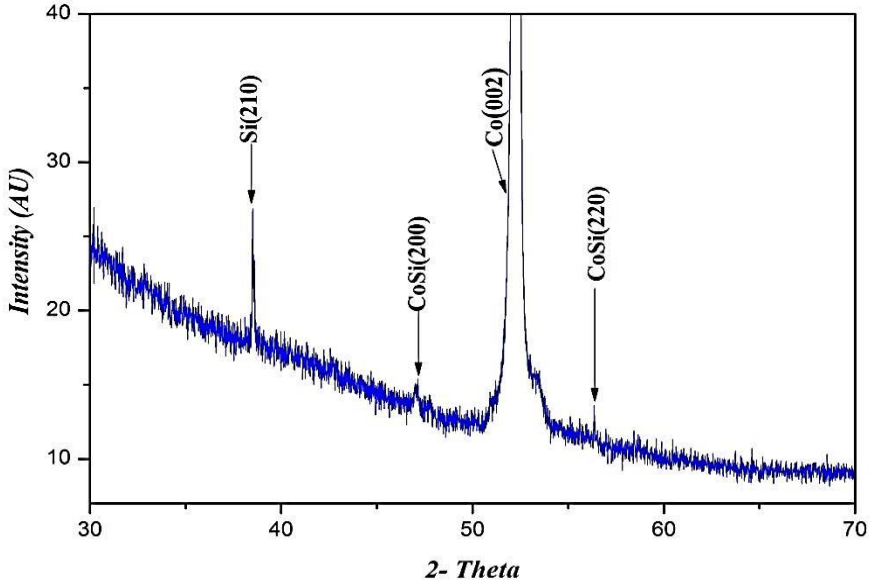

Figure 4.8: XRD pattern of the Si<100>|FeZr(33 nm)|Co(126 nm) sample annealed at 450 °C for 24 h showing the formation of CoSi.

4.5.3 SEM results

Figure 4.9 depicts the SEM images of samples after isochronal annealing at 400 and 450 °C for 24 h and with a diffusion barrier thickness of 33 nm. Annealing the sample caused the formation of crystals on the surface in contrast to the unannealed sample, shown in Figure 4.2. From visual comparison of the SEM images in Figure 4.2 and Figure 4.9, it may be observed that the crystals growth with black spots occur on the surface. The appearance of the crystals on the surface is an indication of the formation of the silicides, which can also be clearly seen in the XRD pattern shown in Figure 4.7 and Figure 4.8. Furthermore, the manifestation of black spots on the surface is due to the possible presence of some of the carbon layer in the interface. It could have come from the air when the vacuum was being broken down in the furnace or occurred through carbon contamination from the pumps, especially if the tubes were tapped and switched off.

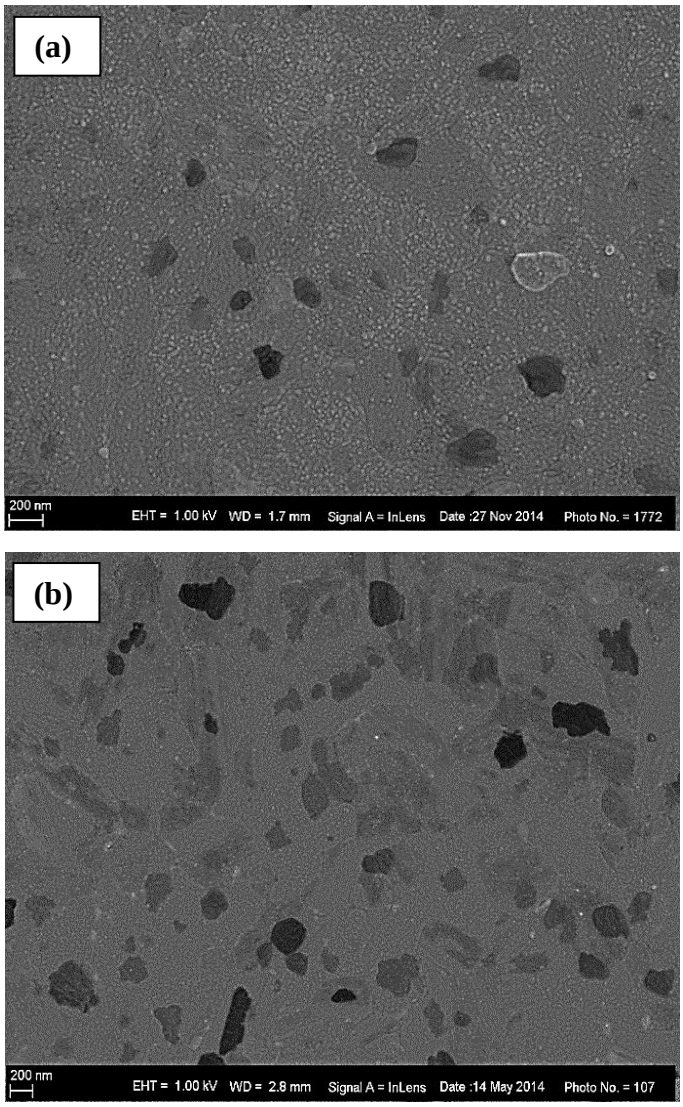

Figure 4.9: SEM micrographs of the Si<100>|FeZr(33 nm)|Co(126 nm) sample (a) at 400 ºC and (b) at 450 °C.

4.6 Annealed Si<100>/FeZr(43nm)/Co(126 nm) Sample

4.6.1 RBS results

The reaction of the quaternary Si/FeZr/Co system is far more complicated than both a ternary system and the simple reaction of Co with Si. Figure 4.10 and Figure 4.11 show the spectrum obtained after annealing for 24 h at 400 and 450 °C. The following qualitative information can be derived by comparing these spectra: the back edge (lower energy) of

the Co signal does not have a progressive shift towards higher energy channels after annealing. Although such an occurrence was expected, it is not obvious because some Fe atoms had replaced the Co atoms. At the same time, a shift can be observed on the high energy edge of the Si signal, which tends to shift toward higher energy channels after annealing. This indicates that inter-diffusion is taking place at the Co/Si interface. The Si signal's shifts to higher channels further indicating a movement towards the surface but a lack of mixing with the original Co layer to any significant extent. The front most part of the Si signal shows a region of constant Si composition, while the deeper region shows a graded composition profile. Substantial changes in the Fe distribution can be noted (channels 305-335), while the Zr enrichment layer appears to be unchanged.

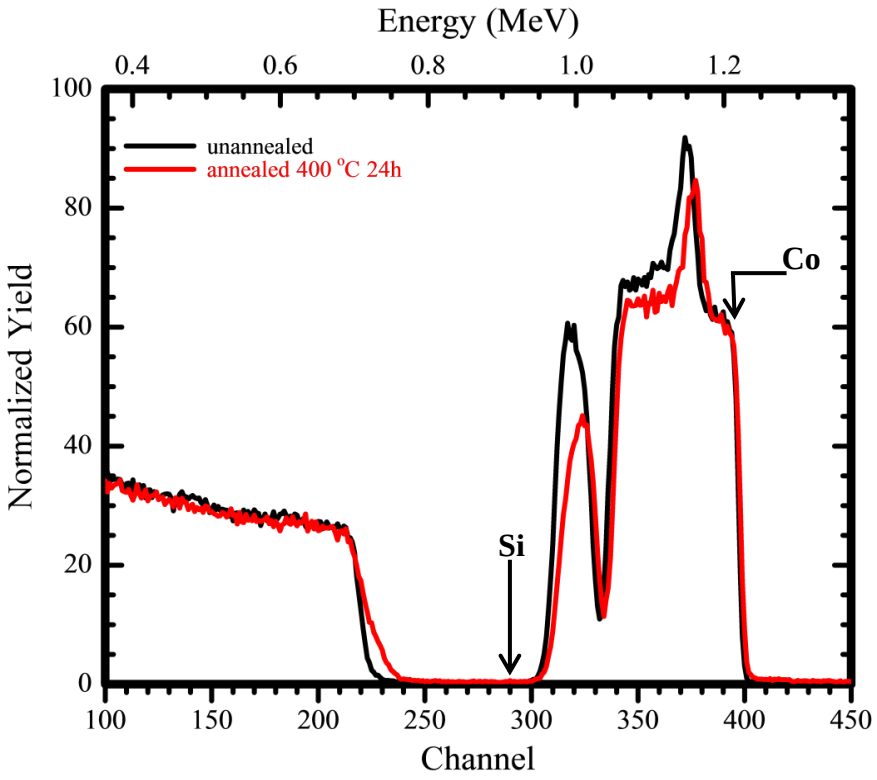

Figure 4.10: Overlay of RBS spectra of the Si<100>|FeZr(43 nm)|Co(126 nm) unannealed and 400 °C annealed samples.

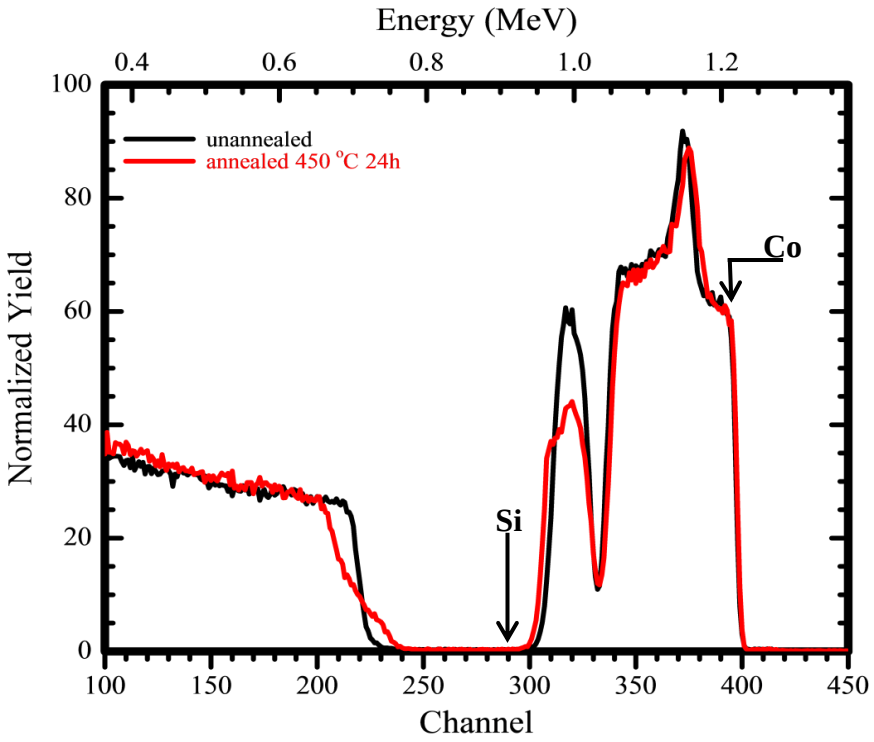

Figure 4.11: Overlay of RBS spectra of the Si<100>|FeZr(43 nm)|Co(126 nm) unannealed and 450 °C annealed samples.

4.6.2 XRD results

In these and subsequent samples, the scattered X-ray signals of Fe/Co have sharp signals due to scattering in many different directions. After thermal annealing, the formation of some phases at the interface was observed.

Figure 4.12 and Figure 4.13 illustrates corresponding XRD spectra of the diffraction pattern of the 400 and 450 °C (24 h) annealed sample, which contains Co silicide peaks corresponding to diffraction from planes of the CoSi(200) and CoSi(220) at 2θ positions 47.5° and 56.3°. Other peaks are indexed to the Si substrate from planes (210) at 2θ = 38.7° and the Co from planes (002) at two-theta position 52.2°, which the stronger peak indicates. The formation of CoSi at the interface of this sample correlates with the results obtained through RBS. Samples annealed at 400 °C and 450 °C have similar diffraction peaks for the same thickness of diffusion barrier equal to 43 nm.

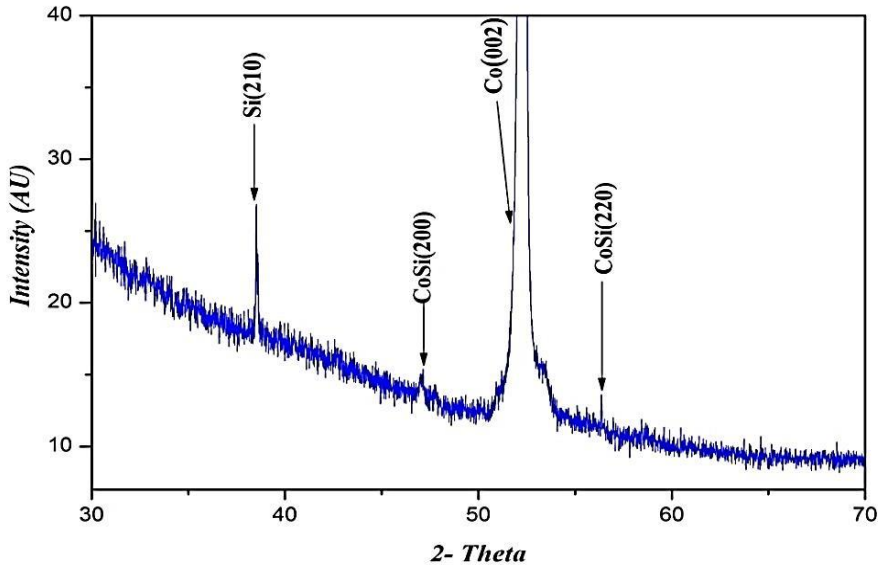

Figure 4.12: XRD pattern of a sample of Si<100>|FeZr(43 nm)|Co(126 nm) annealed at 400 °C for 24 h showing the formation of CoSi.

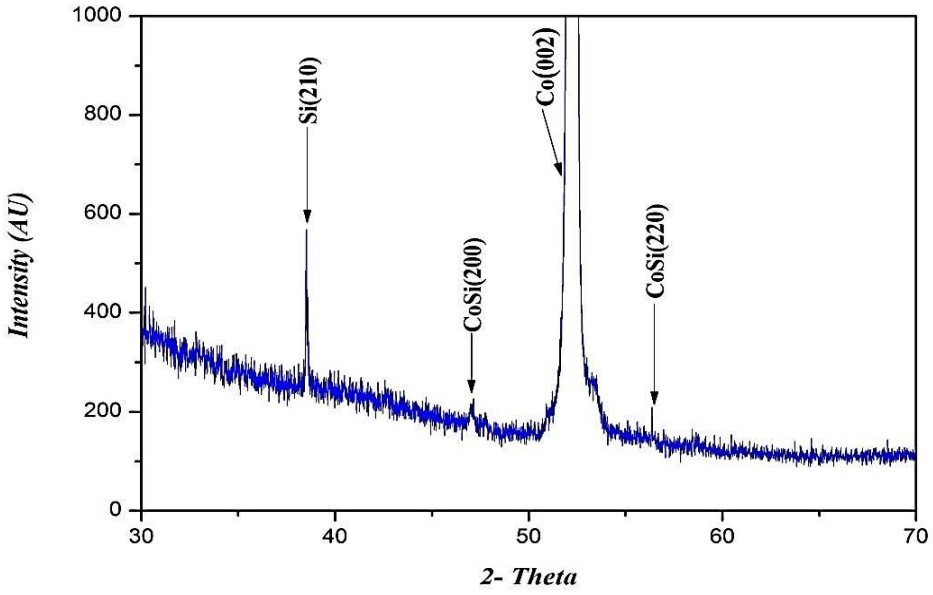

Figure 4.13: XRD pattern of a sample of Si<100>|FeZr(43 nm)|Co(126 nm) annealed at 450 °C for 24 h showing the formation of CoSi.

4.6.3 SEM results

In Figure 4.14 (a) the grains growth with less black spots means that there is less of a C-layer on the surface. The grains growth is not entirely clear and the granules can be seen on the surface because some Co had not completely reacted. In Figure 4.14 (b), an SEM image of the sample annealed at 450 °C, black spots of C, as well as crystals can be observed on the surface. This is because all Co is crystalline. One can then confirm, from the images in Figure 4.14 (a) and (b), the formation of cobalt silicides, which are also identified by the XRD pattern in Figure 4.12 and Figure 4.13.

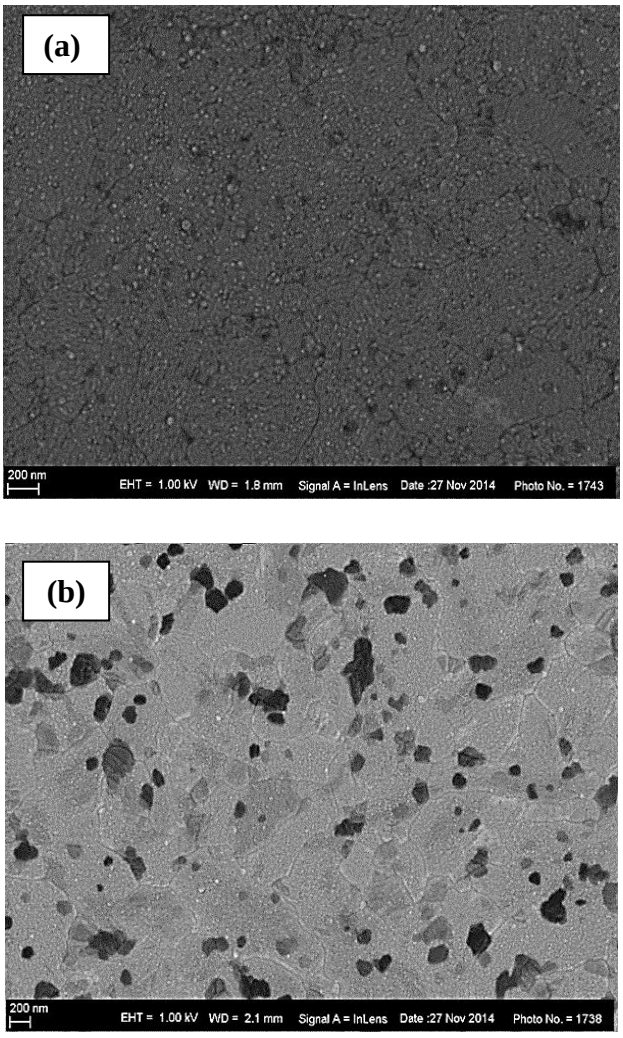

Figure 4.14: SEM micrographs of the Si<100>|FeZr(43 nm)|Co(126 nm) samples (a) at 400 °C (b) at 450 °C.

4.7 Annealed Si<100>/FeZr(48 nm)/Co(126 nm) sample

4.7.1 RBS results

Figure 4.15 shows the spectrum obtained after annealing for 24 h at 400 °C. The following qualitative information can be derived by comparing these spectra. After annealing, Co atoms came in contact with Si atoms and the Co metal began to react with the Si substrate, forming cobalt silicides. This completely agrees with the XRD data. The step on the Si edge grows towards the Si surface channel position, indicating lateral growth of the reaction zone.

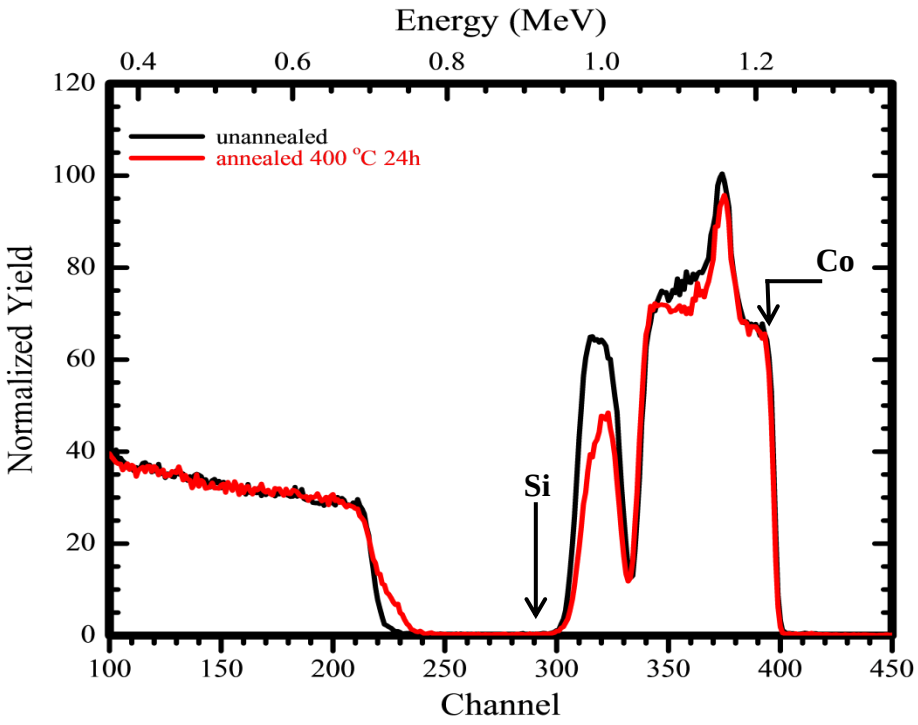

Figure 4.15: Overlay of RBS spectra of Si<100>|FeZr(48 nm)|Co(126 nm) unannealed and 400 °C annealed samples.

4.7.2 XRD results

The XRD scan of the 400 °C (24 h) annealed sample contains peaks corresponding to diffraction from the (200) and (220) planes of CoSi phase respectively. These peaks are also observed at the same two-theta positions in the subsequent annealed sample's peaks. Other peaks of Co silicides are indexed as $CoSi_2$ from planes (200), (210) and (310) at two-theta positions 48.5°, 54.7° and 65.9°. At the same time as shown in Figure 4.16, the diffraction pattern indicated that Si from planes (210) observed at 2θ = 38.7°, and Co from planes (002) observed at two-theta = 52.2 degree. This peak is observed at the same 2-theta position in the subsequent annealed samples.

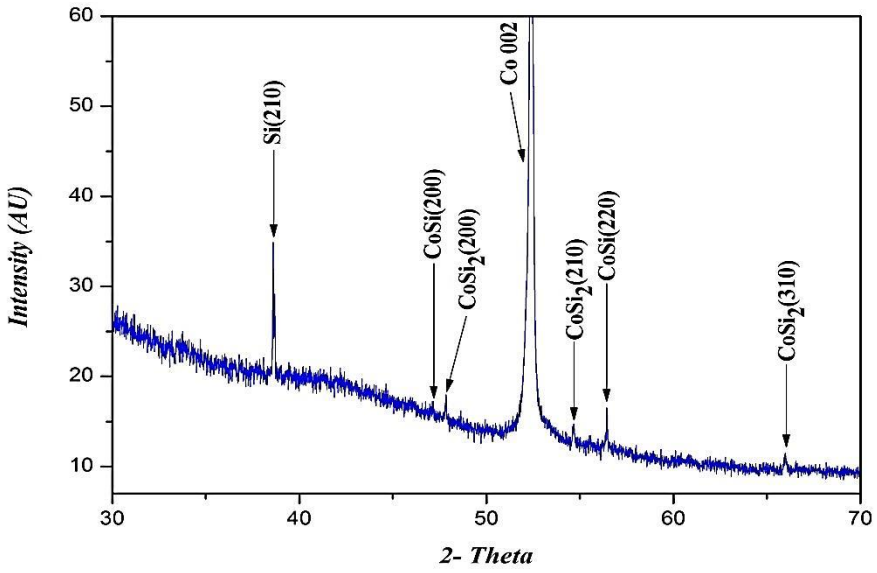

Figure 4.16: XRD pattern of a sample of Si<100>|FeZr(48 nm)|Co(126 nm) annealed at 400 °C for 24 h, showing the formation of a mixture of CoSi and $CoSi_2$.

4.7.3 SEM results

Figure 4.17 presents SEM images of the samples after isochronal annealing at 400 °C for 24 h, and with a diffusion barrier thickness of 48 nm. Annealing the sample caused the grains growth on the surface of the sample compared with the unannealed sample shown in

Figure 4.2. A visual comparison of the SEM images in Figure 4.2 and Figure 4.17 reveals that the grains growth occurred without black spots on the surface, which means that there was no carbon layer growth. The appearance of grains growth on the surface indicates the formation of cobalt silicides. This has also been demonstrated by the XRD data in Figure 4.16.

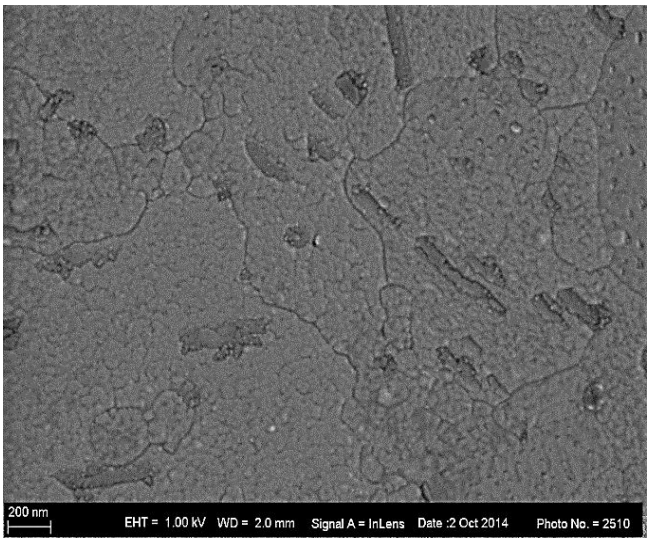

Figure 4.17: SEM micrographs of the Si<100>|FeZr(48 nm)|Co(126 nm) sample at 400 °C.

4.8 Annealed Si<100>/FeZr(53 nm)/Co(126 nm) sample

4.8.1 RBS results

From the Figure 4.18, it is clear that for the entire duration of the formation of cobalt silicide, both samples have a clear step forming. By annealing at 450 °C for 24 h with a diffusion barrier thickness of 53 nm, it is observed, that the lower edge of the Si step starts to progressively shift towards the Si surface channel. The upper part of the Si edge is observed, and conforms to the Si edge. This means that the area which grows on the Si edge continues to grow towards the Si surface channel position, indicating lateral growth of the reaction area. Also, the peaks obtained from XRD indicates the formation of $CoSi_2$

and CoSi phases. But the RBS spectra of samples annealed at 450 °C show a very low Si concentration, i.e. less than 50 % Si. This completely contradicts the XRD results. An explanation for this is that the cobalt silicides were formed as spot formation by forming in some areas but not in others. That is why the concentration of Si is completely different compared to that of the cobalt silicides formation as layer.

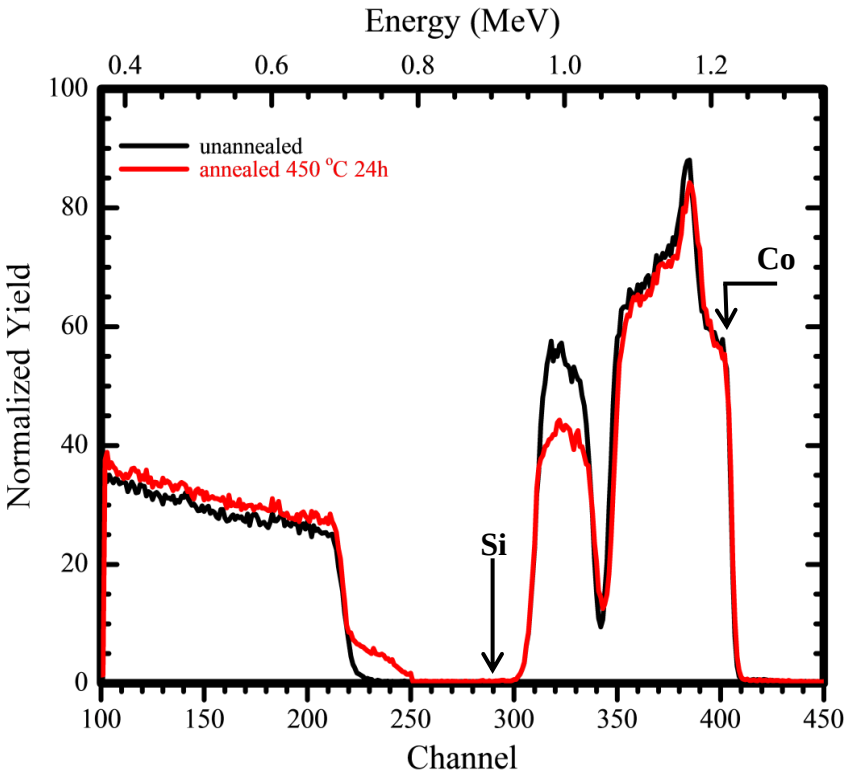

Figure 4.18: Overlay of RBS spectra of Si<100>|FeZr(53 nm)|Co(126 nm) unannealed and 450 °C annealed samples.

4.8.2 XRD results

The XRD scan of the 450 °C (24 h) annealed sample contains peaks corresponding to diffraction from the (200) and (220) planes of CoSi phase respectively. These peaks are also observed at the same two-theta positions in the subsequently annealed sample's peaks. In the 54.7° and 65.9° two-theta regions of the XRD scan of the 450 °C annealed sample there are peaks corresponding to diffraction from the (210) and (310) planes of the $CoSi_2$ phase respectively. These peaks are also observed at the same two-theta positions in the

subsequent annealed sample. With regard to the other peaks, the diffraction pattern indexed these as Si from planes (210) at two-theta position 38.7° and Co from planes (002) of the hexagonal Co phase at 2θ position 52.2°. These are indicated in Figure 4.19.

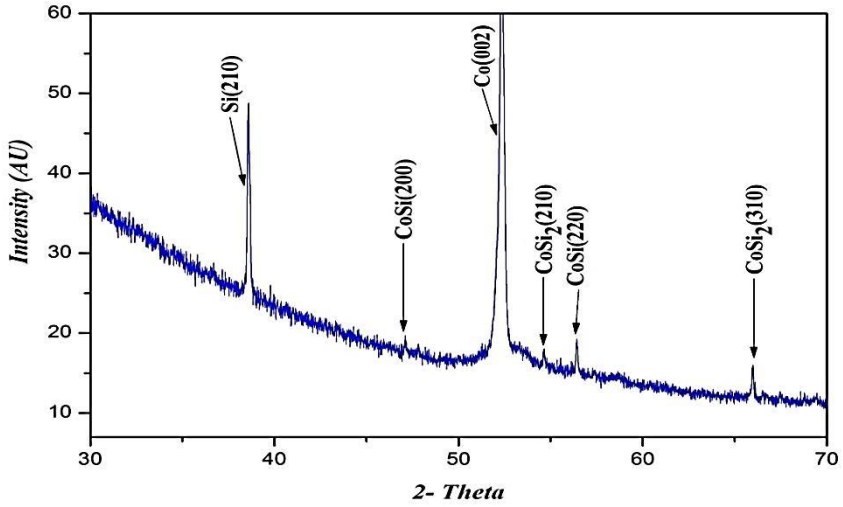

Figure 4.19: XRD pattern of the Si<100>|FeZr(53 nm)|Co(126 nm) sample annealed at 450 °C for 24 h.

4.8.3 SEM results

As can be seen in Figure 4.20, the annealing of the sample at 450 ºC causes crystals growth with clearly visible black spots on the surface. This growth suggests the formation of cobalt silicides, which is also clearly presented by the XRD pattern in Figure 4.19.

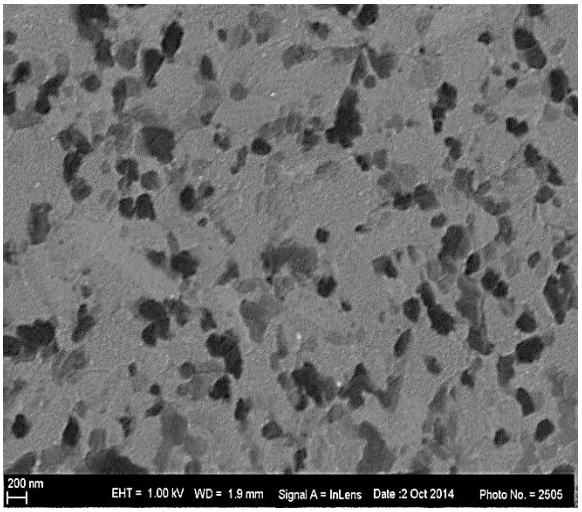

Figure 4.20: SEM micrographs of the Si<100>|FeZr(53 nm)|Co(126 nm) sample annealed at 450 °C.

4.9 Annealed Si<100>/FeZr(63 nm/Co(126 nm) sample

4.9.1 RBS and AES results

Figure 4.21 displays the spectrum obtained after annealing for 24 h at 450 °C. The following qualitative information can be derived by comparing these spectra. The area reaction at the edge of the Si signal indicates that two layers of different average composition were formed. The Si signal's shift to higher channels indicates a movement towards the surface but not a mixing with the original Co layer to any significant extent. The front most part of the Si signal shows a region of constant Si composition, while the deeper region shows a graded composition profile. Substantial changes in the Fe distribution can be noted (channels 300-340), while the Zr enriched layer appears to be unchanged. Since the mass resolution between Co and Fe is problematic for RBS, the samples were analysed by AES after all XRD and SEM measurements were performed.

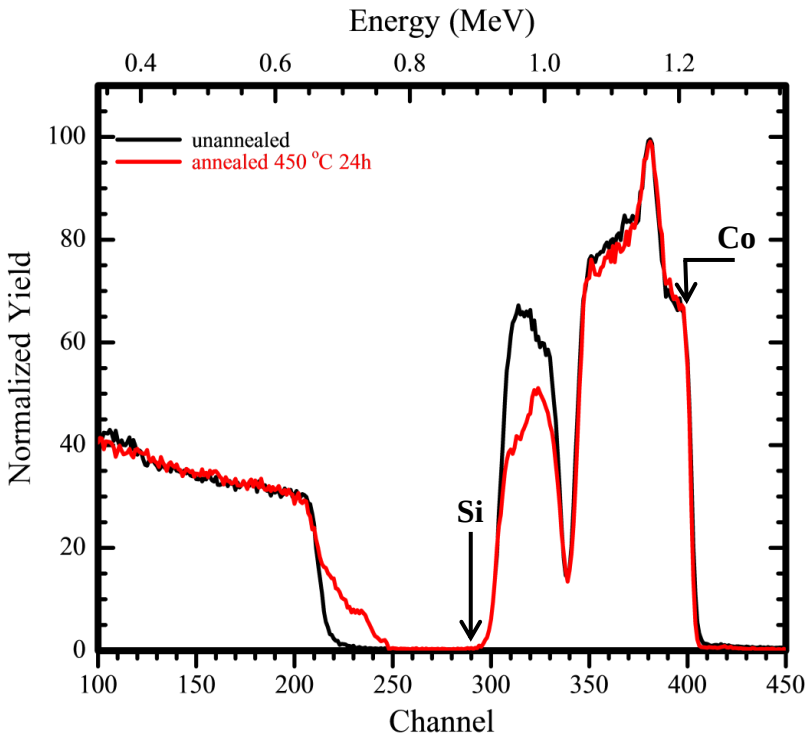

Figure 4.21: Overlay of RBS spectra of the Si<100>|FeZr(63 nm)|Co(126 nm) unannealed and 450 °C annealed samples.

The depth profiles obtained by AES analysis in Figure 4.22 show Co, Fe, Zr and Si peaks, and the presence of carbon at the surface and the Co/FeZr interface. Oxygen was also picked up by AES analysis and it is striking that its variation in concentration follows that of Zr. This could be due to Zr's affinity for oxygen linking the two elements strongly together. The AES results indicate that a complex mixed-phase region with up to six elements could be identified. It is interesting that, in this region (sputtering time between 2000-2500*s*), the Si and Co concentrations are constant and in a 2:1 ratio, while the Fe concentration steadily increases. This suggests that the Co and Si are in a phase with a narrow composition range. Fe is also found to be uniformly distributed in the Co layer with an approximate concentration of 5-10%. According to the Co-Fe phase diagram [10], as much as 10% of Fe can dissolve into Co.

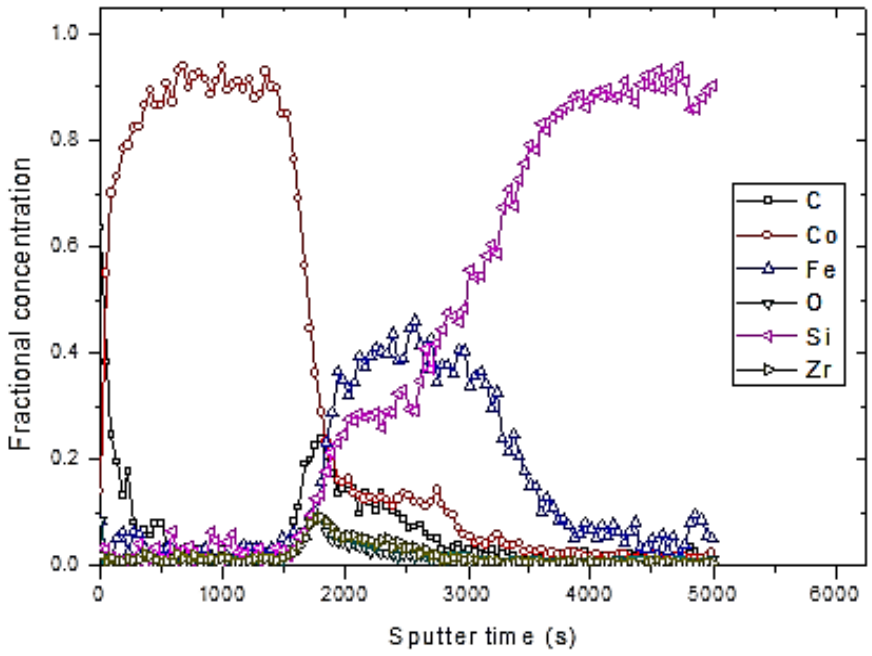

Figure 4.22: The AES depth profile of the Si<100>|FeZr(63 nm)|Co(126 nm) sample after annealing at 450 °C for 24 h.

The AES results informed the RBS simulations as seen in Figure 4.23 (a), and the resulting depth profiles determined from this are shown in Figure 4.23 (b). The Co and Si profiles, which could indicate the formation of cobalt silicides, are similar to and consistent with the AES profile. The simulation of the RBS spectra of samples annealed at 450 °C for 24 h was done with five layers (excluding the surface Co and the Si substrate layers) is shown in Table 4.1. The first three of these layers were used to model the Zr enrichment layer. The reduction in the height of the Fe peak, in comparison with the AES results shown in Figure 4.22, is explained by the solution of Fe atoms into the Co forming a Co(Fe). Therefore, after annealing, the RBS spectrum corresponding to the original Co layer seems unchanged.

Table 4.1: Results of the RBS simulations of the annealed sample.

Layer	**Thickness (at. /cm^2)**	**Composition (%)**					
		Co	**Fe**	**Zr**	**Si**	**O**	**C**
1	1100	86	13	-	1	-	-
2	85	66	10	4	17	3	-
3	80	-	37	17	11	12	23
4	30	13	13	24	40	7	3
5	325	11	50	-	31	6	2
6	300	2	42	-	56	-	-
7	3000	-	-	-	100	-	-

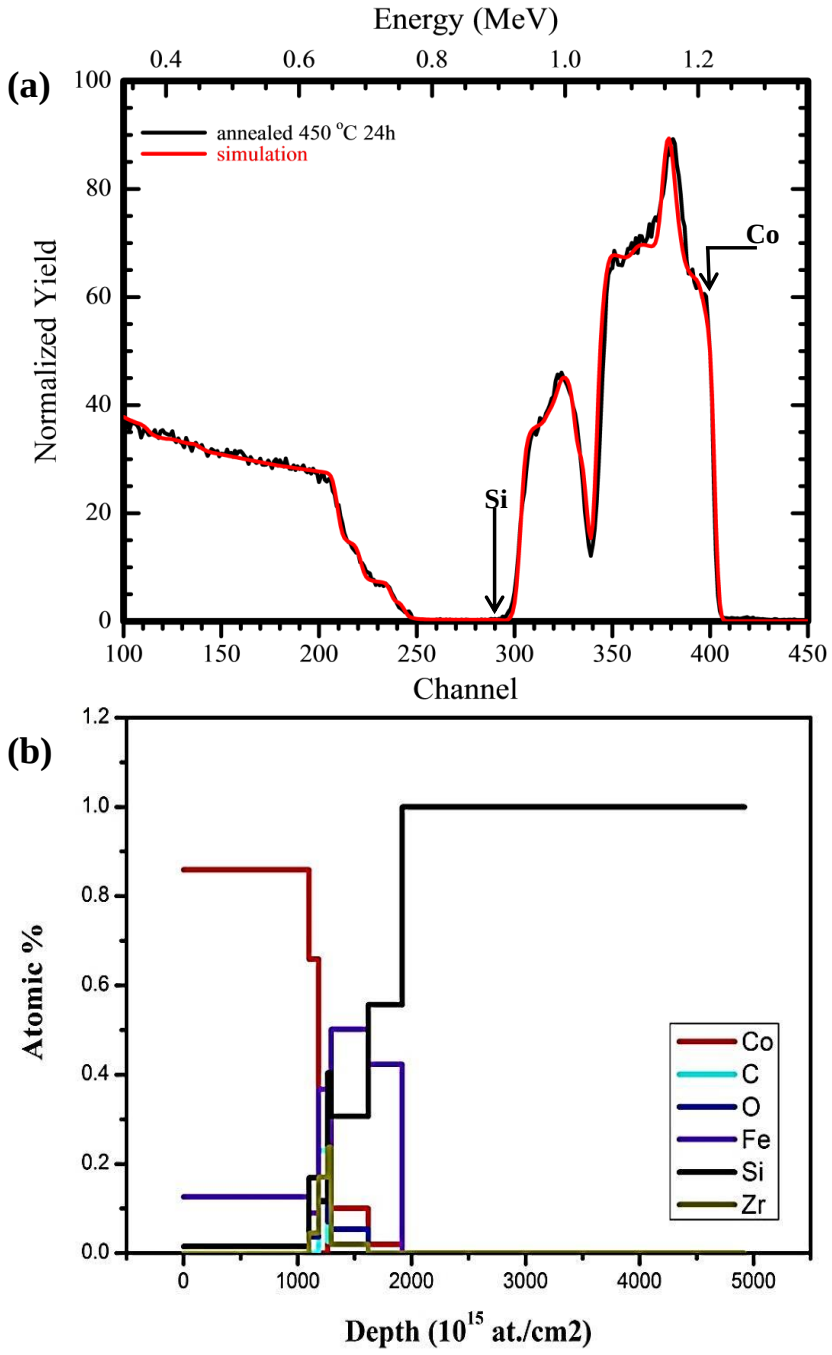

Figure 4.23: (a) Comparison between the RBS spectrum and a simulation of the annealed sample, and (b) a representative composition profile of the simulation used.

4.9.2 XRD results

The XRD scan of the 450 °C (24 h) annealed sample contains peaks corresponding to diffraction from the (200) and (210) planes of the CoSi phase respectively (see Figure 4.24). The other peaks of the cobalt silicides are indexed as $CoSi_2$ from the (200), (210) and (310) planes. At the same time, the diffraction pattern shows Si(210), as well as cubic Co(002) and possibly cubic Fe(110). However, the cubic Fe phase is only stable above 900 ºC, while the Co(002) phase is stable at 450 °C. This peak is therefore indexed as only Co(002). The reflections of the $FeSi_2$(040) and $CoSi_2$(210) as well as the $FeSi_2$(041) and CoSi(220) are close (d spacing within 0.003-0.005 Å). This study makes use of the fact that $FeSi_2$ is a high-temperature phase usually formed at 700 to 950 °C [11-13], with the lowest reported temperature of 550 °C [14] to exclude the possibility of $FeSi_2$ formation and we therefore positively identify the peaks at 54.7º and 56.3° as $CoSi_2$(210) and CoSi(220) respectively. While FeSi is present at 450 °C [14], its interplanar lattice spacing is very far from all the Co-Si interplanar spacing as indicated by the XRD results in Figure 4.24. FeZr serves as a barrier to the reaction of Co and Si, significantly increasing reaction times. There was no evidence of any silicide formation at 350 ºC for seven days, nor any XRD trace of Co_2Si, even at an intermediate annealing temperature of 400 ºC. Only the formation of CoSi and $CoSi_2$ were observed. The formation temperature of $CoSi_2$ is effectively reduced to 450 °C, compared to reported 700 °C when Ta was used as a diffusion barrier between Co and Si [15].

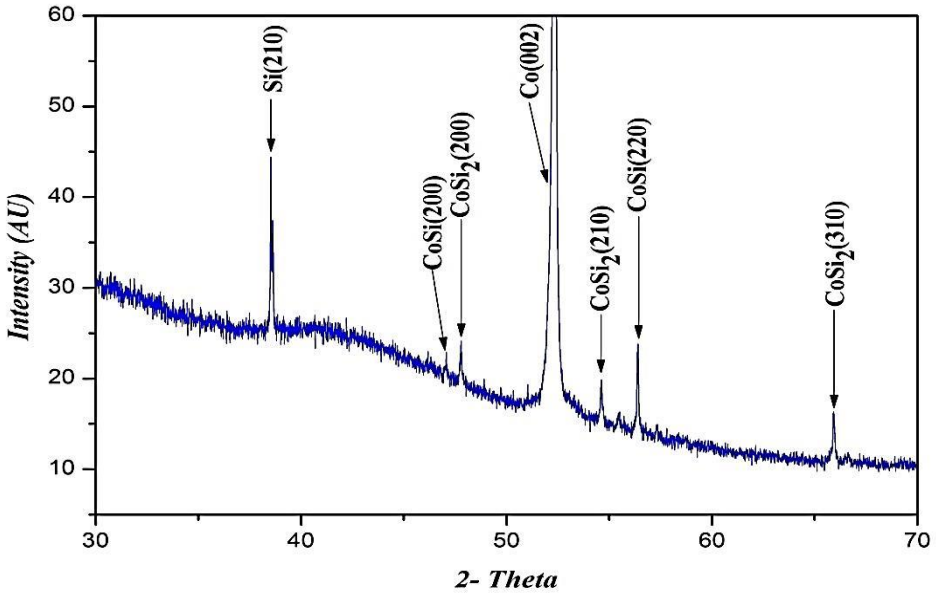

Figure 4.24: XRD pattern of the annealed Si<100>|FeZr(63 nm)|Co(126 nm) sample at 450 °C for 24 h, showing the formation of a mixture of CoSi and $CoSi_2$.

4.9.3 SEM results

Figure 4.25 shows the changes in the surface topography as a result of annealing the samples at 450 °C for 24 h. By comparing it with the unannealed sample shown in Figure 4.2, the formation of crystals with black spots, which is probably carbon on the surface, can be observed. The crystals are a very clear confirmation of the formation of cobalt silicides. Here, the black spots are somewhat transparent and, underneath them, the grains (or part of the grain) are visible. This confirms that the black spots were formed after the grains growth on the surface. Moreover, the manifestation of black spots on the surface is due to the possible presence of some of the carbon layer in the interface. It could have come from the air when the vacuum was being broken down in the furnace or occurred through carbon contamination from the pumps, especially if the tubes are tapped and the device switches off.

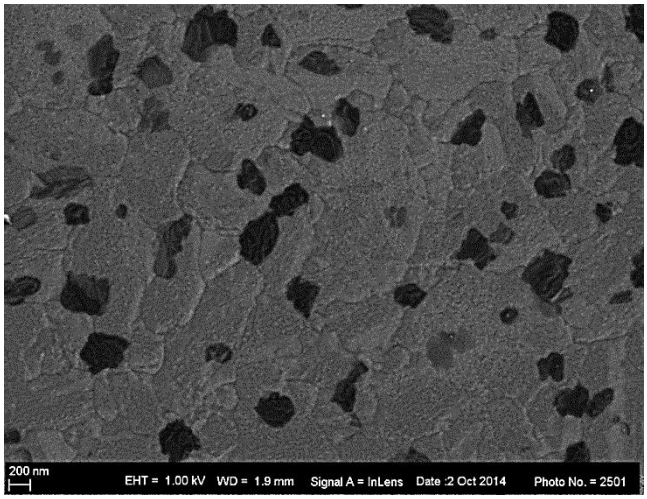

Figure 4.25: SEM micrograph of the annealed Si<100>|FeZr(63 nm)|Co(126 nm) sample at 450 °C.

4.9.4 A cross-sectional SEM

In Figure 4.26 a cross-sectional SEM image of the sample prepared by LN_2 fracture is shown and three different layers can be observed. At the top is the Co(Fe) layer that has formed large grains. The grains and some darker transparent areas (identified as surface carbon contamination, due to their transparency as well as the large carbon surface peak observed in the AES measurements) are clearly visible on plan-view SEM (not shown). Below this, the columnar microstructure of the reaction zone containing FeZr and both CoSi and $CoSi_2$ is visible. The interface of the reaction zone and both the Si substrate and the Co layer seems quite laterally uniform, which is in good agreement with the sharpness of the back edges of this layer, as observed in the RBS spectra. The thickness of the Co(Fe) is about 175 nm, while the reaction zone thickness is 70 nm, both of which are in good agreement with the RBS simulations.

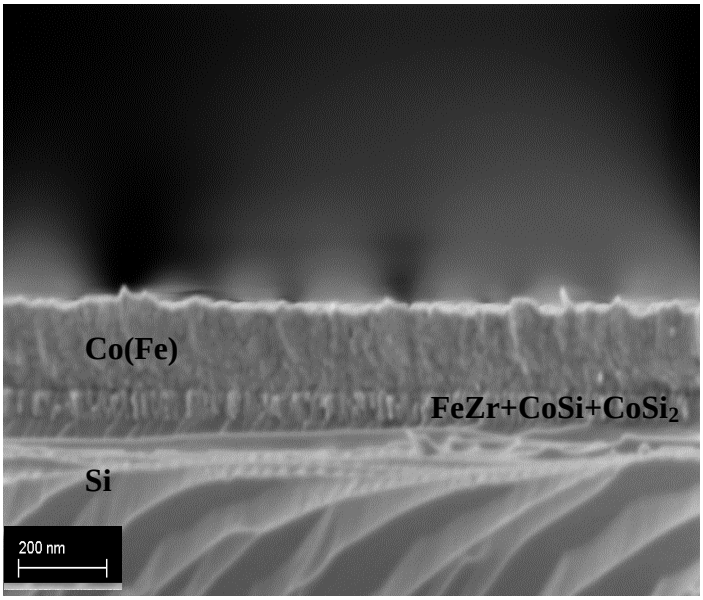

Figure 4.26: Cross-sectional SEM image of the annealed Si<100>|FeZr(63 nm)|Co(126 nm) sample prepared by fracturing.

4.10 Annealed Si<100>/FeZr(83 nm)/Co(126 nm) Sample

4.10.1 RBS results

In the case of the thicker (83 nm) FeZr diffusion barrier, little diffusion of Co atoms through the barrier layer (see Figure 4.27) occurred at 450˚C. Annealing the sample at this temperature for 24 h formed cobalt silicides and the XRD signal also indicates the presence of some CoSi and $CoSi_2$.

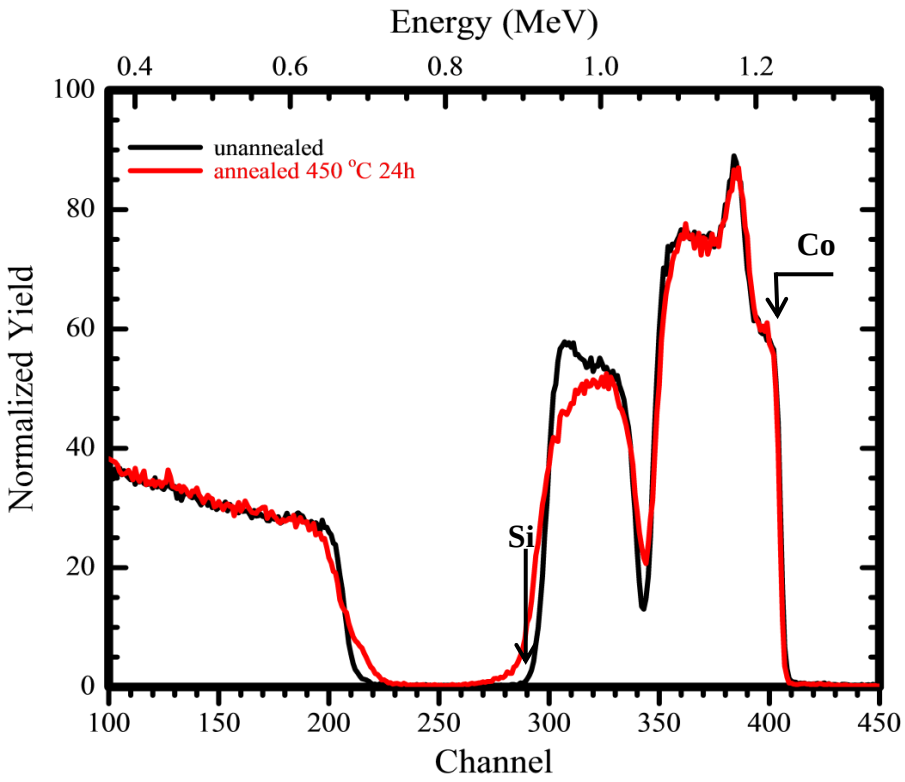

Figure 4.27: Overlay of RBS spectra of the Si<100>|FeZr(83 nm)|Co(126 nm) unannealed sample and 450 °C for 24 h annealed sample.

4.10.2 XRD results

For samples Si<100>|FeZr(83 nm)|Co(126 nm) annealed at 450 °C for 24 h, when compared to other cases, weak peaks from CoSi and $CoSi_2$ are visible, but a strong peak from the Si substrate can be observed. Also, less intense peaks overall can be observed than in the other cases. The various cobalt silicide phases, namely CoSi(200), CoSi(220) and $CoSi_2$(310), are also clearly present, as seen in Figure 4.28.

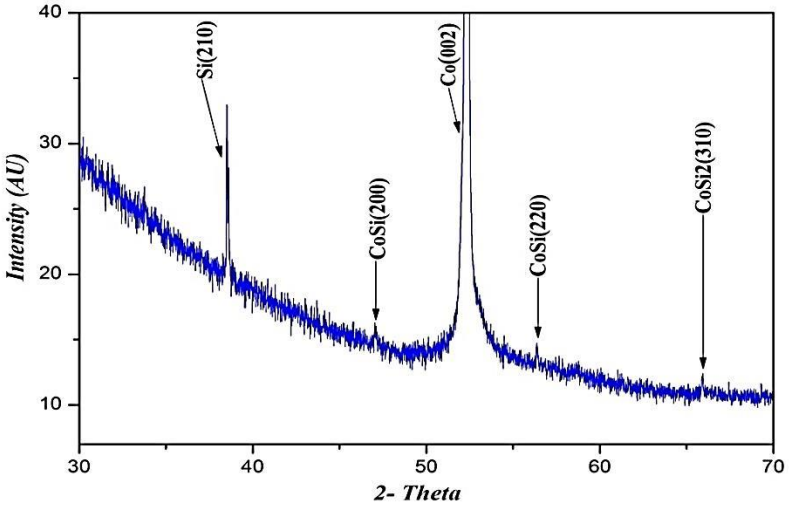

Figure 4.28: XRD pattern of a sample of Si<100>|FeZr(83 nm)|Co(126 nm) annealed at 450 ºC for 24 h showing the formation of a mixture of CoSi and $CoSi_2$.

4.10.3 SEM results

Figure 4.29 indicates the formation of very clear grains growth on the surface. That confirms the formation of cobalt silicide. This same figure shows the changes in the surface topography as a result of annealing. It is evident that the surface of the sample has grain bond and one can clearly see the grain boundary and grooving on it.

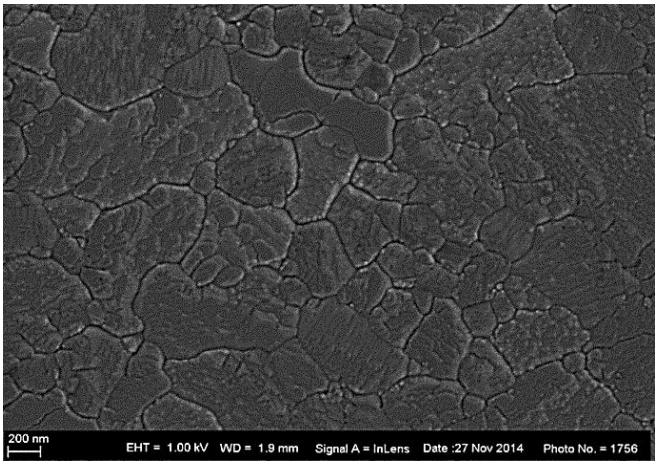

Figure 4.29: SEM micrographs of Si<100>|FeZr(83 nm)|Co(126 nm) at 450 ºC.

4.11 Annealed Si<100>/FeZr(100 nm)/Co(126 nm) sample

4.11.1 RBS results

Increasing the FeZr diffusion barrier layer reduced both the diffusion of Co atoms through the barrier layer and the formation of cobalt silicide at the edge of the Si signal in the RBS spectrum. The RBS spectra of the Si<100>/FeZr(100 nm)/Co(1000Å) samples annealed at a temperature of 450 ºC is shown in Figure 4.30. With the use of a 100 nm FeZr diffusion barrier layer, there was some cobalt silicide formation.

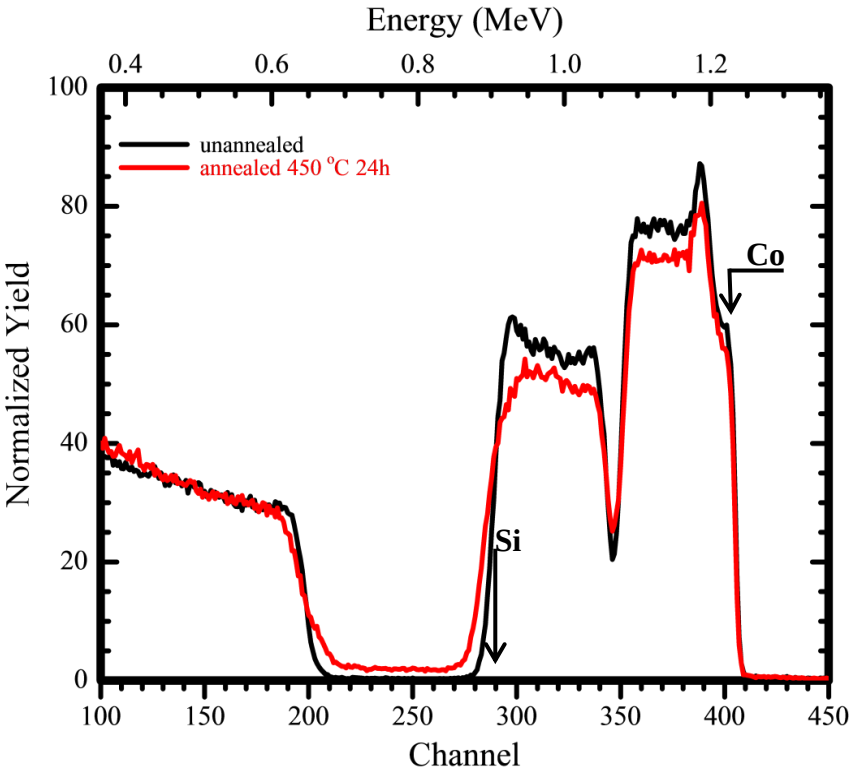

Figure 4.30: Overlay of RBS spectra of the Si<100>|FeZr(100 nm)|Co(126 nm) unannealed and 450 °C for 24 h annealed samples.

4.11.2 XRD results

The XRD results of the Si<100>|FeZr(100 nm)|Co(126 nm) sample annealed at 450 °C for 24 h show weak peaks from CoSi and $CoSi_2$. The various cobalt silicide phases, namely CoSi(200) and CoSi(220) at positions of two-theta 47.75º and 56.3°, as well as $CoSi_2$(200) and $CoSi_2$(210), were observed at 2θ positions 48.2° and 54.7° respectively, as seen in Figure 4.31.

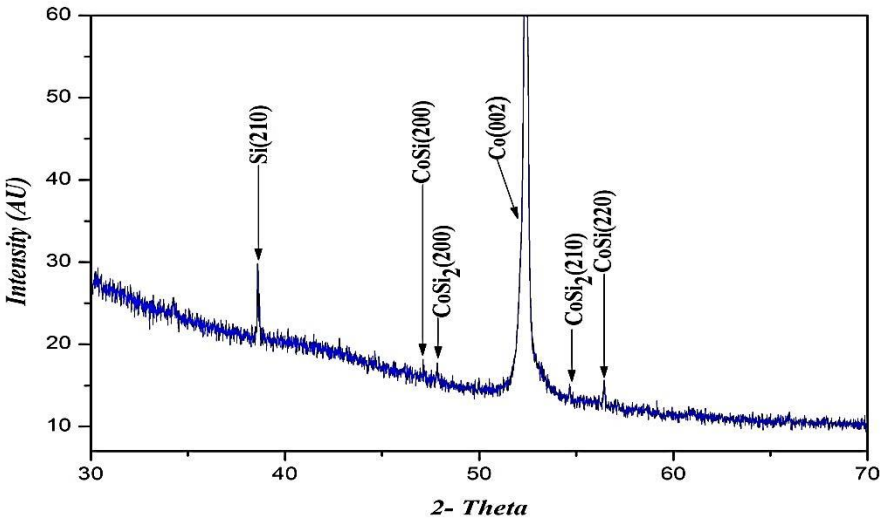

Figure 4.31: XRD pattern of a sample of Si<100>|FeZr(100 nm)|Co(126 nm) annealed at 450 ºC for 24 h showing the formation of a mixture of CoSi and $CoSi_2$.

4.11.3 SEM results

A comparison between the SEM images of the unannealed and annealed Si<100>|FeZr(100 nm)|Co(126 nm) sample show that much change has occurred on the surface, as shown in Figure 4.32. The result is the same as that of the Si<100>/FeZr(83 nm)/Co(100 nm) sample with the formation of clear grains without black spots on the surface. This confirms the formation of cobalt silicides without the growth of carbon.

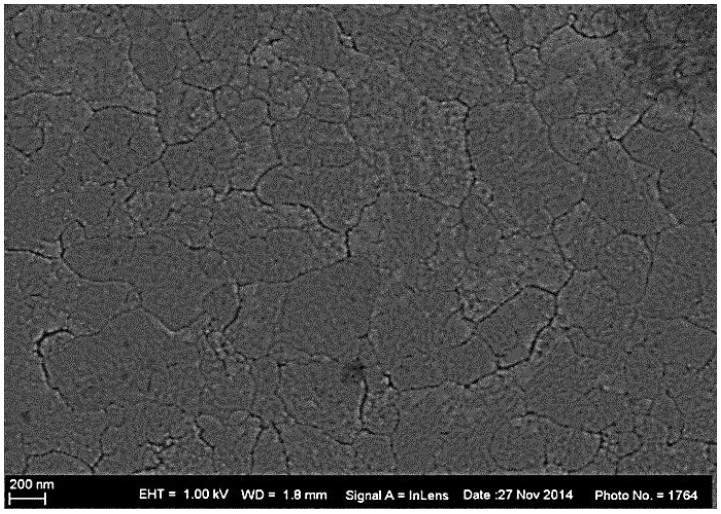

Figure 4.32: SEM micrographs of Si<100>|FeZr(100 nm)|Co(126 nm) at 450 ºC.

References

[1] S. S. Lau, J. W. Mayer and K. N. Tu. "Interaction in Co/Si thin-film system kinetics", *Journal of Applied Physics, 49, (1978).*

[2] G. Ottaviani, K. N. Tu, P. Psaras and C. Nobili, "In situ resistivity measurement of cobalt silicide formation", *Journal of Applied Physics, 62(1), (1987) 2290-2294.*

[3] R. Pretorius and J. W. Mayer. "Silicide formation by concentration controlled phase selection", *Journal of Applied Physics,81(5), (1997) 2448-2450.*

[4] A. Vantomme, M. A. Nicolet, G. Bai and D. B. Fraser. "Formation of epitaxial $CoSi_2$ on Si (100): Role of the annealing ambient", *Applied Physics Letters, 62(3), (1993) 243-245*

[5] M. L. A. Dass, D. B Fraser and C. S Wei. "Growth of epitaxial $CoSi_2$ on Si (100)", *Applied Physics Letters, 58(12), (1991) 1308-1310.*

[6] R. T. Tung and F. Schrey. "Increased uniformity and thermal stability of $CoSi_2$ thin films by Ti capping", *Applied Physics Letters, 67(15), (1995) 2164-2166.*

[7] R. T. Tung, "Growth of Epilaxial $CoSi_2$ Through a Thin Interlager ", *In MRS Proceedings, Cambridge University Press, Vol.427, (1996) 481.*

[8] L. R. Doolittle, "Algorithms for the rapid simulation of Rutherford backscattering spectra.", *Nuclear Instruments and Methods in Physics Research Section B: Beam Interactions with Materials and Atoms., 9.3, (1985) 344-351.*

[9] T. Wu and D. L. Kohlstedt, “Rutherford Backscattering Spectroscopy Study of the Kinetics of Oxidation of $(Mg,Fe)_2SiO4$,” *Journal of American Ceramic Society, vol. 45, (1988) 540–545*

[10] T. Nishizawa and K. Ishida. "The Co− Fe (Cobalt− Iron) system.", *Bulletin of Alloy Phase Diagrams., 5.3, (1984) 250-259.*

[11] A. De Luca, M. Texier, A. Portavoce, N. Burle, C. Grosjean, S. Morata and F. Michel. "Mechanism of β-$FeSi_2$ precipitates growth-and-dissolution and pyramidal defects formation during oxidation of Fe-contaminated silicon wafers.", *Journal of Applied Physics, 117(11), (2015) 115302*

[12] Y. Oikawa, C. Kim and H. Ozaki. "Effect of Fe–Si Mixed Powder on β-$FeSi_2$Formation from Fe–Si Mixture Film by Isothermal Process in Encapsulated.", *Space Japanese Journal of Applied Physics., 43(10), (2004) 7217–7221.*

[13] M. Takashi, and J. Ohsawa. "Formation of β-$FeSi_2$ with electron beam evaporation.", *Electronics and Communications in Japan., (Part II: Electronics) 87.1, (2004) 9-15.*

[14] S. S. Lau, J. Y. Feng, J. O. Olowolafe and M. A. Nicolet, "Iron silicide thin film formation at low temperatures", *Thin Solid Films, 25(2), (1975) 415-422.*

[15] J. Pelleg. "Formation of Co and Ta silicides on Si (111) and Si (100) substrates from codeposited Co and Ta thin films.", *Thin Solid Films, 325(1), (1998) 60-71.*

CHAPTER 5

CONCLUSIONS AND FUTURE WORK

5.1 Summary and Conclusions

Metal silicides continue to be an important part of the design philosophy in semiconductor technology due to their application as contacts or interconnects. Metal silicides are usually formed by a reaction between a deposited thin metal film and a silicon substrate (single crystal or polycrystalline), followed by a heat treatment at an appropriate temperature. Among these silicides, cobalt disilicide is currently the most widely used as it possesses the lowest resistivity, a low contact resistance and a good thermal stability. In order to be used in integrated circuits, a silicide must have sufficient thermal stability to withstand the entire thermal processing required, such as layer deposition and dielectric flow. In this study, the cobalt silicide formation through (FeZr) diffusion barrier layers (Chapter 4) was investigated.

Chapter 5 reports on the effect of the use of FeZr diffusion barrier layers on silicide formation in the Co-Si system and summarises the results of the investigation. Figure 5.1 illustrates the cobalt silicide formation through different thicknesses of FeZr diffusion barrier layers through use of a formation diagram. Table 5.1 summarises the thicknesses of the diffusion barrier layers, silicides formation, and temperatures at which theses silicide phases began to form.

As shown in Figure 5.1 and Table 5.1, the use of the thinner (33 and 43 nm Å) FeZr diffusion barriers for the Co-Si system impeded the Co diffusion at annealing temperatures of up to 400 °C. No diffusion was observed to occur across an FeZr diffusion barrier of varying thickness at temperature below 400 °C as observed from RBS, XRD and SEM analysis. CoSi started to form as first phase using thin thicknesses of FeZr diffusion barrier layers (33 and 43 nm). The initial phase to form after annealing at 400 and 450 °C for 24 h

was only CoSi. The presence of the FeZr barrier lowers the effective concentration of the Co at the growth interface, thus bypassing the formation of the Co_2Si precursor phase.

As shown in Figure 5.1 and Table 5.1, the use of the thicker (48, 53, 63, 83 and 100 nm) FeZr barrier layers impeded the diffusion of Co atoms through the barrier layer at temperatures of up to 400 °C. Annealing at 400 and 450 °C formed mostly $CoSi_2$, but the XRD measurements confirmed the presence of some CoSi, as indicated in Figure 5.2. In this study, CoSi formed as first phase at thin thicknesses of the diffusion barrier layer while CoSi and $CoSi_2$ formed simultaneously for thick thicknesses.

It can be argued that the presence of a thinner FeZr diffusion barrier layer lowers the effective concentration of Co at the growth interface and this results in the bypassing of the formation of Co_2Si as first phase. The thin FeZr barrier led to formation of CoSi as first phase at 400 and 450 °C, whereas the thick FeZr barrier formed mainly $CoSi_2$ as first phase at the same temperatures, even though the Co signal indicated the presence of some CoSi, which was also confirmed by the XRD measurements. The thicker FeZr barriers were more effective in impeding the diffusion of the Co atoms than the thinner barriers. The thicker FeZr barriers did not perform as well as the thinner ones. Some general conclusions can be drawn for the formation of cobalt silicides through FeZr diffusion barriers. Firstly, no silicide formation at all occurred at temperatures below 400 °C and the cobalt silicide formation was generally more uniform when thin barriers were used. The thin FeZr barrier delivered better uniformity of CoSi at a temperature of 450 °C.

The initial phases observed to form fit well with EHF model predictions. The FeZr diffusion barrier led to concentration-controlled phase selection by reducing the effective concentration of Co atoms available to react with Si, and this has been proposed as a model to interpret first phase formation occurring at solid interfaces:

- Leading to formation of CoSi as initial phase.
- Bypassing Co_2Si which forms between Co and Si without diffusion barrier.

Concentration-controlled phase selection in solid-state reaction has been proposed as a model to interpret first-phase formation occurring at solid interfaces. This is done in the context of the EHF model. The EHF model predicts, as the initial phase, the formation of Co_2Si at the Co/Si interface if there is no barrier layer. In the case of this study, the presence of FeZr as barrier layer caused CoSi to be formed as the initial phase, thus bypassing Co_2Si formation. The EHF model shows that the diffusion barrier can reduce the effective concentration of the Co atoms to a value where the effective heat of formation of CoSi is more negative than that of Co_2Si. Thus, first-phase formation of CoSi is thus thermodynamically favoured. The results obtained in this study fit well with the model if the initial phase Co_2Si has been bypassed.

The choice of FeZr as diffusion barrier between Co and Si has attractive applications in different fields. This study has shown the formation of CoSi and $CoSi_2$ which have known favourable electronic properties on Si substrate.

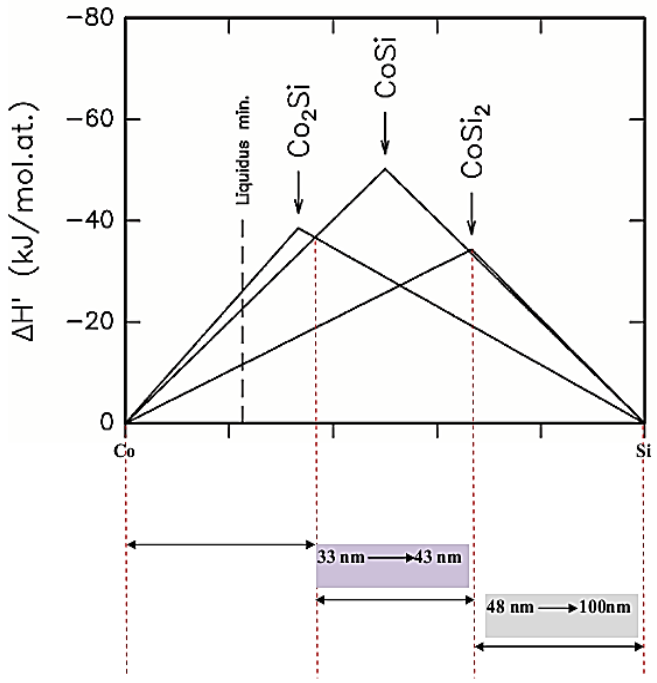

Figure 5.1: A diagram showing cobalt silicide formation through different thicknesses of FeZr diffusion barrier layers.

Table 5.1: Cobalt silicide formation through FeZr diffusion barrier layers.

Cobalt silicide formation through FeZr diffusion barrier layers		
Barrier	**Temp. (°C)**	**Silicide Formation**
FeZr(33 nm)	350	No reaction
	400	CoSi
	450	CoSi
FeZr(43 nm)	350	No reaction
	400	CoSi
	450	CoSi
FeZr(48 nm)	350	No reaction
	400	CoSi and $CoSi_2$
FeZr(53 nm)	350	No reaction
	450	CoSi and $CoSi_2$
FeZr(63 nm)	350	No reaction
	400	CoSi and $CoSi_2$
	450	CoSi and $CoSi_2$
FeZr(83 nm)	350	No reaction
	400	CoSi and $CoSi_2$
	450	CoSi and $CoSi_2$
FeZr(100 nm)	350	No reaction
	400	CoSi and $CoSi_2$
	450	CoSi and $CoSi_2$

After comparing the results of this system with other Co-Si systems with a diffusion barrier as summarized in Table 2.3, we never observed the formation of $CoSi_2$ on its own. However, in all cases (Table 2.3) where only $CoSi_2$ was formed, the annealing temperature was 500 °C or much higher. In this investigation, we stayed below 500 °C to study first phase formation as it may be argued that higher temperature annealing can lead to the

conversion of CoSi to $CoSi_2$, thus masking the simultaneous formation of CoSi and $CoSi_2$. It might be that annealing at temperature higher than 500 °C we would also only see $CoSi_2$, since this is the thermodynamically stable final phase.

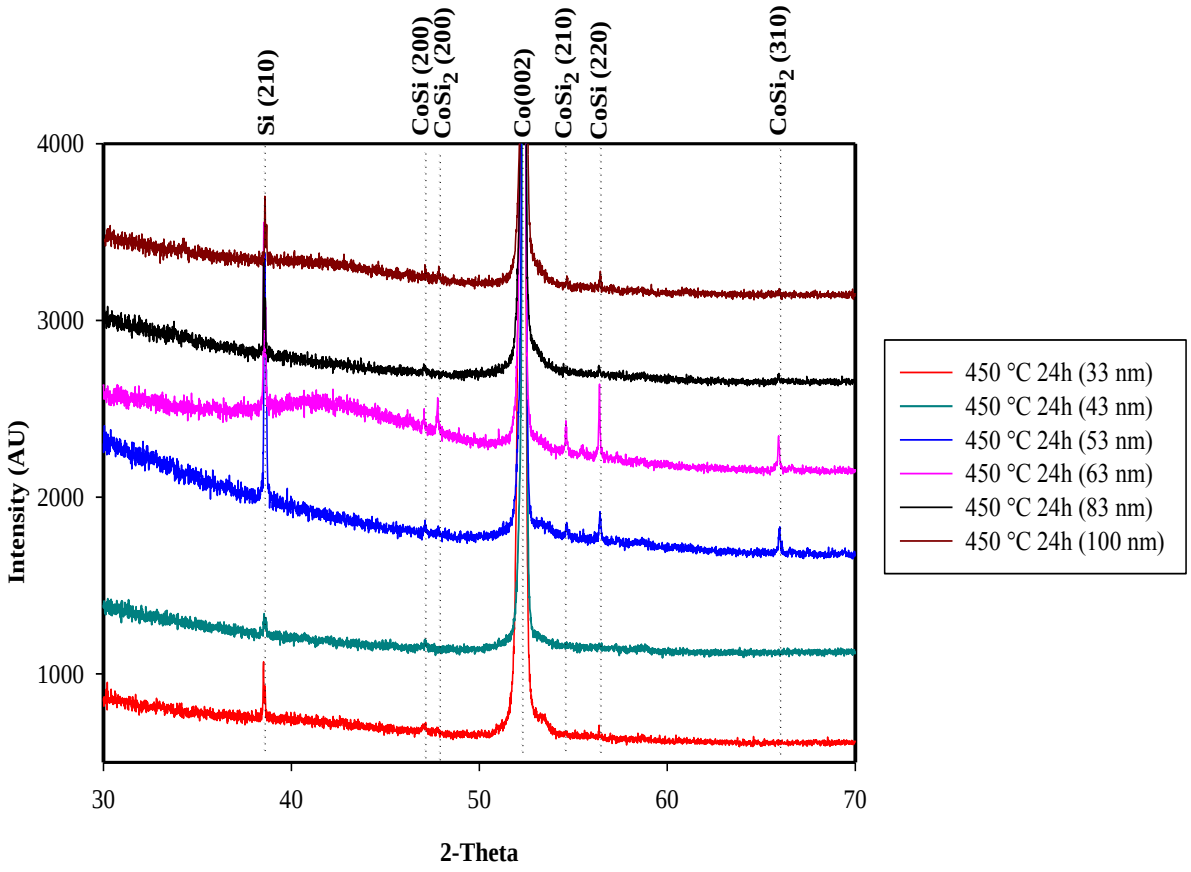

Figure 5.2: Overlay of XRD diffraction patterns of samples annealed at 450 °C for 24 h and different thicknesses of barrier layer (33, 43, 53, 63, 83 and 100 nm).

The surface topography of Co films was characterised by SEM. The surface morphology of the Co films prepared by MBE deposition appears homogeneous and smooth, according to the SEM images. No outgrowths were observed on the unannealed films. Based on similar scan sizes, as annealing temperature and duration increased, the film surface showed grain growth of the overlaying Co film.

5.2 Future work

There is a scope for further analysis of the work presented in this thesis. This would involve:

- Use of different orientation of Si substrate (001), (111) etc. since diffusion/reaction are known to depend on the substrate orientation.
- Analysis of the samples by cross section TEM to study the diffusion of Co through the FeZr layer.
- Kinetics of Co silicides formation through diffusion barrier layer (FeZr).
- Use of different a-barriers between Co and Si.